Analysis and processing of HRCT images of the lung for automatic segmentation and nodule detection

A thesis
submitted in partial fulfilment
of the requirements for the degree
of
Master of Science
in
Computer Science and Software Engineering
at the

University of Canterbury

by

Huaqing Chen

Dr. Ramakrishnan Mukundan…….Principal Supervisor

Associate Professor, Department of Computer Science and Software Engineering, University of Canterbury

Dr. Anthony Butler……..……Co-Supervisor

Senior Radiologist, Department of Radiology, University of Otago

University of Canterbury

2012

To my Mother and Father

Abstract

Automatic lung segmentation and lung nodule detection through High-Resolution Computed Tomography (HRCT) image is a new and exciting research in the area of medical image processing and analysis. In this research, two new techniques for segmentation of lung regions and extraction of nodules on the HRCT image are proposed. An automatic lung segmentation system is proposed for identifying the lungs in HRCT lung images. First, lung regions are extracted from the HRCT images by grey-level thresholding. The lung background information is eliminated by linear scans originating from border pixels. Finally, lung boundaries are smoothed along the mediastinum. The lung nodule extraction from the HRCT image is processed based on a set of continuous HRCT slices of lung images. In the first stage, the abnormal areas are extracted based on nodule pixel collection and combination. In the final stage, the abnormal area is extracted by comparing the density and shape profile. Both of the systems have been tested by processing data sets from 10 continuous image sets (100 images). Lung segmentation results are presented by comparing our automatic method to manually traced borders. Averaged over all results, the accuracy of lung segmentation is 96.10%. The proposed nodule detection method has been tested on image sets containing healthy and unhealthy lung images. Statistical analysis has been done and the results show the overall nodule detection rate is 88.44% along with the false positive rate of 0.18.

Acknowledgments

First and foremost, I would like to thank my supervisor, Dr Ramakrishnan Mukundan, for providing me with such a wonderful and rewarding research experience: you encouraged me to study things I thought I would never study and see places I thought I would never see. Special thanks to Dr Anthony Butler and Dr Justin Hegarty for providing a large collection of anonymised HRCT images (including both test images and reference images), which have been valuable for this research. I would also like to thank them for the useful discussions we had, which provided important information about medical images. I am thankful to Frieda Looser from the Learning Skills Centre for doing grammar checking for this document. I would like to thank the Bioengineering Group of the University of Otago, Christchurch, for providing HRCT datasets for this project.

Last, but far from least, I appreciate the help from the Department of Computer Science and Software Engineering at the University of Canterbury throughout the development of my Master's project. Thanks for providing me a stable and safe environment for my study.

Table of Contents

List of Figures

List of Tables

Chapter 1

Introduction

Medical image processing techniques can be used for diagnosis, treatment and research in medical imaging such as ultrasonography, High Resolution Computed Tomography (HRCT) and Magnetic Resonance Image (MRI). HRCT is the most commonly used diagnosis technique for the analysis of the lung regions and the number of HRCT evaluations of the lungs has been steadily increasing. Initially, HRCT images were only used by radiologists to diagnose patients' disease symptoms [1]. The radiologists identify the disease symptoms by visually searching for the abnormal texture shown on the HRCT images. Recently, research began to focus more on analysing medical images by using Computer Aided Diagnosis (CAD) systems [2], where the aim is to help medical professionals identify the disease symptoms more accurately. The CAD systems help radiologists to characterise the distribution of the disease patterns found on the HRCT images [3] and make their final decisions more confidently. The research presented in this thesis describes techniques for lung segmentation and lung nodule detection. The lung segmentation technique is used to pre-process the lung image, and the lung nodule detection technique uses the pre-processed lung image for further nodule detection.

Instead of detecting nodules based on original lung images, the proposed lung segmentation technique removes all the noise information outside of the lung regions. The lung segmentation method is based on the flood fill algorithm which is used to effectively identify the surrounding region. This step facilitates the use of

another fast method for the removal of the CT background using linear scans originating from border pixels. Connected components that represent parts of the trachea are removed by noting the separation of the mean and standard deviation of intensity values between the trachea and the lungs. The segmented lung images are further enhanced to restore the intensity values of the pixels on the bronchi and the lung boundary.

The nodule detection technique detects nodules existing on the segmented lung regions. Firstly, lung nodule candidates are defined as the regions of interest that possibly contain nodules, which are extracted by combining the pixels with similar intensity variation on the segmented lung regions. Then, extracted nodule candidates are filtered by a rule based filtering process. Finally, a shape descriptor is used to determine the shape features of the nodule candidates and compare them with the collected nodule shape features for identification. Instead of searching for a particular shape and large size lung disease symptom textures appearing on lung images, the proposed nodule detection technique is able to detect small size nodules by enlarging them for more accurate shape feature determination.

In this research, the majority of non-nodule information is eliminated by the following two processes:

- Segmenting lung regions from original lung images to get rid of the information located outside of the lung regions, such as bones and surrounding tissue regions.
- Processing the segmented lung regions from a set of consecutive HRCT slices to eliminate the unnecessary information located inside of the lung regions, such as veins and lung tissue.

1.1 Motivation

Lung nodule detection techniques offer the potential of screening and early cancer detection at a stage when it may be more effectively treated. This was motivated by significant developments in CT scanner technology.

Most of the nodule detection techniques have problems of (1) detecting lung nodules only with a radiologist's assistance, (2) detecting a small number of nodules, and (3) manually inputting data to complete the nodule detection process.

Lung images have a highly irregular intensity distribution, and their description with traditional methods is insufficient. Intensity based image analysis has been found to be useful in describing the pixel intensity variation and determining the overall image characteristics.

1.2 Objectives

This research aims to develop a generic model for lung segmentation and lung nodule detection which will segment the lung regions from lung images and detect the lung nodules with different shapes, sizes and locations.

For lung segmentation, the following objectives are considered:

- Separating the CT background, the lungs and the thorax region surrounding the lungs by grey-level thresholding.
- Using flood fill algorithm to effectively identify the thorax region. The seed point of the flood fill algorithm needs to be allocated automatically in the thorax region.
- Removing the CT background by using linear scans originating from border pixels.
- Removing airways based on noting the separation of the mean and standard deviation of intensity values between the airways and lungs.
- Restoring the intensity values of the pixels on the bronchi and lung boundary for further lung image enhancement.

For lung nodule detection, the following objectives are considered:

- Decomposing segmented lung regions based on classifying the pixels into different intensity intervals.

- Combining the pixels that have the same intensity as the nodule pixels to extract suspected nodules.
- Filtering the suspected nodules based on comparing their characteristics with nodules.
- Determining the shape features of the suspected nodules.
- Identifying nodules by comparing the shape feature of the suspected nodules with the shape feature of nodules.

1.3 Thesis Overview

The rest of this thesis is organised as follows:

- **Chapter 2** gives a brief interpretation of HRCT lung imaging and the literature review of lung image processing including lung segmentation and lung nodule detection.
- **Chapter 3** reviews the α-image decomposition based image analysis technique, which is used for processing highly irregular intensity distribution of lung images.
- **Chapter 4** describes the development of the lung segmentation technique that pre-processes the lung image for further accurate nodule detection use.
- **Chapter 5** describes the development of the lung nodule detection technique, which identifies nodules based on shape feature comparison.
- **Chapter 6** presents and analyses the results of the lung segmentation.
- **Chapter 7** presents and analyses the results of the lung nodule detection and evaluates some technique parameters.
- **Chapter 8** summarises the findings of this research. It concludes the thesis and outlines some future directions in the area.

1.4 Publication

The following paper was presented at the Otago Medical School, Christchurch:

- H. Chen, R.Mukundan, A. Butler, K.Hart. "A Multifractal Formulism for Segmenting HRCT Images of the lung", Oral presentation, Communicating Bioengineering Research, The Centre for Bioengineering, University of Otago, Christchurch, 10 November 2010.

The following paper was published in the Twenty-sixth International Conference on Image and Vision Computing New Zealand:

- H. Chen, R. Mukundan, A. Butler. "Automatic Lung Segmentation in HRCT Images", International Confernce on Image and Vision Computing, IVCNZ Auckland, 29 November 2011, pp. 293-298.

Chapter 2

Background

In this chapter, a brief background of lung anatomy, HRCT imaging and nodule characterisation is reviewed, followed by a description of lung image processing that subsequent chapters will be based on.

Section 2.1 reviews the domain knowledge of lung anatomy, HRCT imaging and nodule characterisation. Section 2.2 gives an overview of the related work on lung image processing including lung segmentation and lung nodule detection.

2.1 HRCT Lung Images Interpretation

Detailed understanding of lung anatomy, HRCT imaging and nodule characterisation is a necessary step for successful image interpretation. The way lung anatomy appears on HRCT images and radiologists interpret images are explained in this section. Section 2.1.1 describes the anatomical features of the lung, as well as the different lung regions. Section 2.1.2 introduces the structure of HRCT lung images and also explains the components of the HRCT images. Section 2.1.3 presents some common lung nodules and discusses their features.

2.1.1 Lung Anatomy

Each lung is located on the side of the thoracic cavity with a conical shape as Figure 2.1 shows. Each lung also contains a fissure, which separate the lung into upper and lower lobes. Lungs consist of bronchi (airway), blood vein and

connective tissue that holds up the lung structure. The alveoli and bronchioles are connected to each other as a bronchial tree and run alongside each other [4].

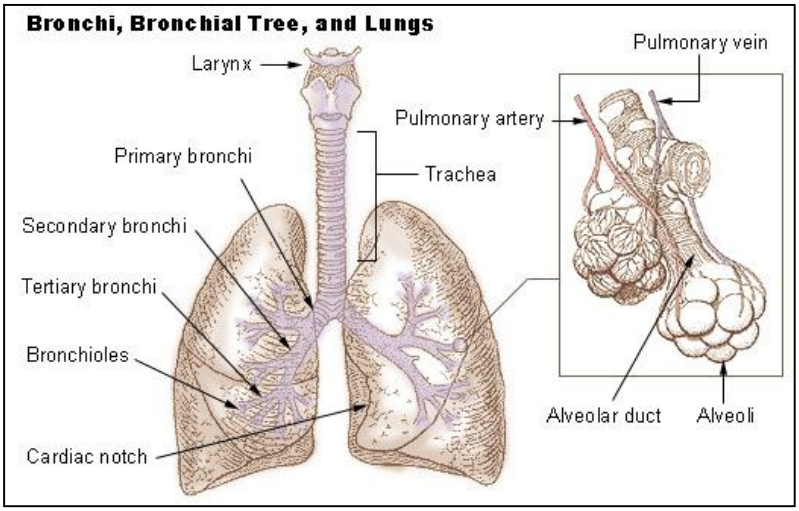

Figure 2.1 Bronchi, bronchial tree, and lungs. [4]

The lung regions can be further divided into three different regions: Apical, Middle and Basal [5]. In Figure 2.2, the lung regions are categorised into three regions. The division occurs along the axial plane of the human body.

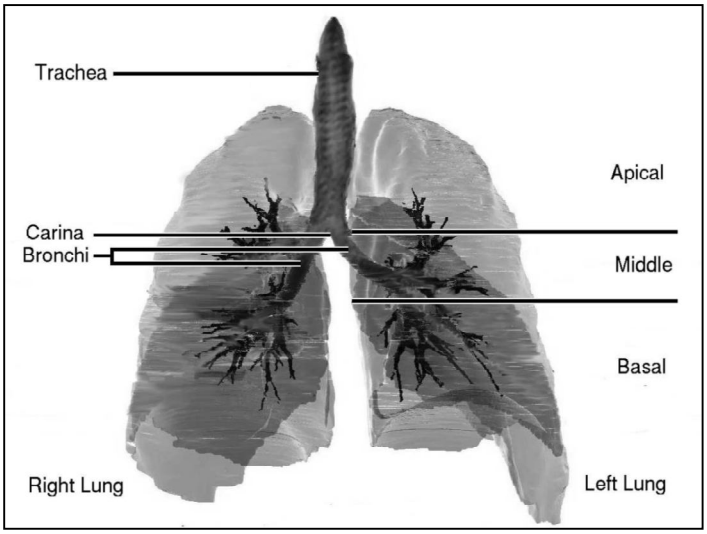

Figure 2.2 Further division of the lung regions [5]

Dividing the lung regions into three regions is not only important for lung disease detection, but it is also important for researchers to develop more reliable algorithms.

2.1.2 Lung HRCT Images

HRCT scanners generate a three dimensional view of the imaged organs in the axial section of the human lung, as shown in Figure 2.3(a). Each lung HRCT image is a two dimensional view of the imaged organs with sub-millimetre resolution. It provides high spatial and high temporal resolution for the pulmonary structures and surrounding anatomy so the detailed information of the imaged organs and lung nodules can be clearly seen from the images. Continuous lung HRCT images shown in Figure 2.3(b) are able to produce 3D volume data and enable precise imaged anatomy visualisation and disease pattern visualisation.

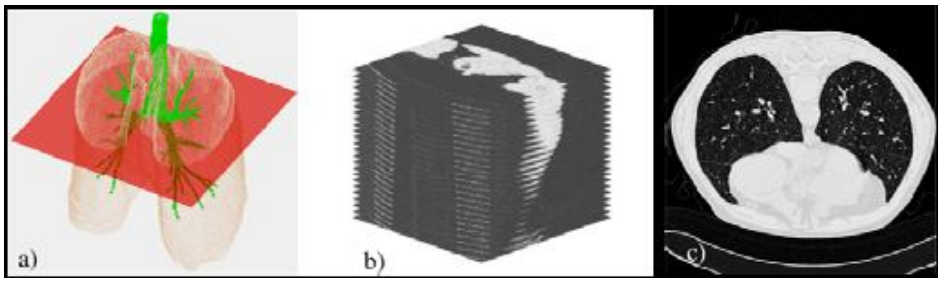

Figure 2.3 (a) Human lung (b) Continuous HRCT images (c) Normal HRCT slice [6]

In order to differentiate the HRCT images belonging to different lung regions, hilum is used as an anatomical landmark. Images located above the hilum belong to the Apical region, images containing the hilum belong to the Middle region, and images located below the hilum belong to the Basal region. Figure 2.4 shows a lung image belonging to the Middle region.

In this research, all the experimental data comes from the Bioengineering Group of the University of Otago, formatted according to the Dicom 3.0 Standard. A large amount of greyscale HRCT lung images are used to evaluate the performance of the proposed methods. Each image was stored and processed in RAW format, and has a size of 512x512 pixels, with a bit depth of 16 bits. For the given HRCT images, each image pixel corresponds to 0.68mm, and the nodule size is measured as the diameter of each nodule. The assumption that nodules will be present only in two or three consecutive slices is valid only for an HRCT stack with 1mm spacing.

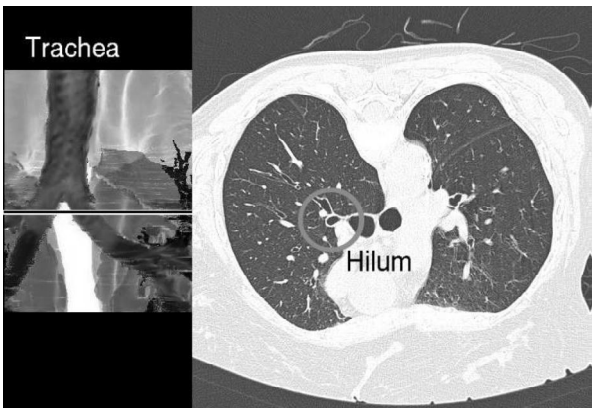

Figure 2.4 Trachea splits, top of the lung [5]

2.1.3 Lung Nodule Characterisation

Lung nodules usually appear as small regions with spherical, ellipsoidal or star shapes [7] [8] in the HRCT lung images. However, in practice, most of nodules are not perfectly spherical but exhibit very large variations in shapes, sizes and intensities, as illustrated in Figure 2.5.

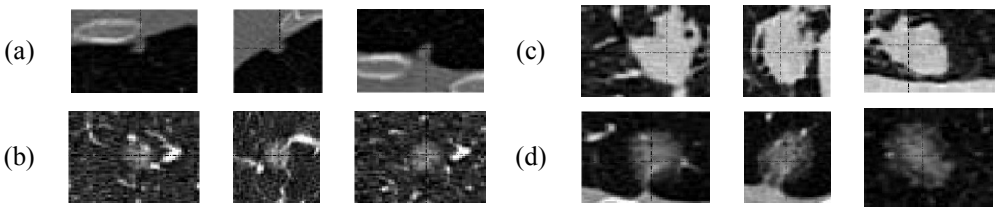

Figure 2.5 Illustration of different types of nodules: (a) Nodule attached to lung boundary (b) Vascularised nodules (c) Solid nodules (d) GGO nodules [9]

Lung nodules can be mainly categorised into two types: solid nodules can be characterised by their high-contrast and ground grass opacity (GGO), and nodules with faint contrast and fuzzy margins [10]. After observing a large number of HRCT lung images and spending a long time discussing nodule characteristics with radiologists, it's concluded that lung nodules have the following characteristics: (1) centroid locates inside of the nodule; (2) intensity higher than lung tissue and part of veins; (3) nodules appear on at least two consecutive HRCT slices, but no more than three consecutive HRCT slices. Figure 2.6 lists some sample cancer and non-cancer nodules.

Nodules							
Cancer	+	+	+	+	+	-	+
Nodules							
Cancer	+	+	+	-	-	-	-
Nodules							
Cancer	+	-	+	-	+	+	-

Figure 2.6 Cancer and non-cancer nodules [11]

2.2 Literature Review of Lung Image Processing Methods

Lung image processing is a fundamental step for most lung image analysis applications. HRCT images have been used for applications such as lung parenchyma density analysis [12], [13], airway analysis [14], and disease detection [15] [16]. In this research, lung HRCT images are used for nodule detection and analysis. Most of the CAD systems consist of two stages, the first of which is the lung segmentation, and the second is the characterisation of disease pattern.

In this section, common lung image processing techniques are explained. Section 2.2.1 gives a brief overview of current lung segmentation techniques. Section 2.2.2 reviews the relevant literature of nodule detection techniques.

2.2.1 Lung Segmentation

Current lung segmentation techniques can be classified as manual and automatic segmentation techniques. In many manual segmentation techniques, the processes such as lung boundary tracking, seed point allocation and lung anterior and posterior junction lines obtainment are manually processed. However, automatic segmentation techniques usually have a coarse lung segmentation step and a lung boundary optimisation step, and both steps are independently processed by the computer itself.

Manual Lung Segmentation

A number of successful manual techniques have been presented by several researchers: Denison et al. [17] used the manual lung boundary tracking method to estimate regional gas and tissue volumes in lungs; Kemerink et al. [18] developed a manually corrected border-tracing algorithm to segment the lung regions; Hedlund [19] introduced 3D region growing with seed points manually specified for segmenting the lungs; Kalender et al. [20] obtained anterior and posterior junction lines manually to separate the left and right lungs in cases where the edge contrast is reduced by the volume averaging.

Automatic Lung Segmentation

Several automatic techniques have been developed by a number of groups as manual segmentation became time consuming: Shojaii et al. [21] provided a lung segmentation technique based on a watershed transform and rolling ball filter. The watershed transform is used to find the lung boundaries and the rolling ball filter is used to smooth lung contours. Most lungs appear as dark regions in HRCT images and they are surrounded by the high density surrounding thorax region. The majority of the lung segmentation frameworks are based on grey-level thresholding. Figure 2.7 shows the lung segmentation result of Shojaii et al.'s method.

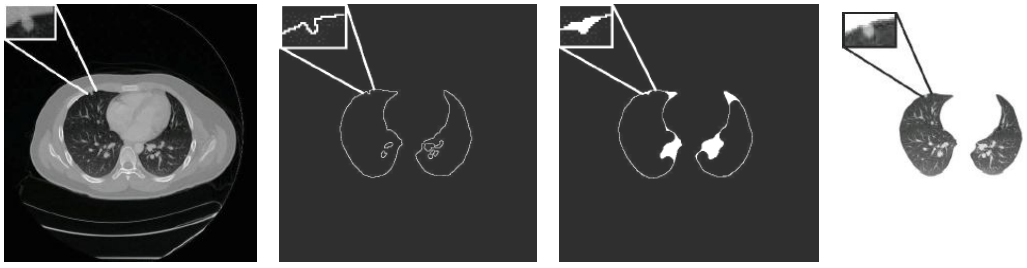

(a) (b) (c) (d)

Figure 2.7 (a) Original HRCT image (b) Segmented lung boundary (c) Smoothed lung boundary (d) Segmented lung regions [21]

Sluimer et al. [22] proposed a refined segmentation-by-registration scheme in which an atlas based segmentation of the pathological lungs is refined by applying voxel classification to the border volume of the transformed probabilistic atlas. It is

shown that this refinement step introduces a significant improvement in segmentation accuracy compared to a standard segmentation-by-registration approach. The method of Vinhais et al [23] consists of an initial step to segment the patient from the background of the image, an extraction step to identify the large airways, decomposing the lung parenchyma, and a final segmentation step to extract the lung regions. Figure 2.8 gives the lung segmentation result of Vinhais et al.'s method.

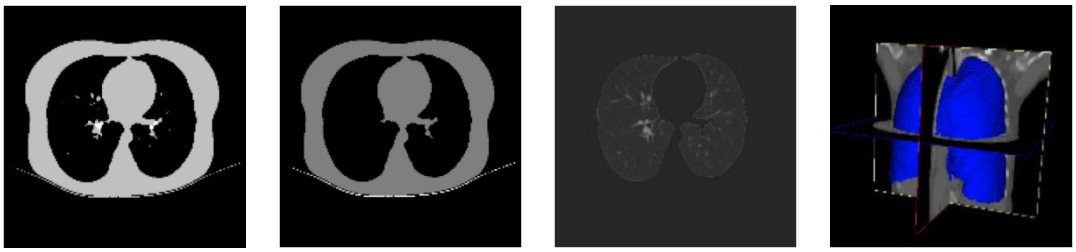

(a) (b) (c) (d)

Figure 2.8 (a) Constrained dilation of air voxels (b) Interior cavities elimination (c) Region of interest (d) Surface rending of the segmented lung regions [23]

Tseng et al. [24], developed a lung segmentation technique which is able to determine the threshold for each individual CT image and segment the lung regions automatically. Some output examples of Tseng's method are shown in Figure 2.9.

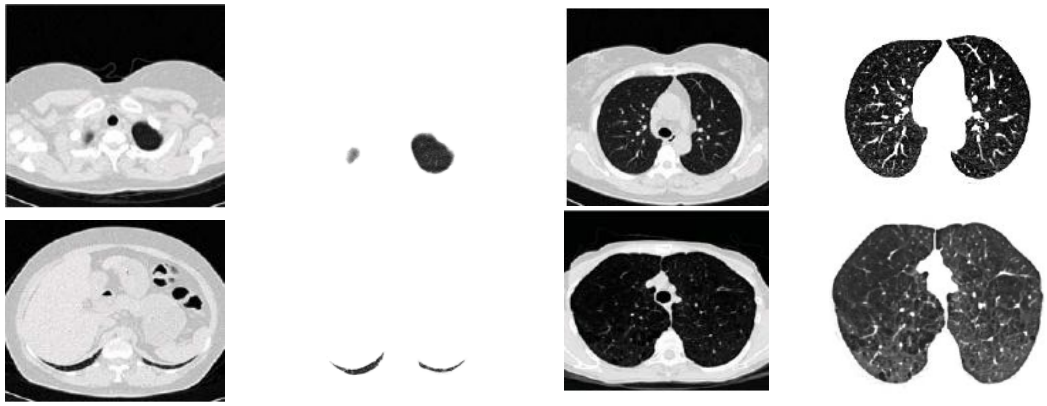

(a) (b) (c) (d)

Figure 2.9 (a) and (c) Original HRCT images (b) and (d) Corresponding segmented lung regions [24]

The shortcoming of the grey-level thresholding technique is it does not perform well if there is an intensity overlapping between the lung regions and a surrounding thorax region. Hu et al. [25] presented a way of comparing the result generated by the manual and the automatic segmentation technique. They use mean, RMS and maximum distance between the automatically extracted lung boundary and manually extracted lung boundary to assess the accuracy of the lung boundary position. According to their boundary difference calculation, they found that the greatest difference between the manually segmented lung boundary and automatically segmented lung boundary occurs on the lung boundaries near to the mediastinum.

The main advantage of lung segmentation techniques is that they minimise the nodule searching area for lung nodule detection.

2.2.2 Lung Nodule Detection

Lung nodule detection is the process of determining whether nodule patterns appear on the HRCT lung image and identifying the location of the nodules. Dr Giger and Dr Doi from the University of Chicago have shown that it is feasible for lung nodules to be automatically extracted from the X-ray radiography based on their features [26]-[27]. Currently, researchers have developed a number of lung nodule detection methods which can be classified as: classification based nodule detection (includes feature based nodule detection), template matching based nodule detection and clustering based nodule detection.

Classification Based Nodule Detection

The classification based nodule detection technique is the most widely used technique. Many machine learning methods are employed in the classification based nodule detection techniques such as artificial neural networks (ANN), support vector machine (SVM), *k*-nearest neighbour algorithm (*k*-NN), linear

discriminant analysis (LDA) and Bayesian classifier. Those machine learning methods are used to reduce the false positives in the lung nodule detection.

Suzuki et al. [28]-[29] developed a massive training ANN to detect both benign and malignant nodule patterns; Boroczky et al. [30] trained a SVM classifier on the subset of optimal features to identify the nodule candidates as nodule or non-nodule; Ginneken [31] implemented linear and non-linear *k*-NN regressions and SVM to predict the unseen nodule feature vector. Figure 2.10 gives three example nodules segmented by Ginneken's method.

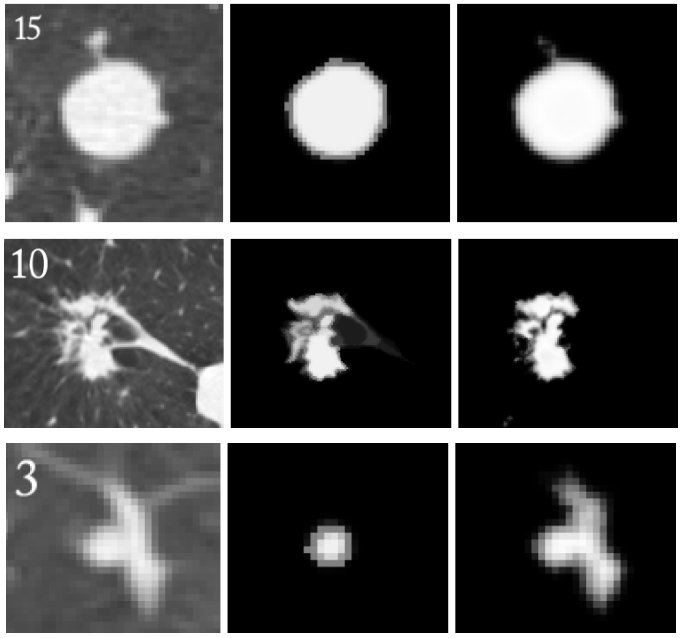

(a) (b) (c)

Figure 2.10 (a) CT data, axial or coronal sections zoomed in on the nodule with a lung window level, W/L = 1400/-600 HU (b) Truth (c) Segmented lung regions [31]

Matsumoto et al. [32] implemented a LDA classifier by using eight features to determine the intermediate nodule candidates. If multiple true detections corresponding to the same nodule were detected, the overall nodule was only counted as one. In order to compare the performance of different classifiers, Sluimer et al [33] employed LDA, *k*-NN, and SVM classifiers in their method to conduct an extensive evaluation. The result shows all the classifiers performed quite well, while the *k*-NN had a slightly better performance than other

counterparts; Klik et al. [34] also implemented multiple classifiers to classify benign sub-pleural nodules. They used *k*-NN, Parzen, LDA and quadratic discriminant to detect lung nodules, and they found LDA performed slightly better than its counterparts. Lin et al. [35] proposed a neural network model, Convolution Neural Network (CNN) architecture, to extract suitable features from chest radiographs and classify the nodules among the suspect nodule area (SNAs).

Feature based nodule detection uses the extracted nodule features to identify nodules. Most features relate to shape, size and intensity on the premise that nodules tend to be spherical and are of greater diameter, and they also have higher intensities than those of lung parenchyma. Kim et al. [36] developed a texture based classifier to classify the true nodules from nodule candidates based on features like shape, size, correlation coefficient and standard deviation;

Template matching Based Nodule Detection

Template matching based nodule detection is based on a simple model that simulates read nodules are the reference image. Several successful template matching based nodule detection techniques have been presented by several authors: Lee et al. [37] applied both semicircular matching and genetic algorithm to identify initial nodule candidates and attenuation, shape, and gradient feature rules to reduce false positives in the nodule detection; Figure 2.11 shows the eliminated and overlooked false positive candidates processed by Lee's method.

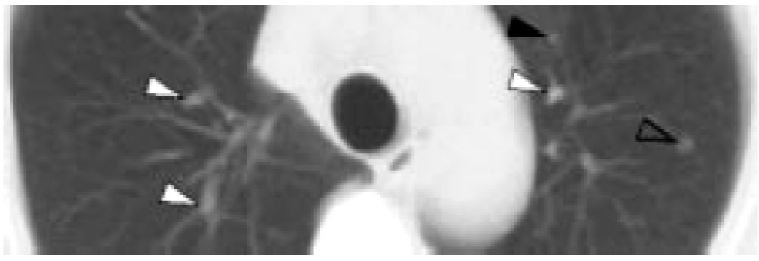

Figure 2.11 White arrows indicate false positive candidates removed by elimination process. A black arrow indicates a false positive candidate that remained after the elimination process. A transparent arrow indicates a detected nodule [37].

Dehmeshki et al [38] proposed a similar method with Lee [37], the only difference they made is they added a Shape Index (SI) parameter to the fitness Equation of the generic algorithm, which helps to improve the nodule detection result; Shigemoto et al. [39] proposed a template matching method base on using pre-defined nodule and vein models. The problem with this method is that the pre-defined models are not applicable for all types of lung nodules and it is unable to describe nodules with irregular surface and small size.

The weakness of the template matching based methods is it requires prior knowledge expressed by functions like Gabor or Gaussian [40] to pre-define all the different templates. However, it is difficult to pre-design the functions to accurately represent the various nodules.

Clustering Based Nodule Detection

The cluster based nodule detection techniques are mainly based on classifying lung regions into different number of clusters. A number of successful techniques have been presented by several researchers: Antonelli et al. [41] applied Fuzzy C-Means algorithm to classify the lung area in two clusters: nodule and blood veins are included in former, and the air is included in latter; Antonelli's method used the feed-forward four-layer neural network (FFN) architecture, which is seen in Figure 2.12.

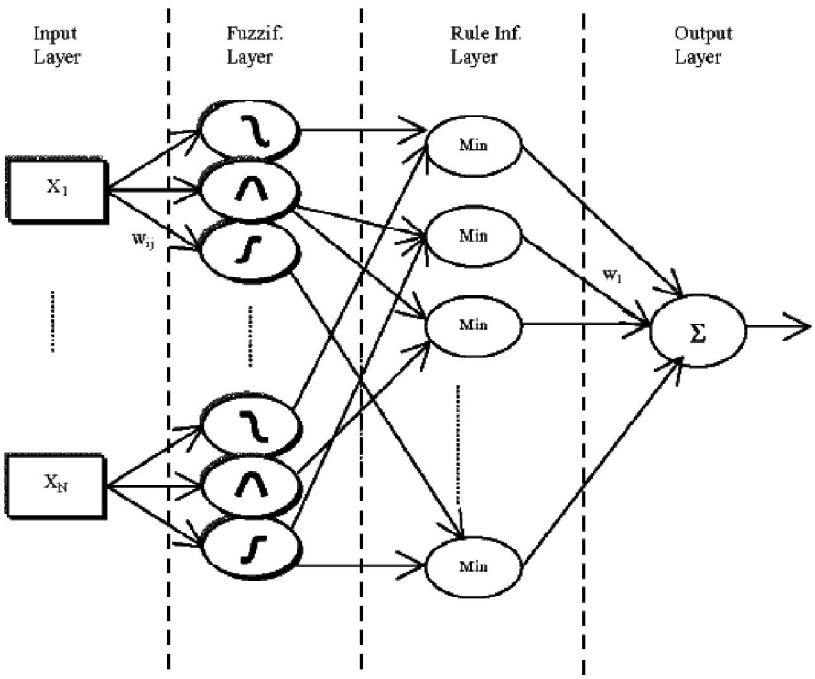

Figure 2.12 Architecture of the four-fuzzy neural network [41]

Kanazawa at al. [42] described a diagnosis rule based on fuzzy clustering, which is used to partition the histogram of pixels within the lung fields into three regions: “airway region”, “blood vein region”, and “tumour region”. They finally classify nodules and veins based on using similar features in a heuristic rule-based approach; Kawata et al. [43] proposed a linear discriminant classification method based on *k*-means clustering using benign and malignant lung nodule datasets based on topological histogram features.

Clustering approaches can be directly used to separate lung nodules from lung nodule candidates, and they can also be implemented to improve the lung nodule classification performance [8].

Chapter 3

Processing of HRCT Images

The intensity distribution in biomedical images is highly irregular and does not often permit a direct definition of shape parameters using geometrical descriptors. The Holder exponent [44], [45] is used in this research for resolving local densities variation in HRCT lung images. This chapter gives an overview of image representation followed by measuring the image intensity distribution based on the Holder exponent.

Section 3.1 gives a brief overview of image representation. Section 3.2 presents the Holder exponent for quantifying local density variation, and four different measures are discussed for the Holder exponent estimation. Section 3.3 discusses α-image generation and usage.

3.1 Image Representation

Each digital image is combined with a different number of pixels, each pixel having a particular location and intensity, as shown in Figure 3.1. As mentioned in Section 2.1.2 the HRCT lung images used in this research are in greyscale intensity and with 16 bit colour depth. So we consider 65536 levels of grey, from 0 (black) through to 65535 (white). Image pixels can be viewed from the enlarged lung junction image with size M×N in Figure 3.1, the location of each pixel is given by the co-ordinate (m, n) and intensity value at that pixel is g(m, n).

In order to make sure all the pixel intensity values extracted from the HRCT image are positive, each pixel intensity is normalised by adding the intensity value 65535 [46]. After normalising the intensity value for each pixel, the pixel intensities will be within the range [0, 65535].

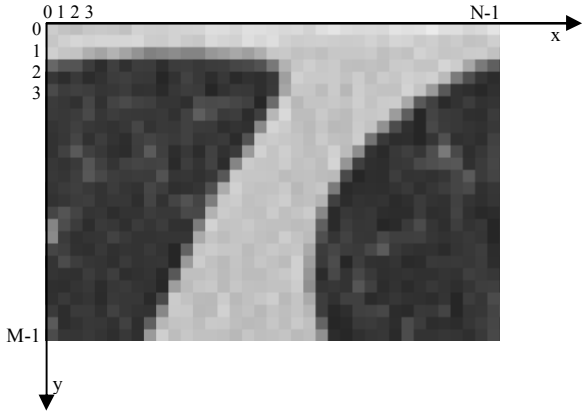

Figure 3.1 Enlarged lung junction image

The whole image can be represented as a 2D matrix with M rows and N columns:

$$g(m, n) = \begin{bmatrix} g(0,0) & g(0,1) & \dots & \dots & g(0,N-1) \\ g(1,1) & g(1,1) & \dots & \dots & g(1,N-1) \\ \vdots & \dots & \ddots & \dots & \vdots \\ g(M-1,0) & g(M-1,1) & \dots & \dots & g(M-1,N-1) \end{bmatrix}$$

3.2 Holder exponent α

The Holder exponent α [44] [47] [48] [49] [50] represents the degree of intensity variation at each pixel position in the image. It is estimated for each pixel (m, n) as the slope of the linear regression line of the plot of $\log_{\varepsilon} \mu(m,n)$ versus $\log \varepsilon$, for ε is the increasing size of the measure neighbourhood centred around the pixel (m, n). $\mu_{\varepsilon}(m, n)$ is the amount of intensity measured in the area. α-value computation is reflected by the local behaviour of a measure $\mu_{\varepsilon}(m, n)$, so choosing an appropriate measure is important for accurate α-value computation.

Some commonly used measures $\mu_{\varepsilon}(m, n)$, such as Sum measure, Iso measure, Maximum intensity measure and Inverse minimum measure for multi-fractal based analysis are based on pixel intensity, and introduced by Jacques Lévy Véhel and Pascal Mignot [51], and are defined by Nilsson [48] as follows:

$$sum: \mu_{\varepsilon(m,n)} = \sum_{(\kappa,\iota)\in\Omega} g(\kappa, \iota) \tag{3.1}$$

$$Iso: \mu_{\varepsilon(m,n)} = \#\{(k,l)|\ g(m,n) \equiv g(k,l), (k,l) \in \Omega\} \quad (3.2)$$

$$Maximum: \mu_{\varepsilon(m,n)} = \max_{(\kappa,\iota)\in\Omega} g(\kappa,\iota) \quad (3.3)$$

$$Inverse\ Minimum: \mu_{\varepsilon(m,n)} = 1 - \min_{(k,l)\in\Omega} g(k,l) \quad (3.4)$$

In the above Equations, g(k, l) represents the greyscale intensity value at pixel (m, n), ε is the size of the measure neighbourhood, and Ω is the set of all pixels within the measure neighbourhood.

In this research, we choose to use Sum measure for α-value estimation. Those four different measures are described in detail in Section 3.2.1-3.2.4. The comparative analysis of the four intensity measures is presented in Section 7.3.1.

3.2.1 Sum Measure

Sum measure is defined as the sum of the intensity value within a local neighbourhood. The local neighbourhood is usually in disc shape, square shape or diamond shape, and those shapes are known as neighbourhood shapes. Nilsson [48] summarised that different neighbourhood shapes can affect the estimation of the intensity measure $\mu_\varepsilon(m, n)$.

In this section, we discuss the Sum measure based on disc and square neighbourhood shapes; they are known as Multiple concentric discs and Multiple concentric windows:

- Multiple concentric discs: A measure $\mu_p(\delta)$ in a disc of radius δ at centre point p.
- Multiple concentric windows: A measure $\mu_p(r)$ in a square of size r at centre point p.

The results for both Multiple concentric discs and Multiple concentric windows are compared and analysed in Section 7.3.2. The comparison result shows Multiple concentric windows give better performance.

Multiple concentric discs and windows

In the Multiple concentric discs, we denote the measure function as $\mu_p(\delta)$, and δ represents the radius size of the disc region centred at a pixel p in which the measure is defined (see Figure 3.2(a)). The $\mu_p(\delta)$ stands for the intensity sum of the pixels inside the disc region with radius δ. In Multiple concentric windows, r represents the size of the square centred as pixel p in which the measure is defined in Figure 3.2(b). The $\mu_p(r)$ stands for the intensity sum of the pixels inside the square region.

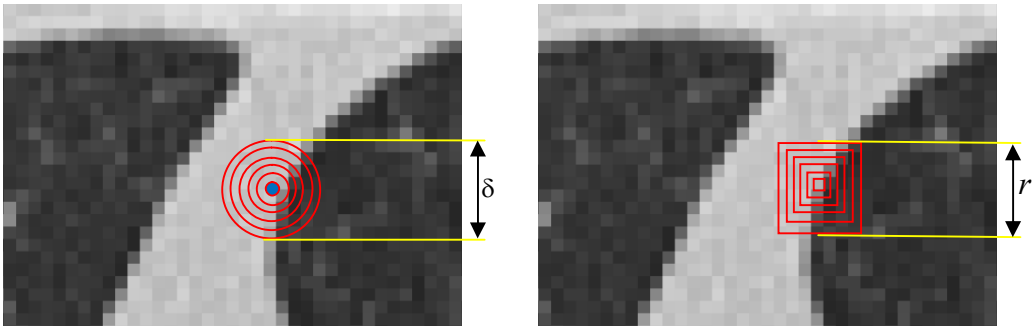

(a) (b)

Figure 3.2 Sum measure window shapes (a) Multiple concentric discs (b) Multiple concentric windows

In the Multiple concentric discs, the exponent at p is the term that shows how $\mu_p(\delta)$ scales with δ according to the power law in Equation 3.5. The exponent at p in Equation 3.6 shows how $\mu_p(r)$ scales with r for the Multiple concentric windows.

$$\mu_p(\delta) = C\delta^a \tag{3.5}$$

$$\mu_p(\mathrm{r}) = Cr^a \tag{3.6}$$

C is a constant in the above two Equations. The term α is an important term in characterising the variation of intensity. With the enlargement of the neighbourhood size, m denotes the total number of discs used in the computation of α in the Equation 3.7, and n denotes the total number of squares used for α computation in the Equation 3.8.

$$\delta = k, k = 0, 1, 2, \ldots, m. \tag{3.7}$$

$$r = 2k + 1, k = 0, 1, 2, \ldots, n. \quad (3.8)$$

Because of the neighbourhood shape difference between the Multiple concentric discs and the Multiple concentric windows, there is a difference in pixel increment. Figure 3.3 shows the neighbourhood size (δ) for the Multiple concentric discs increases one pixel at a time. Figure 3.4 illustrates the Multiple concentric windows have a neighbourhood size (r) which increases two pixels each time. The exponent α in the Equations 3.5 and 3.6 also establishes a mapping from the original image to an α-image, which is introduced in Section 3.3.

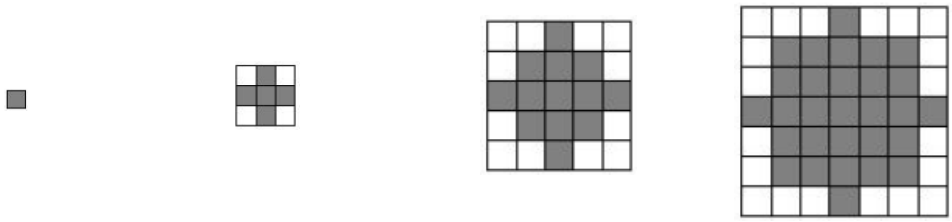

(a) $\delta = 1$ (b) $\delta = 2$ (c) $\delta = 3$ (d) $\delta = 4$

Figure 3.3 Neighbourhoods of $\delta = 1, 2, 3, 4$ respectively, for the centre pixel p [52]

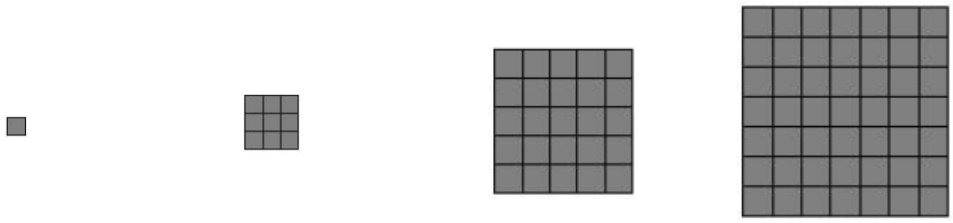

(a) $r = 1$ (b) $r = 3$ (c) $r = 5$ (d) $r = 7$

Figure 3.4 Neighbourhoods of $r = 1, 3, 5, 7$ respectively, for the centre pixel p [52]

As the δ value and r value for both Multiple concentric discs and Multiple concentric windows increase, the value of α at each pixel is estimated as the slope of the linear regression line through points on a log-log plot where $\log(\delta)$ and $\log(r)$ are plotted along the x-axis, and $\log(\mu_p)$ along the y-axis, as shown in Figure 3.5(a) and (b).

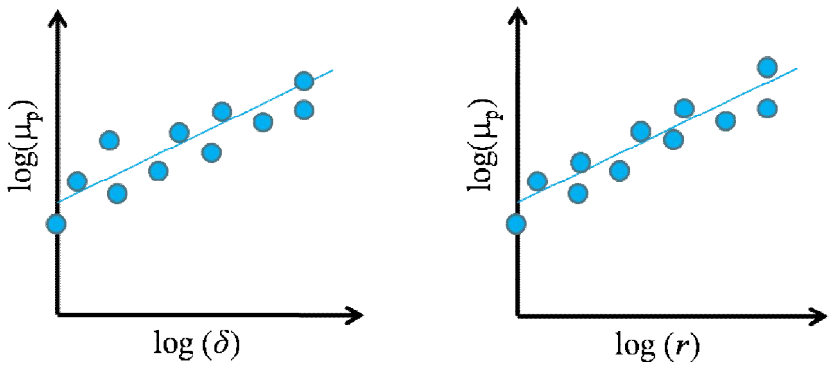

(a) (b)

Figure 3.5 Linear regression lines for: (a) Multiple concentric discs (b) Multiple concentric windows

3.2.2 Iso Measure

As seen in Equation 3.2, the Iso measure counts the number of pixels which have the same intensity value with the centred pixel (m, n) in a neighbourhood. The counted number of pixels is the measure $\mu_r(m, n)$.

3.2.3 Maximum Measure

Equation 3.3 defines the measure $\mu_r(m, n)$ to be equal to the intensity of the pixel with the greatest intensity in a neighbourhood. The greatest intensity value of pixel (m, n) is the measure $\mu_r(m, n)$.

3.2.4 Inverse Minimum Measure

In the Inverse Minimum measure, the $\mu_r(m, n)$ is the amount of measure in a neighbourhood to be 1 minus the intensity of the lowest intensity pixel in a neighbourhood, as shown in Equation 3.4.

3.3 Decomposition of an α-image

α-image is represented by a number of pixels, which have similar Holder exponent. It is used to show the pixels on an image that have similar degree of intensity variation, such as the pixels on object edges.

3.3.1 The α-image

Once α-values are calculated for each pixel in the original image, the α-image with the same size as the original image can be created. A 512×512 lung image has 262144 (512×512) α-values, which are sorted from minimum (α_{min}) to maximum (α_{max}). The intensity of each pixel in the α-image is set to represent the α-value of the corresponding pixel in the original image. In order to enhance the contrast of the α-image and see the brightest and darkest points which lie around the areas of strongest singularity, we display α-values in the full range [0, 1]. Figure 3.6 illustrates both the HRCT lung image and its α-image. Figure 3.6(b) shows that the pixels on the lung boundary have a similar degree of intensity variation, so α-images are also able to show object edges. Dawei et al. [53] used the Holder exponent for medical CT image edge detection, and edge detection result is shown by α-image.

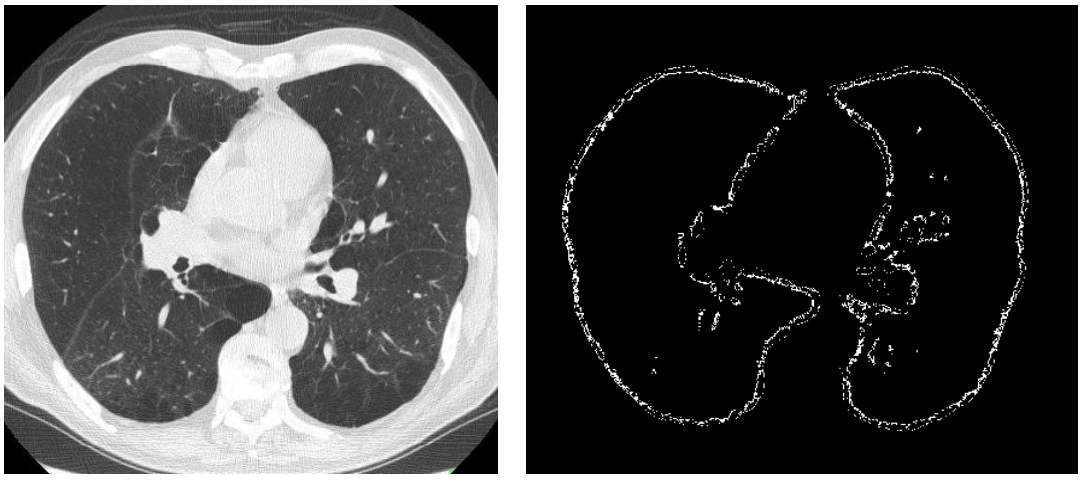

(a) (b)

Figure 3.6 (a) Original HRCT lung image (b) Corresponding α-image

3.3.2 Thresholding the α-image

The sorted α-values are further subdivided into n discrete intervals $\alpha_1, \alpha_2, \alpha_3, \ldots, \alpha_n$. Each interval α_k is defined as follows:

$$\alpha_k = \alpha_{min} + (k-1)\Delta\alpha_{k,}\ k = 1, 2, \ldots, n. \tag{3.9}$$

$$\Delta\alpha_k = (\alpha_{max} - \alpha_{min})/n \tag{3.10}$$

We choose n = 100 and for each sub-range k we threshold the α-image by considering only pixels with α-value in range $\alpha_k \leq \alpha < (\alpha_k + \Delta\alpha_k)$. We can then obtain the α-image by assigning the value 1 to these pixels, and 0 to all others. The α-image shows the pixels with α-values belonging to the same interval of [α_k, α_{k+1}], and those pixels have similar intensity variation [48] [49] [50]. The number of pixels belonging to each α-interval is counted, and most of the pixels have a Sum measure calculated α-value around value 2.0, as shown in Figure 3.7.

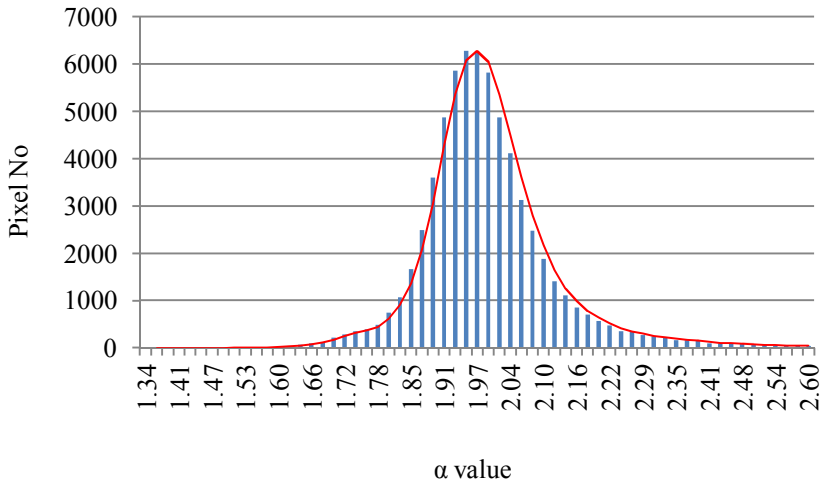

Figure 3.7 Image α-histogram

Choosing different numbers of intervals cause different α-image representation. Section 7.3.3 discusses how the different interval numbers reflect with the α-image representation.

Chapter 4

Lung Segmentation

In this chapter, a method is proposed to segment lung regions automatically from HRCT lung images. According to the region based intensity characterisation, the lung image can be considered as consisting primarily of three regions: the CT background, the lungs, and the thorax region surrounding the lungs. This method based on flood fill algorithm [54] is used to effectively identify the surrounding thorax region, as well as the CT background. This step facilitates the use of another fast method for the removal of the CT background using linear scans originating from border pixels. Connected components that represent parts of the trachea are removed by noting the separation of the mean and standard deviation of intensity values between the trachea and the lungs. The segmented lung images are further enhanced to restore the intensity values of the pixels on the bronchi and the lung boundary.

Figure 4.1 describes the structure of the proposed method, which consists of seven steps. An outline of these steps is given below.

a) Using a partitioning of the HRCT lung image into 16x16 boxes, a seed point position for the flood fill algorithm is automatically found in the body region.

b) The flood fill process is initiated with a pre-specified threshold value.

c) The flood fill method visits all pixels in a connected component of the body region.

d) A test is made to see if the flood fill has completely visited the surrounding thorax region. If the surrounding thorax is not completely processed, a new

flood fill seed point is automatically allocated in the unprocessed surrounding thorax region and the flood fill process will start again.

e) The region corresponding to the CT background is now removed using an iterative algorithm.

f) Non-lung connected components are removed from the extracted coarse lung regions based on their pixel intensity mean and deviation.

g) Lung regions and the airway region can be distinguished by their pixel intensity difference. A 3×3 horizontal and vertical dilation mask is applied to recover the lung information lost during the flood fill process.

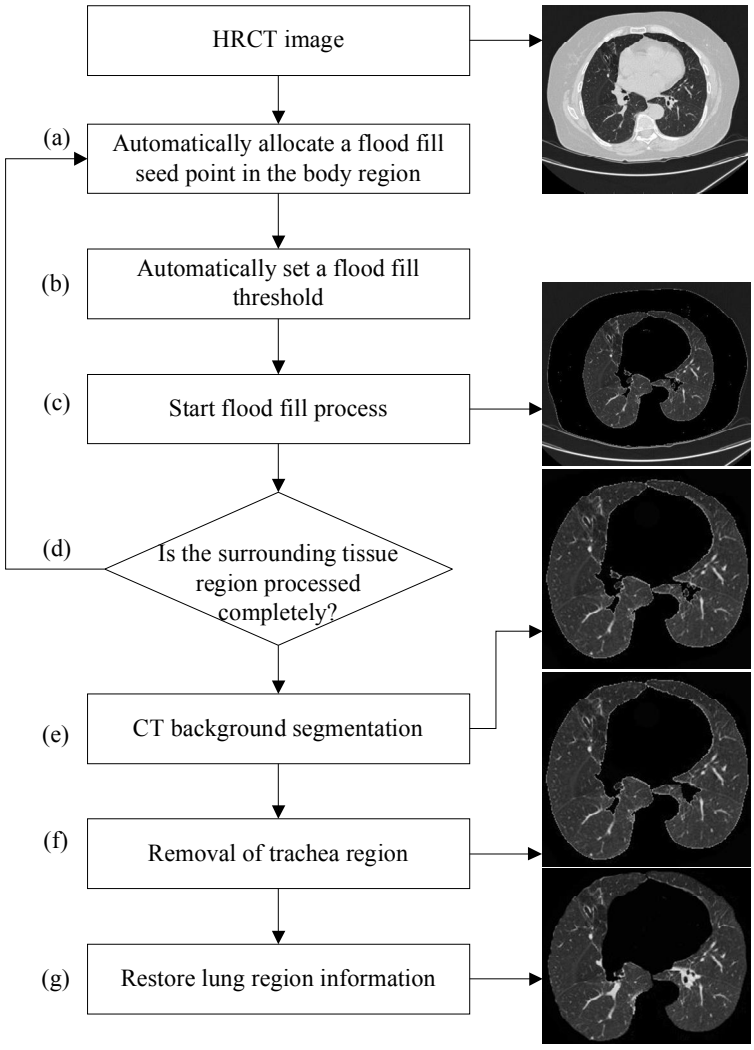

Figure 4.1 The flow chart of the lung segmentation method

Section 4.1-4.5 presents the proposed method based on well defined intensity characteristics of different regions of HRCT images, and use flood fill, linear scan and morphological operations to identify the exact lung regions. Section 4.1 describes the method for separating the lung background, the body tissue region surrounding the lungs and the lung regions. Section 4.2 describes a method for flood fill seed point allocation. Section 4.3 provides an overview of CT background segmentation by using linear scan method on the flood fill processed lung image. Section 4.4 presents a method of eliminating lung airways from CT lung images. Finally, lost lung region information is restored in Section 4.5.

4.1 Region Separation

In an average sense, the intensity values around a pixel in an HRCT image can be roughly categorised to three regions, as seen in Figure 4.2: (1) the CT background, (2) the body tissue surrounding lungs and (3) the lung regions. In healthy HRCT images, the intensity of the body tissue surrounding lung regions is higher than the intensity of the CT background and the lung regions. Our method takes advantage of this separation of intensity values, and uses the flood fill method to first identify the pixels corresponding to tissue in the thorax surrounding the lung.

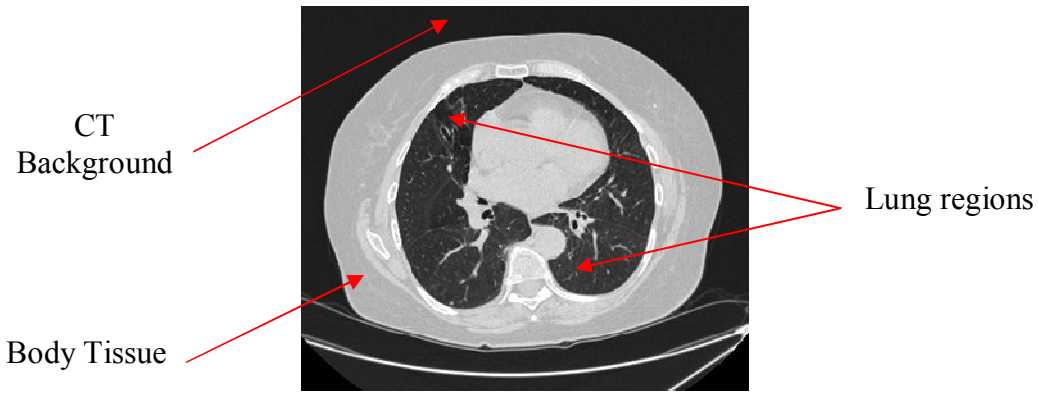

Figure 4.2 HRCT lung image regions

The flood fill method finds connected regions based on some similarity metric, and is used mostly in filling areas with colour in graphics programs [55]. In this proposed method, the flood fill method starts from a pixel that is called the seed

point, and looks for all the pixels in the array which are connected to the seed point. Any pixel connected to the seed point will be flagged if it has similar intensity with the seed point. The flood fill algorithm is recursively processed until all the connected pixels with similar intensity are processed. The flood fill algorithm pseudo code is given in Appendix A.1. Once this process is complete, the region outside this segment can be identified as the CT background region, and the region inside this segment can be identified as lung regions. The CT background region can be easily identified using a fast linear scan from each border pixel.

Figure 4.3 shows the pixel intensity mean difference between the lung regions, body tissue region, and the CT background, computed from several HRCT image slices. The pixel intensity values range from 0 to 65535. Figure 4.3 also suggests that a threshold of T_1 = 15000 would be adequate to initiate a recursive flood-fill in the body tissue region. It is feasible to separate the body tissue region with the lung regions and the CT background region by using the threshold T_1 = 15000. The main task here is to identify a seed pixel in the region, and also to make sure that all possibly disjoint, sections of this region are visited by the algorithm.

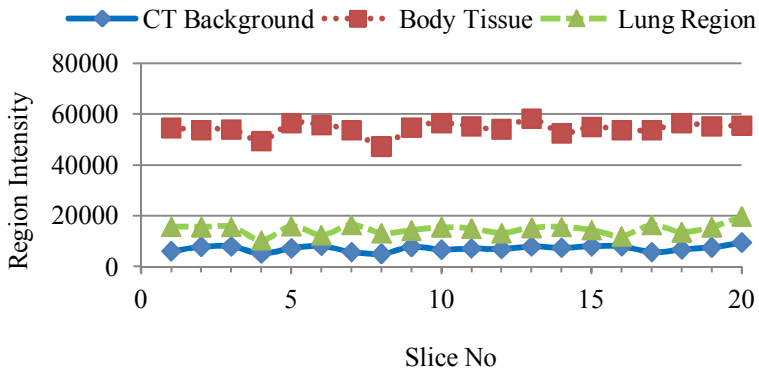

Figure 4.3 Intensity difference of the three main regions

4.2 Automatic Seed Point Selection

As seen in the previous section, the body tissue region is located in between the CT background and the lung regions in HRCT lung images. Implementing the flood fill method in the body tissue region can therefore separate the CT

background and the lung regions. The seed point is defined as the point with the maximum intensity within a neighbourhood of 16×16 pixels having intensity values in the upper region of Figure 4.3. A 16x16 window is found to adequately characterise the nearly uniform distribution of intensities in a neighbourhood, and it also provides the average intensity within the window. Increasing the window size further increases the error in describing uniform distributions, while reducing the window size makes it more sensitive to intensity variations. The HRCT image is therefore divided into 16×16 cells R_{ij}. where i, j = 1,…,32, and the average intensity r_{ij} in each cell is computed. Cells with average intensity greater than T_2 = 45000 contain only pixels belonging to the surrounding thorax region. We select the cell G with the maximum average intensity $g = \max_{ij}(r_{ij})$, and define the seed point as the pixel with the highest intensity in G. The previous steps are guaranteed to provide a cell in the body tissue region, and a seed point in that region (see Figure 4.4(a)). A recursive 4-connected flood fill algorithm using the threshold T_1 visits an entire connected component within this region (see Figure 4.4(b)). All visited pixels and cells are marked, and the whole process is repeated if another component of unmarked cells with an average intensity greater than T_2 exists. In Figure 4.4(a), such disjoint components exist because of the anterior and posterior junctions (indicated by arrows). So, checking for the completeness of the flood fill process is an essential step for lung segmentation.

Please note that parts of the bronchi also have similar intensity values as the surrounding thorax and may get removed by the flood fill operation (see Figure 4.4(b) and (c)). These removed regions will be recovered at a later stage (see Section 4.5).

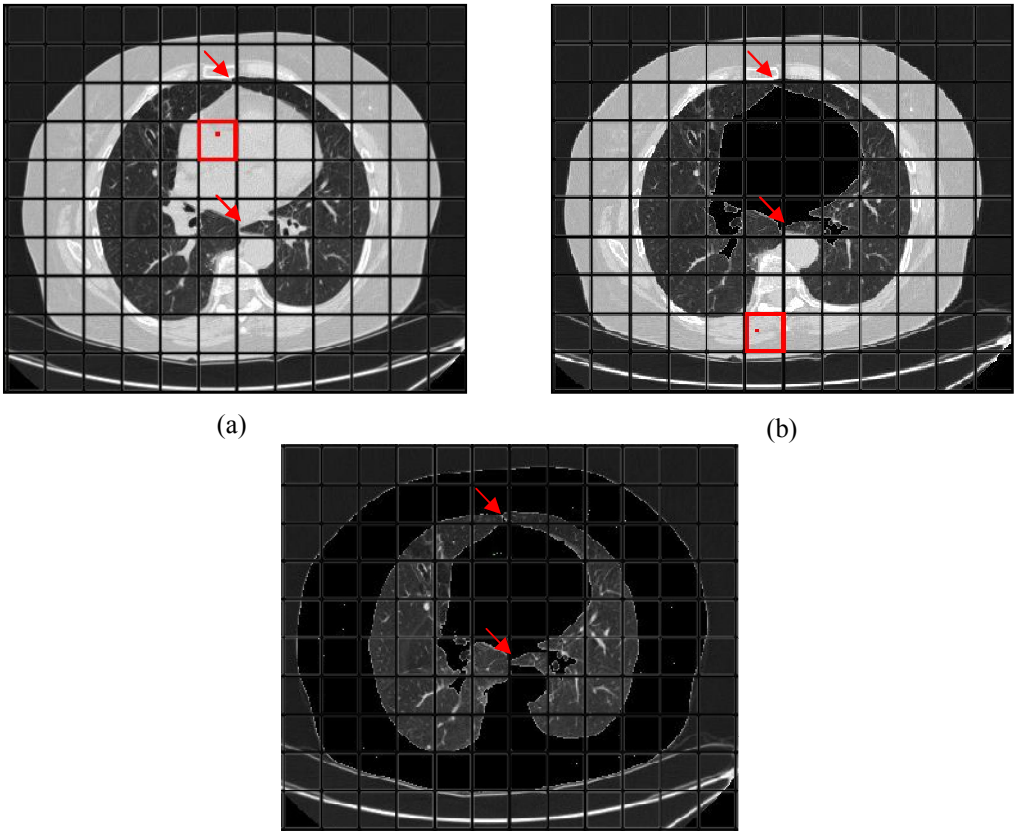

(a) (b)

(c)

Figure 4.4 Process of flood fill (a) First seed point allocation (b) Second seed point allocation (c) Identification of the complete surrounding thorax region using flood fill

4.3 CT Background Segmentation

Having marked the entire body region surrounding the lungs, the next task is to identify the exterior of this region, which is the CT background. This is done by initiating a linear scan from each border pixel towards its pair on the opposite border, marking off each pixel and stopping the scan when a pixel belonging to the surrounding region is encountered. Since, in the most general case, the surrounding region has a non-convex shape, it is necessary to perform both a horizontal scan (from left and right border pixels) and a vertical scan (from top and bottom pixels) to completely remove all external pixels belonging to the CT background. The process is illustrated in Figure 4.5. The time complexity of the horizontal and

vertical scan is represented by big-O notation. The size of the image is $N \times N$, so the scan process requires $O(N \times N)$ time to execute.

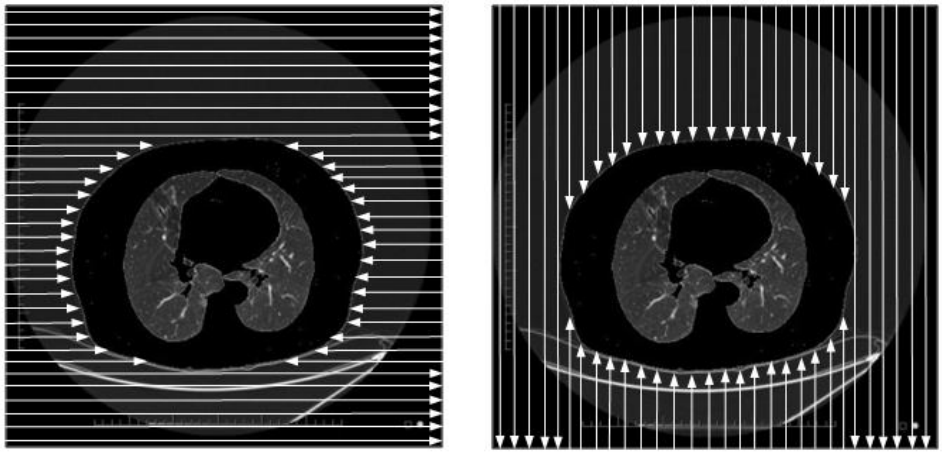

(a) (b)

Figure 4.5 (a) Horizontal scan (b) Vertical scan

Figure 4.6 shows the coarse lung regions with the exterior of the body tissue region removed. Airways (trachea and bronchi) and lung regions are left over in the coarse lung regions image.

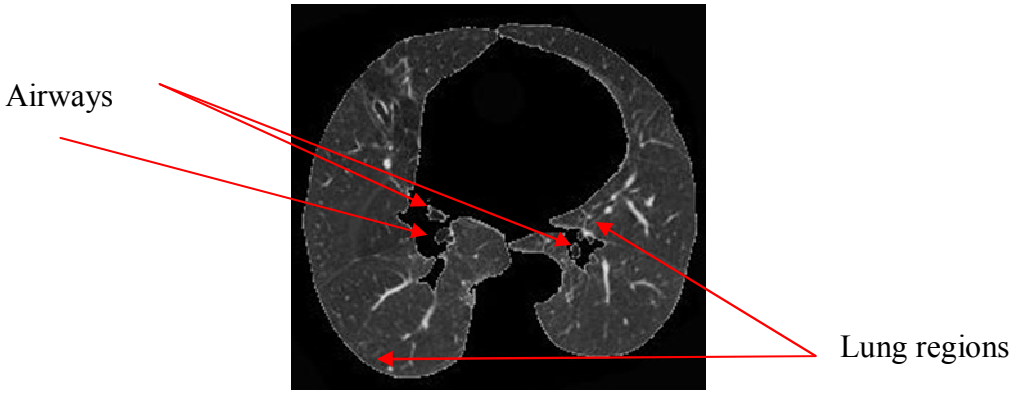

Figure 4.6 Coarse lung regions

4.4 Removal of Trachea Region

A number of authors have developed techniques for detecting lung airways from CT lung images [56]-[57]. In [25], Hu et al. used a slice-by-slice region growing method to remove airways and used the airway's location on the current CT slice to estimate the airway's location on the next slice. However, the slice-by-slice region

growing method is not capable of segmenting the airways on some transverse slices [58].

In our method, we consider specific characteristics of the intensity distribution within the lung regions to identify and remove image segments that correspond to the airways. The images shown in Figure 4.7 have two things in common. Firstly, the trachea region has lower pixel intensity than the lung regions. Secondly, the presence of veins in the lung regions makes the lung regions vary in pixel intensity. So the lung regions have higher pixel intensity mean and deviation than the airway region.

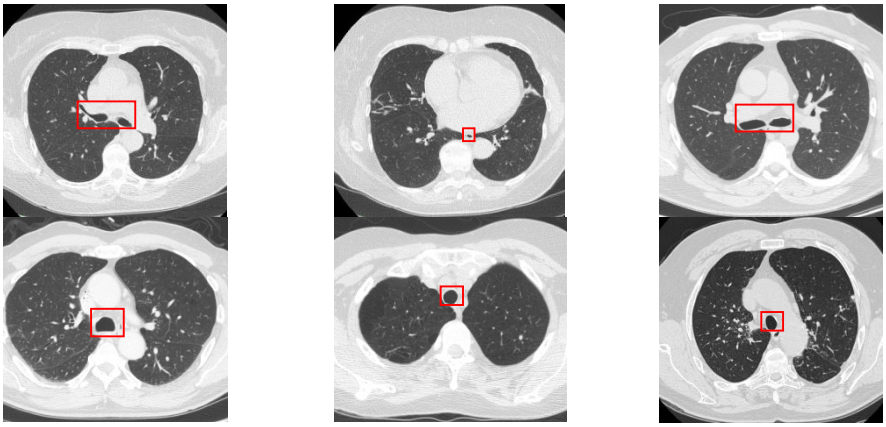

Figure 4.7 Air filled regions vary in size, location and shape

Figure 4.8 indicates the pixel intensity mean and deviation difference between the trachea regions and the lung regions. This separation in the intensity space can be effectively used for identifying connected components that represent parts of the trachea.

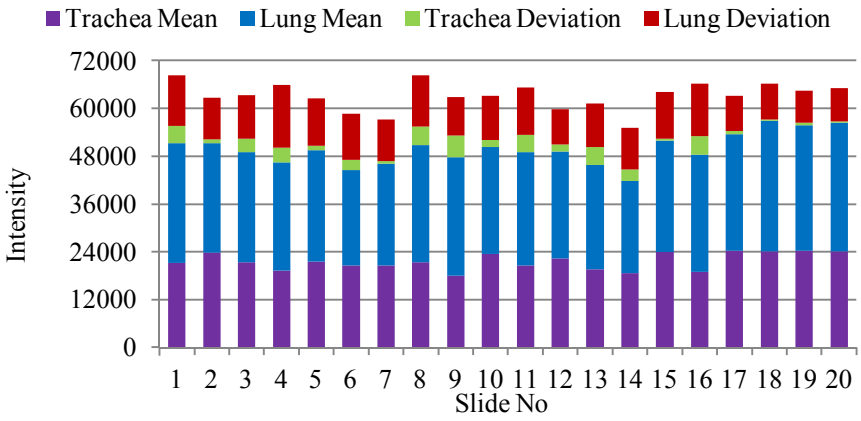

Figure 4.8 The statics of lung and trachea

Each connected component in Figure 4.6 is labelled with a positive number, as shown in Figure 4.9. The labelled connected components are further processed to determine its shape and size. In our case, we will also need to calculate the pixel intensity mean and deviation for each connected component. If a specific connected component belongs to the trachea region according to its pixel intensity mean and deviation, this region will be discarded. Figure 4.8 suggests that the thresholds of trachea mean $T_m = 20000$ and trachea deviation $T_d = 50000$ would be adequate to remove the trachea region. A labelled connected component has to be removed if it has intensity mean $< T_m$, or intensity deviation $< T_d$.

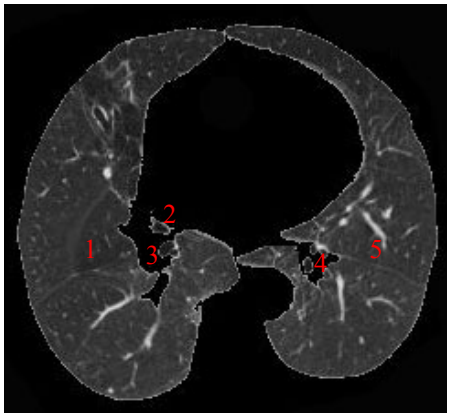

Figure 4.9 Labelled coarse lung regions

Labelling the connected components is done by two steps, which are seed image generation and label image generation. Both steps are performed on the coarse lung regions image (see Figure 4.6).

a) Seed image generation: Seed image is generated by assigning two different numbers to non-background (non-black pixels) and background (black pixels) pixels as seen in Figure 4.9. The non-background pixels are assigned with number 1, and the background pixels are assigned with number 0. The number 1 and 0 are only used to differentiate the background pixels and non-background pixels.

b) Label image generation: Label image is generated by assigning different label numbers to the connected components with pixels numbered by 1 on the seed image. In Figure 4.10, the grey cells in the enlarged window represent the non-background pixels, and the black cells represent the background pixels. The number labelling process scans the seed image pixel by pixel. Once any non-background pixel is scanned, all its connected non-background pixels in eight directions are assigned with a label number. The label number increases as more and more connected components are scanned. Labelled connected components are easy to be extracted and analysed by using its label number.

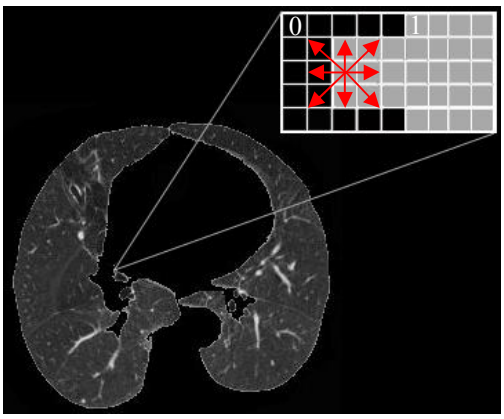

Figure 4.10 Connected components labelling

Each labelled connected component in Figure 4.9 can be picked out for determining its pixel intensity mean and deviation. Decisions can be made to either keep or discard the connected components on the coarse lung regions image. Figure 4.11 outlines the procedure of eliminating trachea regions from labelled coarse lung regions image, which is represented in three steps:

a) Each labelled connected component in the Figure 4.9 is picked out based on its label number.

b) Calculating the pixel intensity mean and deviation for each labeled connected component.

c) A test is made to see if any connected component has similar pixel intensity mean and deviation with the pixel intensity mean and deviation of the trachea. If a connected component has similar pixel intensity mean and deviation with the trachea region pixel intensity mean and deviation, then the connected component needs to be eliminated. Otherwise the connected component is kept in the coarse lung regions image.

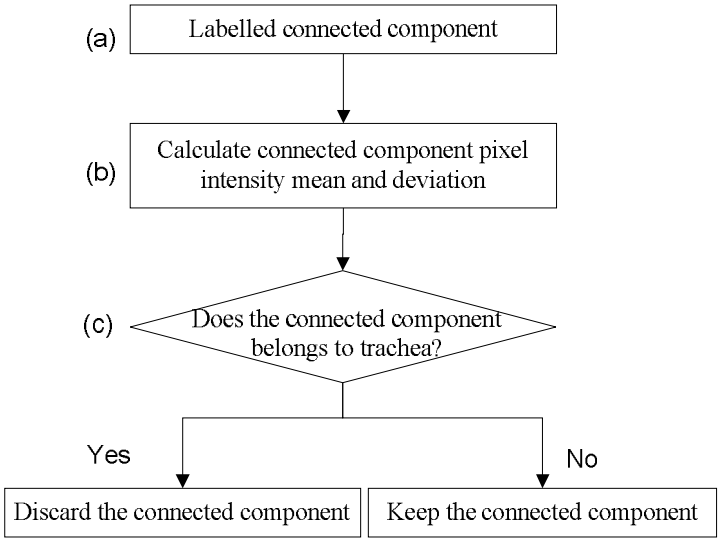

Figure 4.11 Trachea elimination procedure

Figure 4.12 shows trachea regions are removed by the trachea elimination procedure. The next section is to restore the bronchi regions (indicated by arrows in Figure 4.12) removed by the flood fill process on the coarse lung regions.

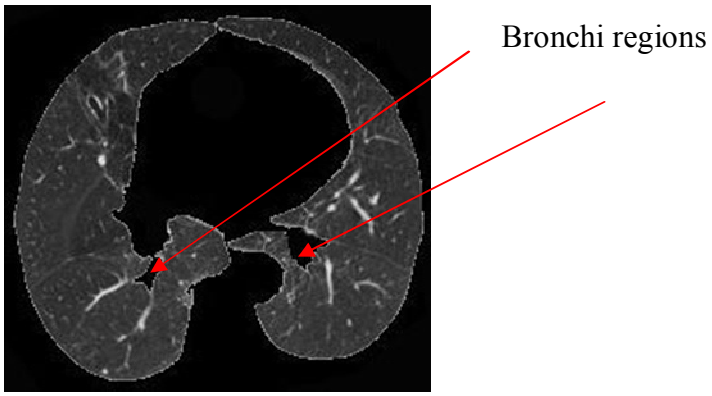

Figure 4.12 Coarse lung regions with tracheas removed

4.5 Restoring Lung Regions Data

Bronchial walls, veins and nodules have generally higher intensity compared to the average lung regions and if they are near the boundary of the lung regions they will most likely get removed by the flood fill process. Figure 4.13(a) shows a lung nodule located on the lung boundary (indicated by a red arrow). In Figure 4.13(b), the lung nodule is lost after the flood fill process. Restoring the lost pixel information within the lung boundary is important for proper segmentation. We propose a method below for accurate reconstruction of the lung image region.

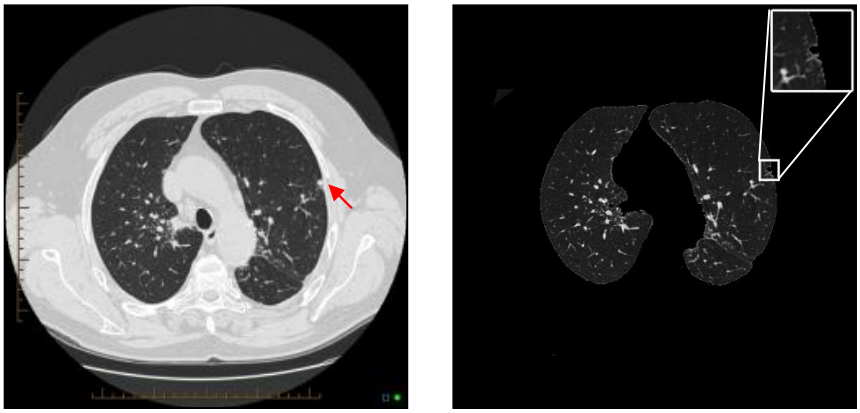

(a) (b)

Figure 4.13 Lung boundary information lost (a) Lung nodule locates on the lung boundary (b) Lung nodule pixels are affected by the flood fill process

4.5.1 Morphological Dilation

In greyscale morphology, the operation of dilation is used for region growing. This operation also closes holes and gaps within the region. Dilation makes an object larger by adding pixels around its edges [59]. The four most basic operations in mathematical morphology are dilation, erosion, opening and closing, and their corresponding effects are illustrated in Appendix A.2. Figure 4.14 shows four 3×3 dilation masks.

Vertical mask	Horizontal mask
0 1 0	0 0 0
0 1 0	1 1 1
0 1 0	0 0 0
Horizontal and Vertical masks	
0 1 0	1 1 1
1 1 1	1 1 1
0 1 0	1 1 1

Figure 4.14 Horizontal and vertical mask [59]

In order to close the lung gaps completely, we convolve the image with the dilation mask 4 times. Four times of dilation is reasonable enough to close up common size lung gaps although more dilation times are still feasible. However, increasing dilation times causes longer lung segmentation processing times. It also increases the amount of noise, which affects the segmentation accuracy.

An example of this application is shown in Figure 4.15(a) and (b). The operation increases the intensity of all pixels within the region, and closes gaps that resulted from the flood fill operation. The border also expands by four pixels. We now replace all non-zero intensity pixels in this image with the corresponding pixels from the original lung image. This operation yields a result, as shown in Figure 4.15(c), where the bronchi regions have been restored. This image also has a four-pixel wide border as a result of the region growing by dilation, and copying of the corresponding pixels from the surrounding region.

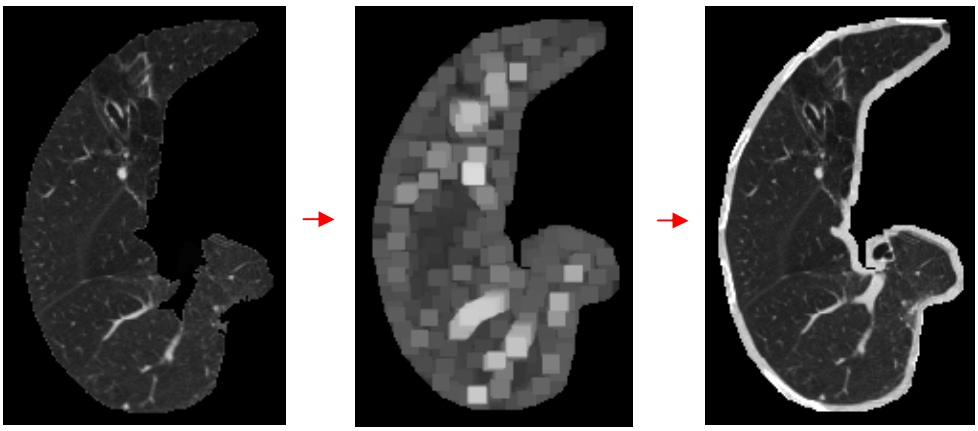

(a) (b) (c)

Figure 4.15 (a) Lung regions after flood fill and CT background removal operations (b) Result of applying the dilation mask four times (c) Dilated lung regions shown by original pixel intensity

Figure 4.16 shows the result of the above sequence of operations when the image is dilated only once, twice, three and four times. A four-step dilation is used primarily to close the gaps represented by the bronchi.

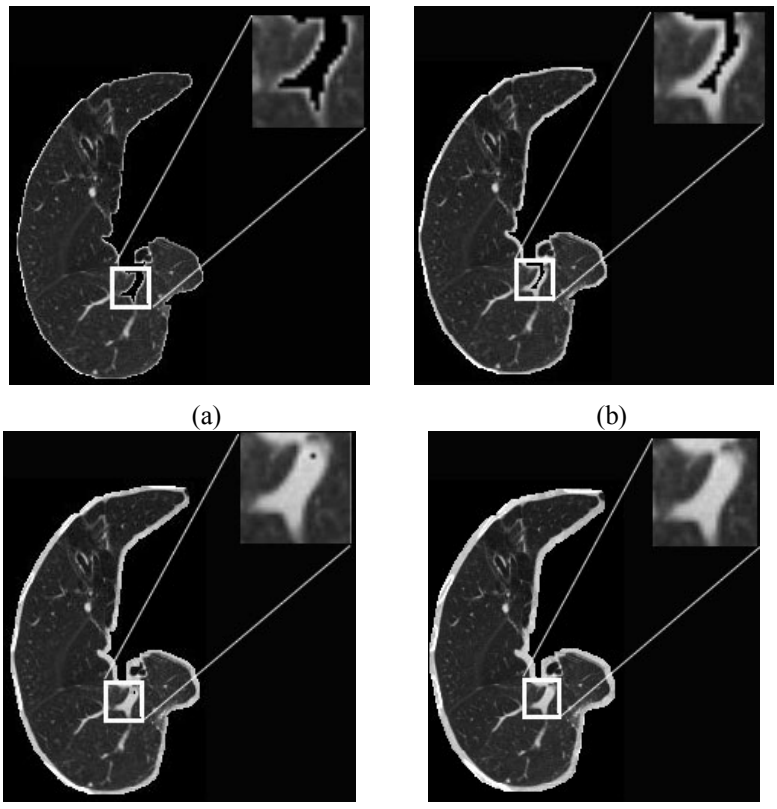

(a) (b)

(c) (d)

Figure 4.16 (a) dilation×1 (b) dilation×2 (c) dilation×3 (d) dilation×4

4.5.2 Lung Boundary Enhancement

In Figure 4.17, the grey cells in the middle of the enlarged window represent the pixels from the body tissue region which were copied from the original image to the lung boundary. The cells marked with numbers are the labelled pixels in the lung regions and the black cells correspond to the background pixels. A scan-line algorithm is used to find the edge pixels which are adjacent to the black background pixels. Every edge pixel has a background pixel included in its eight neighbouring pixels and is also not part of the lung regions. Each scan-line strips off edge pixels found on it by setting their pixel intensity to zero. Repeating the process four times removes the four-pixel wide border introduced by the dilation operation.

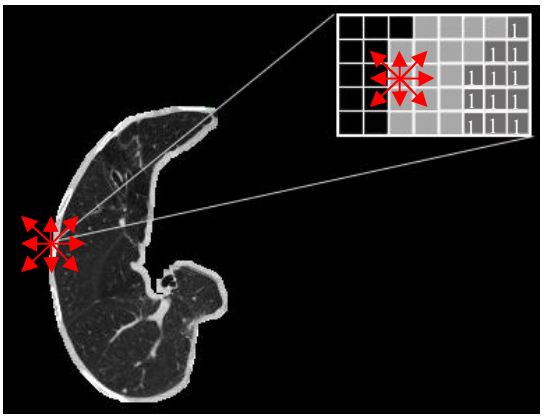

Figure 4.17 Optimise lung boundary

The results of the edge peeling process for our sample image are shown Figure 4.18(a)-(d). In Figure 4.18(d), the border containing pixels from body tissue is completely eliminated. Note also the interior of the lung regions now contains the original pixel intensities.

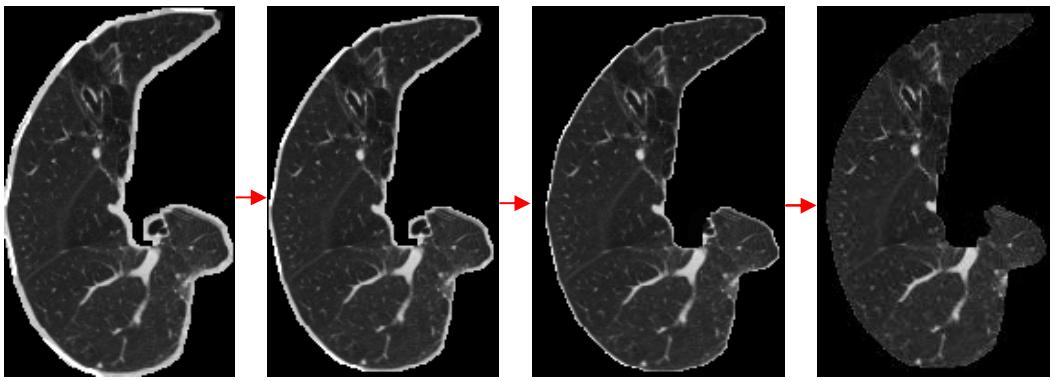

(a) (b) (c) (d)

Figure 4.18 (a) Edge peel ×1 (c) Edge peel ×2 (d) Edge peel ×3 (e) Edge peel ×4

4.6 Summary

The proposed lung regions segmentation technique is based on flood fill and morphological operations to effectively segment lung regions of varying size, shape and location from HRCT images. Using the statistical characteristics of the intensity distribution, it is possible to easily distinguish, the lung and the airway.

The advantages and the limitations of the lung regions segmentation technique are listed as follows:

Advantages of the proposed technique

- The method is fully automatic; it does not require manual input of seed points or interactive selection of regions.
- The method provides accurate segmentation of the lung regions, and effectively removes the trachea regions and the surrounding region of the thorax.
- The pixel intensity values within the interior of the lung regions after segmentation are the same as the original image.

Limitations of the proposed technique

- The method involves several stages of processing using morphological operators.

Chapter 5

Lung Nodules Detection

The previous chapter described the lung segmentation technique for segmenting lung regions, which minimises the nodule detecting area on lung images. However, the existence of the non-nodule noise information inside the lung regions still affects the nodule detection accuracy. In this chapter, an effective lung nodule detection technique is proposed which takes both the grey-level distribution and the object shape into account. The nodule detection technique handles a set of consecutive HRCT slices that includes images with and without nodules. Nodule candidates are generated by combining the α-images that contain nodule information. Each lung image has a combined α-image that contains a different number of nodule candidates and nodules. Most of the nodule candidates are filtered and removed by comparing their characters with nodule characters. Their shape features are determined by implementing nodule radii ratio metric and nodule area ratio metric. Determined nodule candidate shape features are compared with nodule shape features to identify nodules.

Section 5.1 overviews the whole method for nodule candidate extraction. Section 5.2-5.3 explains the method in detail, which includes combining α-image generation and nodule candidates filtering. Section 5.4 presents the technique for detecting nodules based on shape feature comparison between the nodule candidates and nodules.

5.1 Nodule Candidates Extraction Overview

Nodule candidate extraction and filtering is an important image pre-processing step, which is employed to reduce the number of false positives in nodule detection.

Figure 5.1 shows the key steps of the nodule candidate extraction process, and takes up two pages due to its large information presentation. Each step is represented by a row (a) to (f), and each image in the set is numbered from 1 to 5, as shown in Figure 5.1. Nodules are indicated by red arrows on the various images in Figure 5.1. The whole process is presented by the following steps:

a) A set of consecutive HRCT slices for nodule detection is loaded.

b) Lung regions are segmented by using the lung segmentation technique presented in Chapter 4.

c) α-images are generated for each segmented lung image, and the ones containing nodule characteristics are combined in Section 5.2.

d) According to the nodule centroid and intensity discussed in Section 2.1.3, the nodule candidates with gravity points located outside or having low intensity are removed.

e) The nodule candidates processed by step (d) that have less than 75% of their pixels appearing in the next combined α-image are eliminated. However, the nodule candidates identified as nodules in the previous combined α-image will need to be kept.

f) If any of the nodule candidates processed by step (e) still has its pixels appearing on its next third continuous combined α-image, then the nodule candidates is removed.

The above six steps eliminate most of the non-nodule information that exists inside the lung regions. Step (c) performs nodule candidate extraction by combining the α-images that contain nodule information, which is described in detail in Section 5.2. Section 5.3 describes the rule based filtering process, which explains how step (d), (e) and (f) work for false positives elimination. The nodule detection process introduced in Section 5.4 is performed on those filtered nodule candidates.

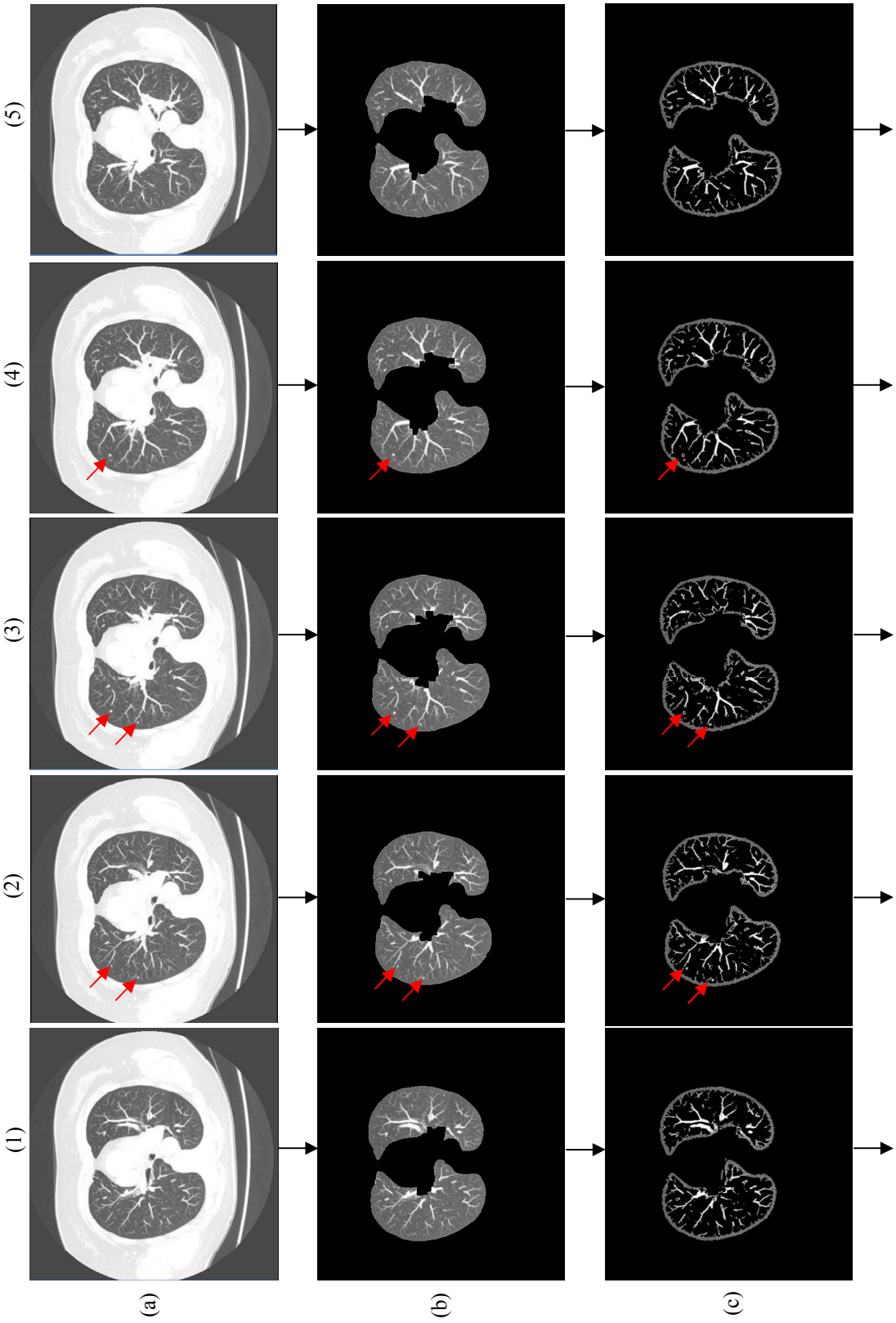
(1)
(2)
(3)
(4)
(5)
(a)
(b)
(c)

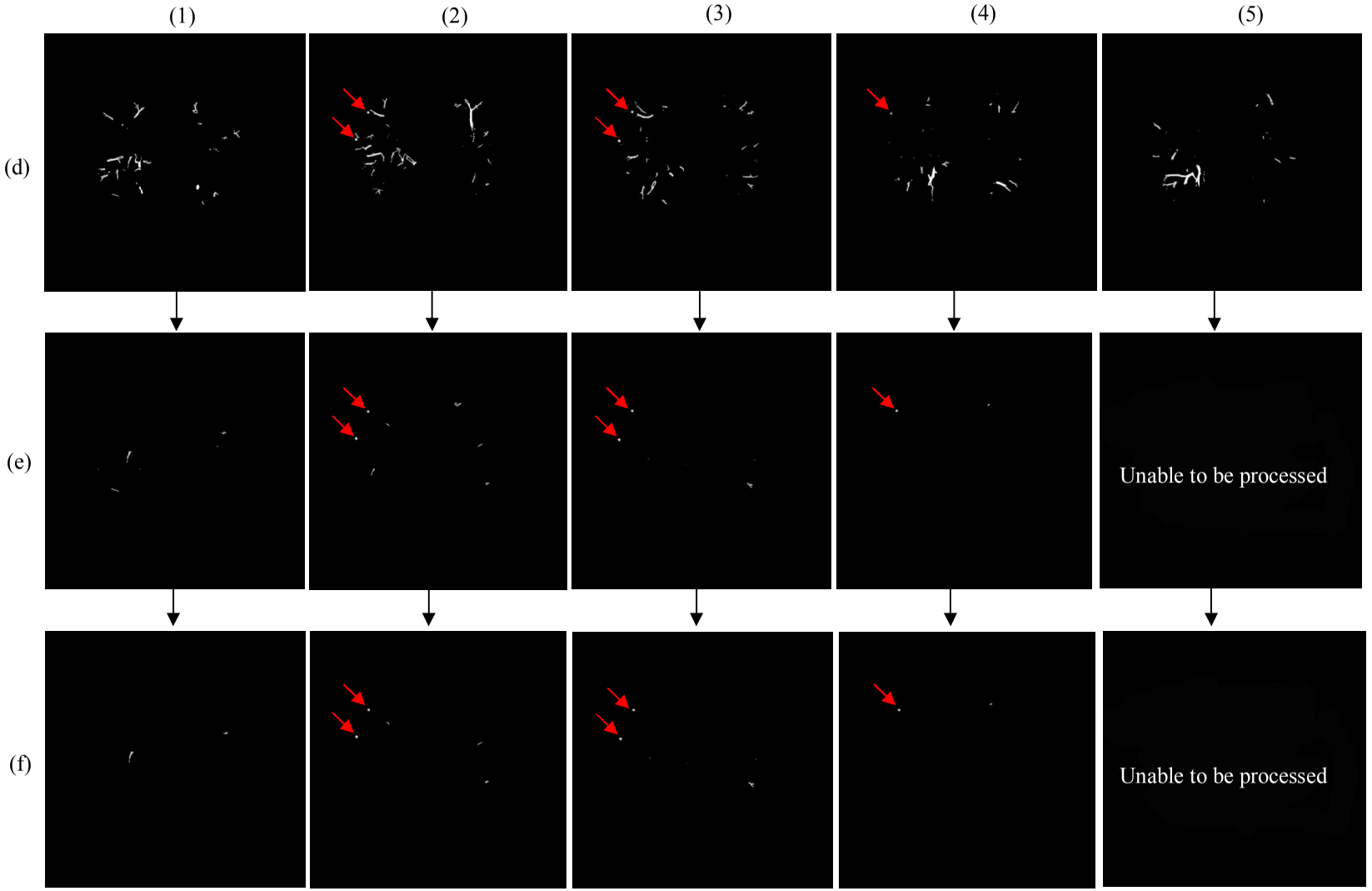

Figure 5.1 Nodule candidates extraction

In Figure 5.1(b)-(d), the images are processed by lung segmentation, α-images combination and rule based filtering processes. The majority of non-nodule information is eliminated after the step (b)-(d) processing. For example, the processed images shown in Figure 5.1(d)(2)-(4) only contain a few number of high intensity veins and the nodules need to be detected.

In Figure 5.1(e)-(f), images are processed by the rule based filtering process. For example, the nodule candidates shown in Figure 5.1(e)(1) are generated by removing the nodule candidates in Figure 5.1(d)(1). The nodule candidates are removed if less than 75% of their pixels appear on the combined α-image (see Figure 5.1(d)(2)). Figure 5.1(d)(1) is the first image in the continuous lung image set so it does not have a previous combined α-image to reference for either removing or keeping the nodule candidates. The nodule candidates in Figure 5.1(e)(5) are unable to be processed since the nodule candidates in Figure 5.1(d)(5) do not have a next combined α-image to reference. In addition, none of the nodule candidates in Figure 5.1(d)(5) belong to the nodule in the previous combined α-image (see Figure 5.1(d)(4)).

Figure 5.1(f)(1)-(2) images are able to be processed since they have the next third images (Figure 5.1(e)(3)-(4)) to reference. However, the Figure 5.1(f)(3)-(4) images cannot be processed by step (f) since the images in Figure 5.1(e)(3)-(4) do not have the next third combined α-image to reference. So the Figure 5.1(f)(3)-(4) images are the same as the images shown in Figure 5.1(e)(3)-(4). Figure 5.1(f)(5) is unable to be processed since the image in Figure 5.1(e)(5) cannot be processed.

5.2 α-images Selection and Combination

Lung nodules have higher intensity than either lung tissue or parts of lung veins on lung images. These nodules can be clearly viewed from lung images if they are of reasonably large size. Lung nodule pixels have similar intensity variation, which can be viewed in the α-images belonging to a certain α-range. Figure 5.2 shows the lung image from Figure 5.1(a)(2), which has the nodules indicated by squares.

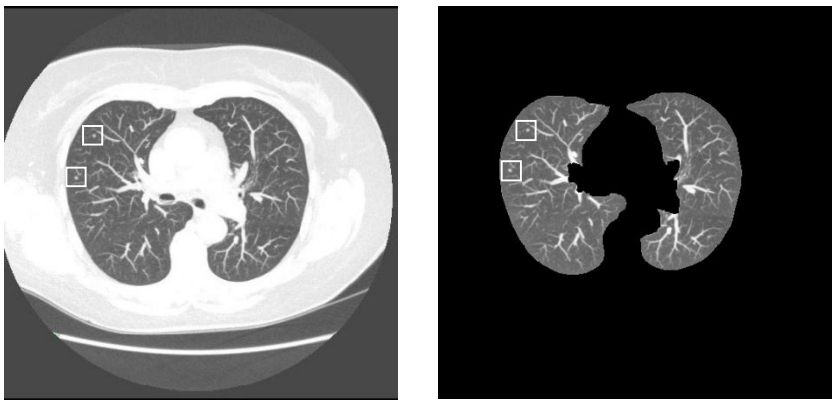

(a) (b)

Figure 5.2 Lung segmentation with nodules indicated by squares (a) Original lung image (b) Segmented lung regions

The nodules in Figure 5.2 are represented separately on different α-images from Figure 5.3(b)-(e). The nodule information starts appearing in the α-image in Figure 5.3(b) with an α-value 1.77, and it disappears on the α-image in Figure 5.3(f) with an α-value 1.94. So the nodule pixels α-range is from 1.77 to 1.94 for this specific lung image. Fifty different lung images were used for nodule α-range estimation. The nodule α-range was concluded from 1.34 to 1.96. This α-range is capable of extracting the nodule information from other lung images.

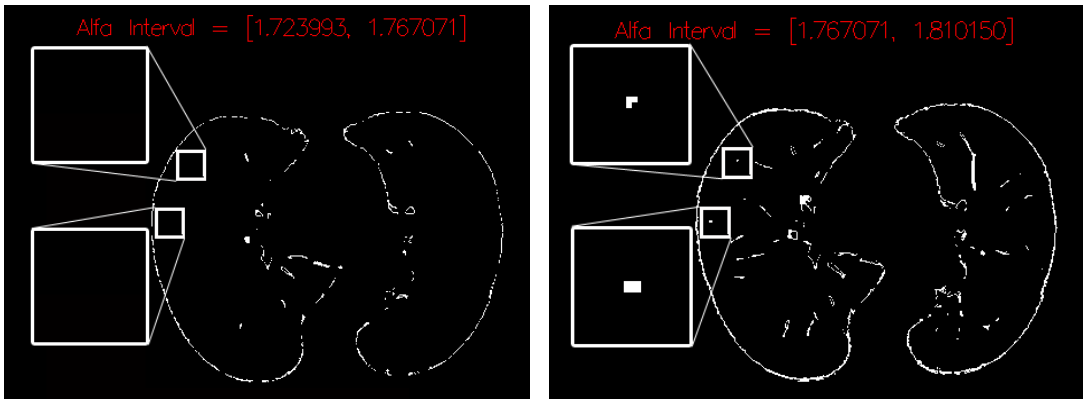

(a) (b)

Figure 5.3 α-images with nodule pixels indicated by squares (a) α-image without nodule information (b)-(e) α-images with nodule information (f) α-image without nodule information

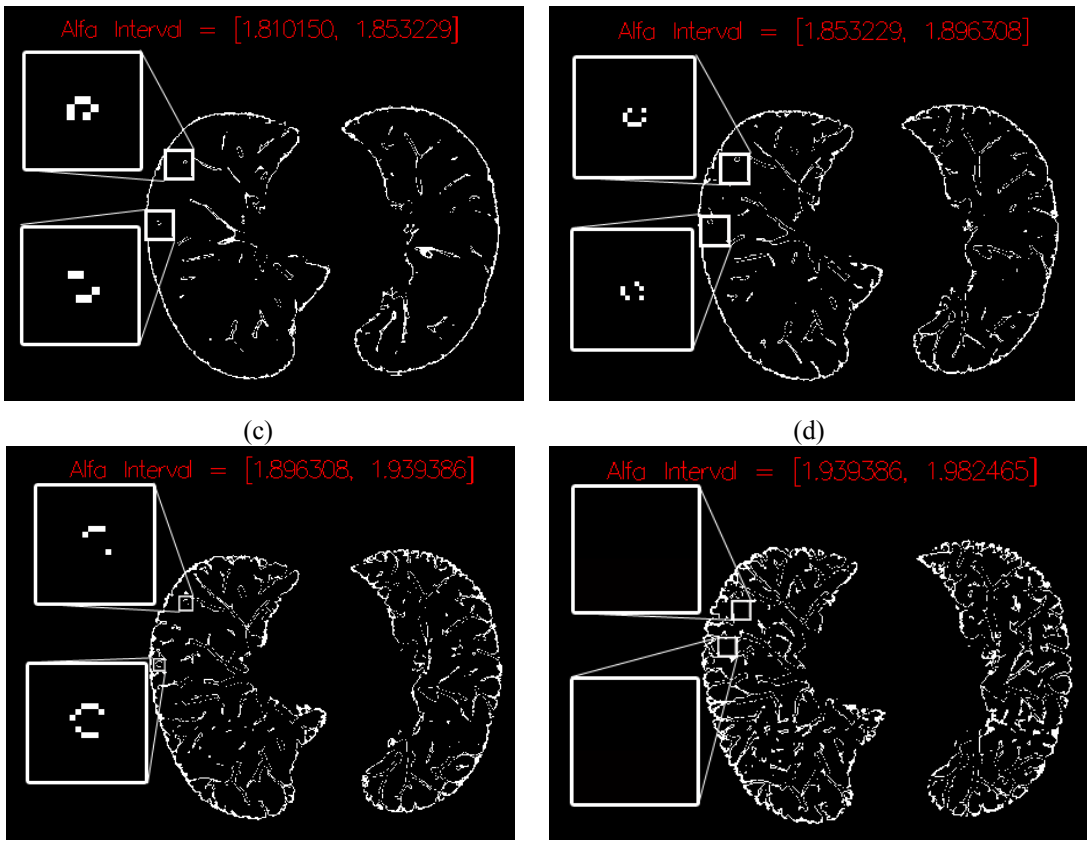

Figure 5.3 (contd.)

As seen in Figure 5.3, the nodule information is separately displayed on different α-images. Thus a complete lung nodule can be generated by combining those α-images. Figure 5.4 shows a combined α-image with nodules indicated by squares.

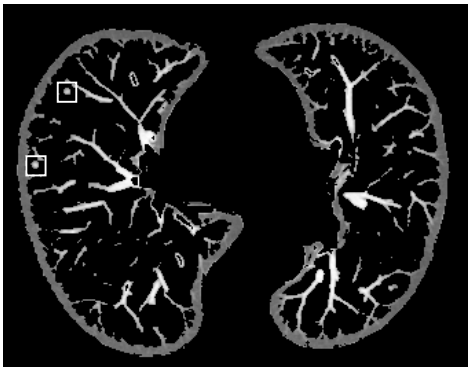

Figure 5.4 α-images combined from α-range 1.77 to 1.94

The combined α-image not only contains the nodules, but it also includes other non-nodule noise information. In this research, we are only interested in detecting and analysing nodules. So the non-nodule noise information needs to be eliminated from the combined α-image. Section 5.3 performs the rule based filtering process for eliminating false positive nodule candidates.

5.3 Rule Based Filtering to Eliminate false positives

Non-nodule noise information elimination is a preparation step for the nodule detection process presented in Section 5.4. Every nodule candidate on the combined α-image is labelled with a positive number. Nodule candidates are picked out by their label numbers for centroid based filtering, intensity based filtering, and frequency based filtering in consecutive HRCT slices.

5.3.1 Centroid Based Filtering

Based on the nodule characters, nodule candidates with centroids located outside are identified as non-nodules. Those non-nodule candidates are removed from the combined α-image. In Figure 5.5, the centroid of each nodule candidate is marked in black. Some typical nodule candidates are enlarged in order to show their centroid locations.

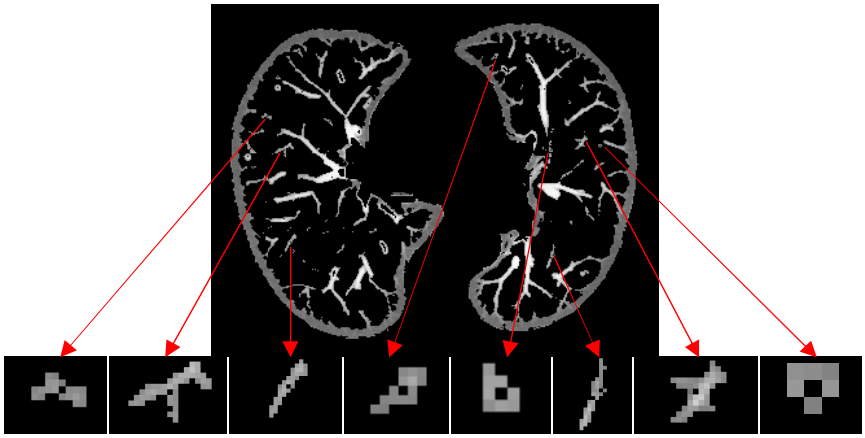

Figure 5.5 Nodule candidates with centroids marked

The circled nodule candidates and lung boundary shown in Figure 5.6(a) have their centroids located outside. Figure 5.6(b) presents the combined α-image that is processed by the centroid based filtering process. The nodule candidates with centroids located outside are removed in Figure 5.6(b). However, the majority of the nodule candidates are still left over and need to be removed by the filtering processes introduced in the following two sections.

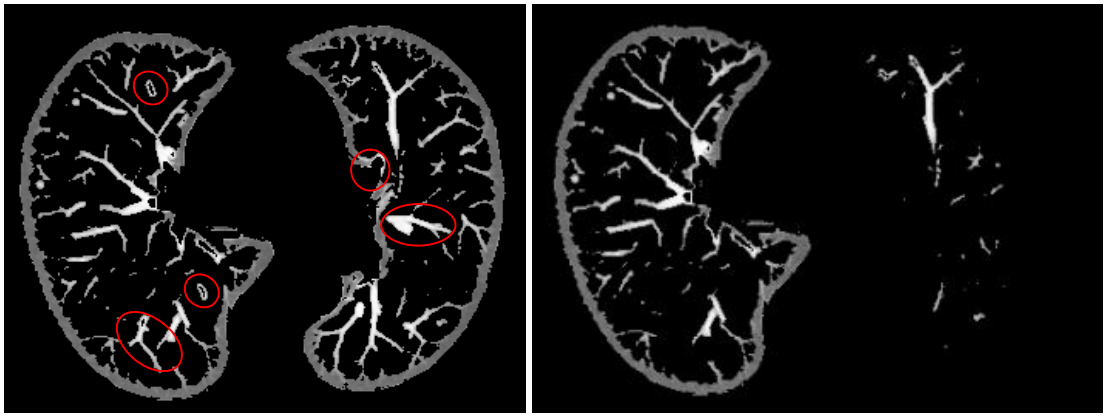

(a) (b)

Figure 5.6 Centroid based filtering (a) Nodule candidates with centroids located outside are circled (b) Centroid based filtering result

5.3.2 Intensity Based Filtering

Intensity based non-nodule noise information elimination removes nodule candidates with a lower intensity than nodules. The nodule candidates in the combined α-image can be categorised as nodules, veins and lung tissue. Nodules have a similar intensity as veins, and the intensity of lung tissue is lower than the intensity of nodules and veins, as shown in Figure 5.7.

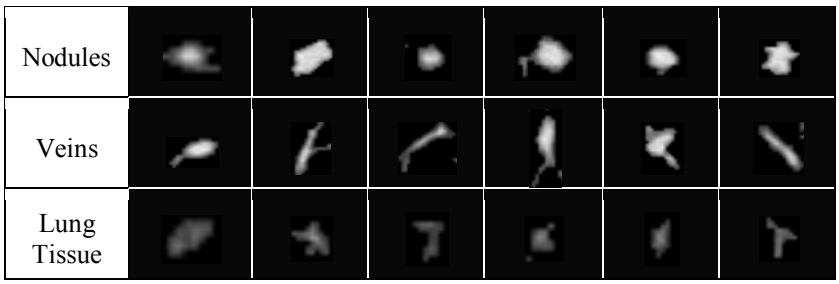

Figure 5.7 Intensity difference between nodules, veins and lung tissue

A scheme is designed to remove more nodule candidates from the combined α-image based on intensity criteria. In Figure 5.8, the pixel intensity mean of the nodules is larger than the pixel intensity mean of the lung tissue and part of the veins. Therefore, the lung tissue and part of the veins are recognised by the criterion that is less than the nodule mean threshold. Figure 5.8 also suggests that a threshold of T_m = 25000 would be adequate to distinguish nodules from veins and lung tissue.

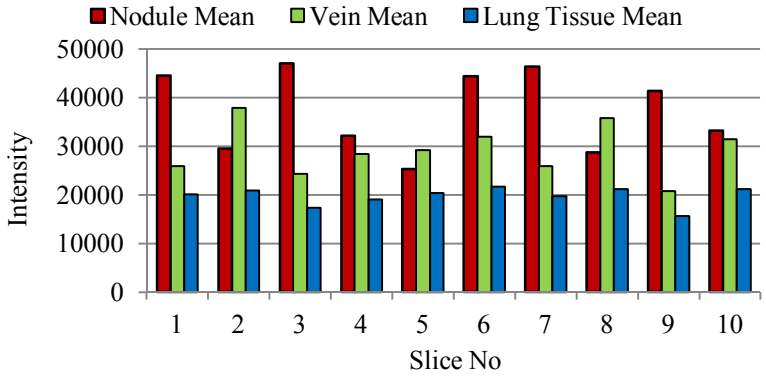

Figure 5.8 Intensity mean difference between nodules, veins and lung tissue

Intensity based filtering is performed on the image that is processed by centroid based filtering, as shown in Figure 5.9(a).

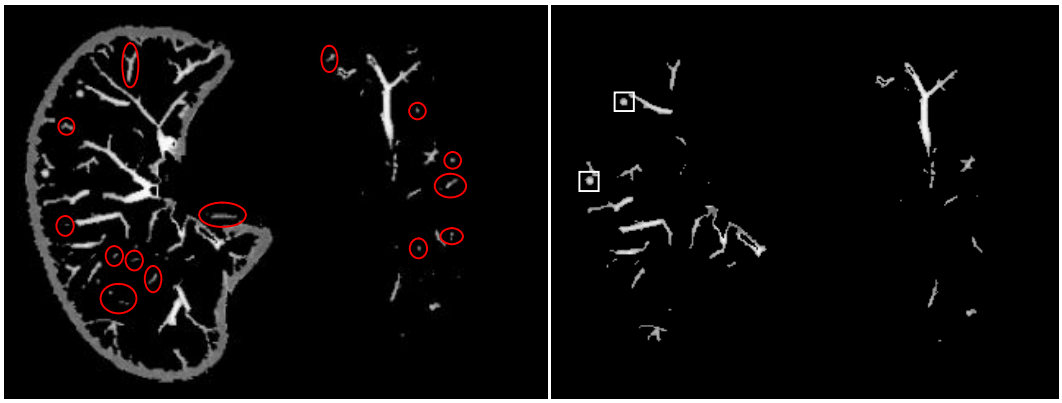

(a) (b)

Figure 5.9 Intensity based filtering (a) Nodule candidates with low intensity are circled (b) Intensity based filtering result

Circled nodule candidates in Figure 5.9(a) are removed due to their intensity values being lower than the intensity threshold. Figure 5.9(b) shows the result of removing the lung tissue and part of the veins by using the intensity based filtering process. In the result image, most of the nodule candidates have been removed and nodules and some other high intensity veins are left over.

The above two filtering processes are based on analysing an individual lung image. Now we consider removing more nodule candidates based on analysing consecutive HRCT slices.

5.3.3 Frequency Based Filtering

As mentioned in Section 2.1.3, lung nodules only appear on two or three consecutive HRCT slices. Nodule candidates need to be removed if they appear on less than two consecutive lung images or more than three consecutive lung images. A set of consecutive HRCT slices is presented in Figure 5.10(a)-(e). Figure 5.10(i)-(v) shows the pre-filtered combined α-images for the continuous lung image. Those combined α-images are processed by centroid based filtering process and intensity based filtering process.

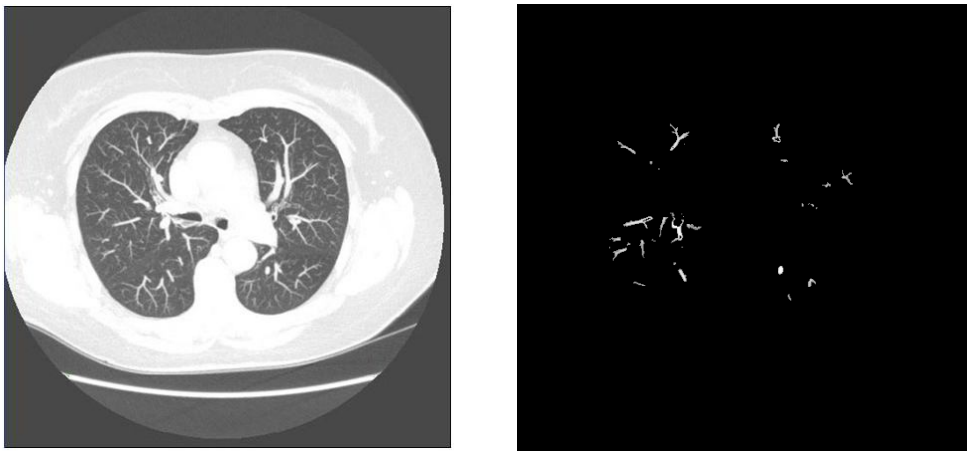

(a) (i)

Figure 5.10 (a)-(e) Consecutive HRCT slices (i)-(v) Combined α-images processed by centroid and intensity based filtering processes

(b)

(ii)

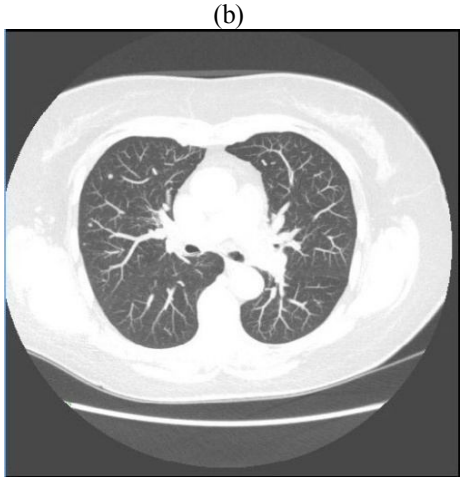

(c)

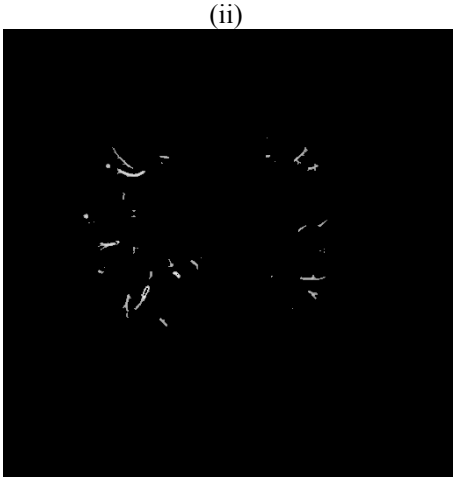

(iii)

(d)

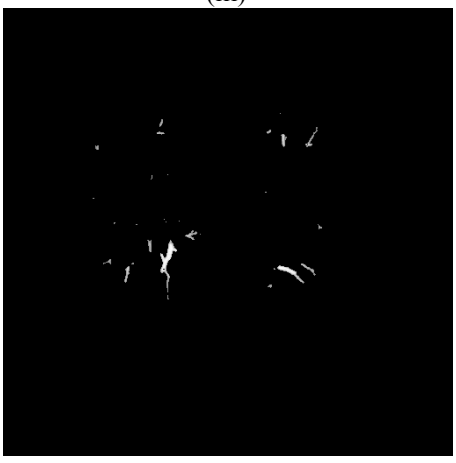

(iv)

Figure 5.10 (contd.)

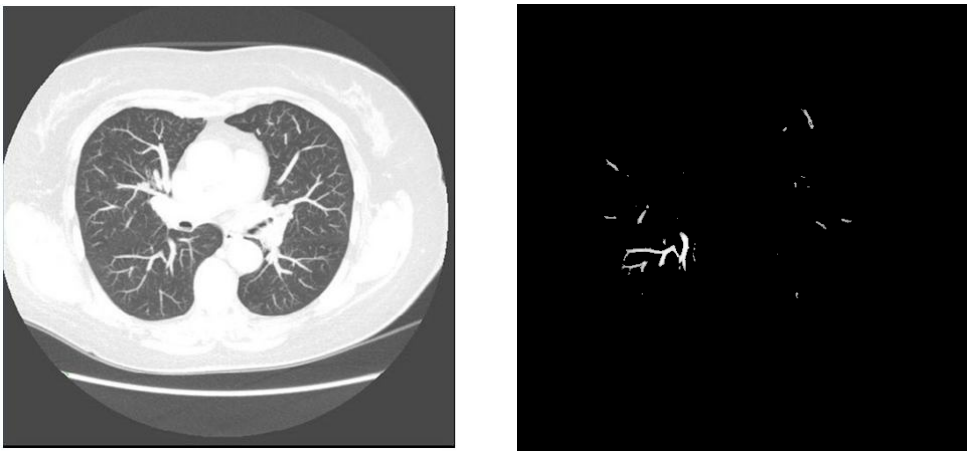

(e) (v)

Figure 5.10 (contd.)

The frequency based filtering process is performed in two steps: Step (1): Nodule candidates on the combined α-image are removed if less than 75% of their pixels appear on the next combined α-image. Twenty different nodules are used to determine the nodule pixel number variation on two continuous combined α-images. Some of the nodules have their size increased on the next continuous combined α-images. Figure 5.11 indicates the nodule pixel appearance on consecutive lung images.

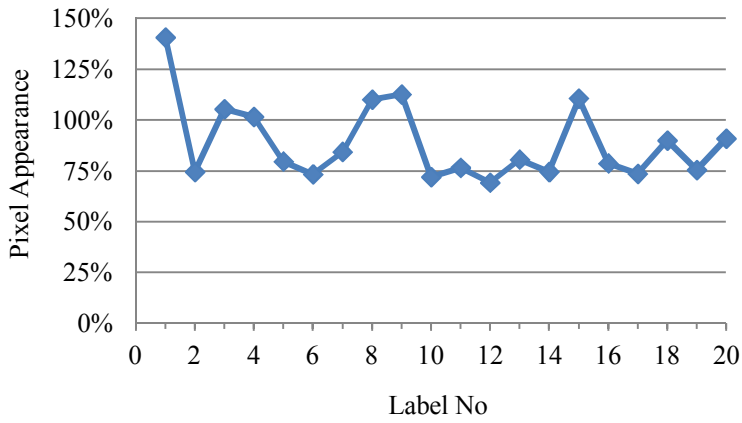

Figure 5.11 Nodule pixel appearance on consecutive HRCT slices

According to Figure 5.11, the size increased nodules have more than 100% of their pixels appearing on the next combined α-images. The rest of the nodules have around 75% of their pixels appearing on the next combined α-image. The 75%

pixel appearance criterion is adequate to remove most of the non-nodule noise information. In the meantime, nodule candidates need to be kept if they are identified as nodules in the previous lung image. Step (2): Nodule candidates need to be removed if any of their pixels appear on the next third combined α-image.

Frequency based filtering: Step 1

Figure 5.12-5.13 illustrates the step 1 process. Some sample nodule candidates indicated in Figure 5.12(a) need to be kept as 75% of their pixels exist on the next combined α-image given in Figure 5.12(b).

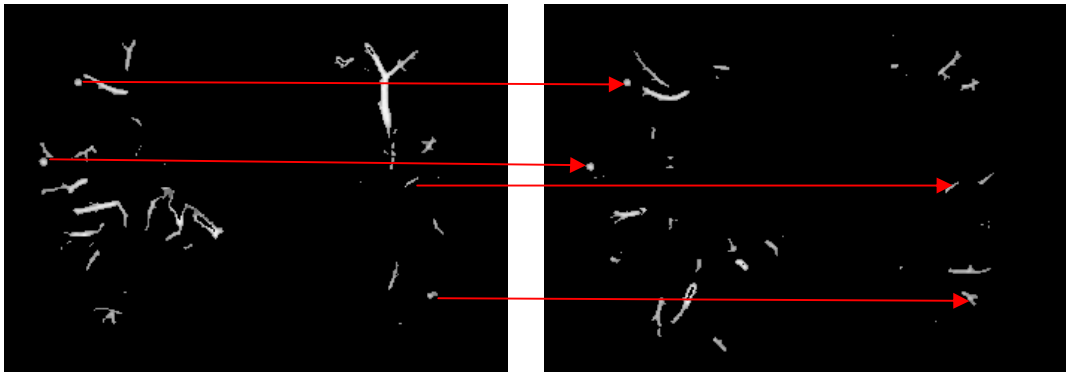

(a) (b)

Figure 5.12 Nodule candidates need to be kept (a) α-image shown in Figure 5.10(ii) (c) Combined α-image shown in Figure 5.10(iii)

In Figure 5.13(a), some sample nodule candidates are indicated for removal as less than 75% of their pixels exist on the next combined α-image shown in Figure 5.13(b).

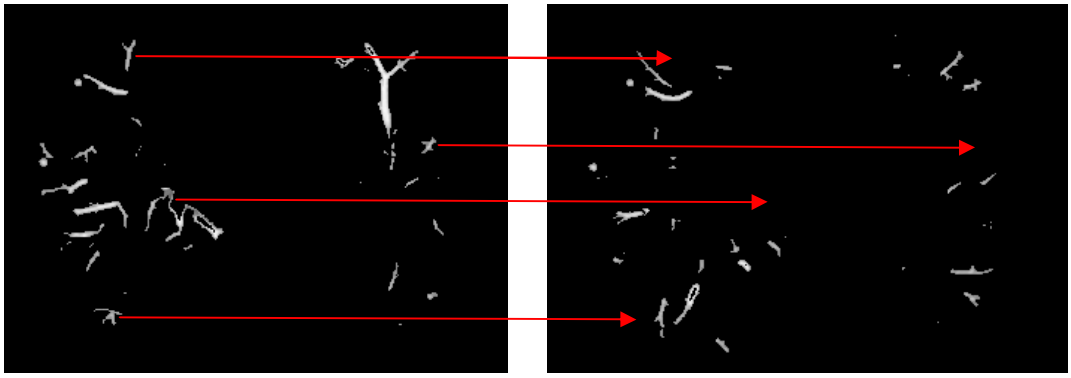

(a) (b)

Figure 5.13 Nodule candidates need to be removed (a) α-image shown in Figure 5.10(ii) (c) Combined α-image shown in Figure 5.10(iii)

The above 75% pixel appearance criterion eliminates a large number of non-nodule noise information. In the meantime, it is also necessary to check whether a nodule candidate is identified as a nodule in the previous lung image. If a nodule candidate is identified as a nodule in the previous lung image, then it needs to be kept.

Figure 5.14 presents three continuous combined α-images from Figure 5.10(ii)-(iv). According to the 75% pixel appearance criterion, nodule candidates need to be removed if less than 75% of their pixels exist on the next combined α-image. The nodule candidate numbered by 2 in Figure 5.14(b) does not satisfy the 75% pixel appearance criterion. However, it needs to be kept due to it being identified as a nodule in Figure 5.14(a). In the same case, the nodule candidate numbered by 1 in Figure 5.14(c) needs to be kept due to it being identified as a nodule in Figure 5.14(b). So if a nodule candidate has at least 75% of its pixels existing in the next combined α-image or it is identified as a nodule in the previous lung image, then this nodule candidate needs to be kept.

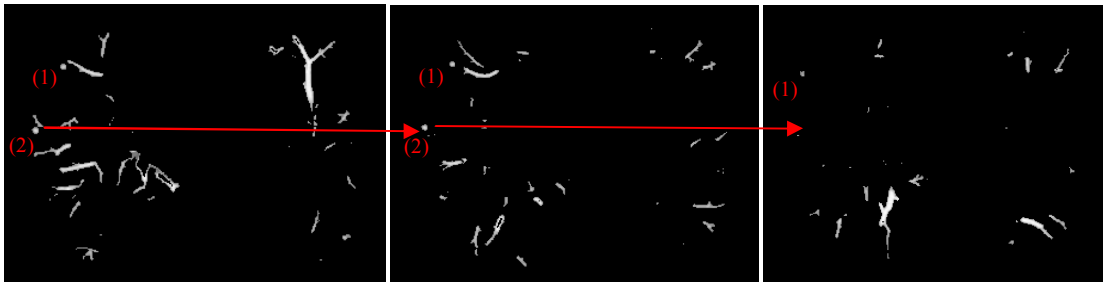

(a) (b) (c)

Figure 5.14 Pre-identified nodules need to be kept (a) Combined α-image shown in Figure 5.10(ii) (b) Combined α-image shown in Figure 5.10(iii) (c) Combined α-image shown in Figure 5.10(iv)

Figure 5.15 shows the result of Figure 5.10(ii) after the step 1 process. Most of the nodule candidates are removed, and the nodule candidates existing on the result image need to be further processed by the step 2 process.

Figure 5.15 Result of the step 1 process

Frequency based filtering: Step 2

The step 2 process removes the nodule candidates that have pixels that exist on its next third combined α-image. The output image of Figure 5.15 is originally from Figure 5.10(ii). So Figure 5.10(v) illustrates the next third combined α-image for the output image shown in Figure 5.15. Figure 5.10(v) is shown in Figure 5.16(b) and Figure 5.17(b).

In Figure 5.16(a), the indicated nodule candidates need to be kept since their pixels do not exist on the next third combined α-image (see Figure 5.16(b)).

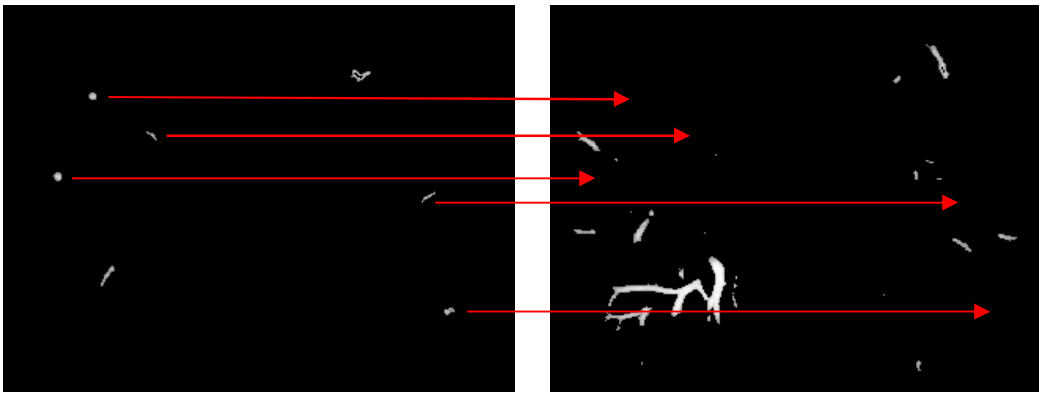

(a) (b)

Figure 5.16 Nodule candidates need to be kept (a) Result of the step 1 process (b) The next third combined α-image

The indicated nodule candidates in Figure 5.17(a) need to be removed since their pixels appear on the next third combined α-image (see Figure 5.17(b)).

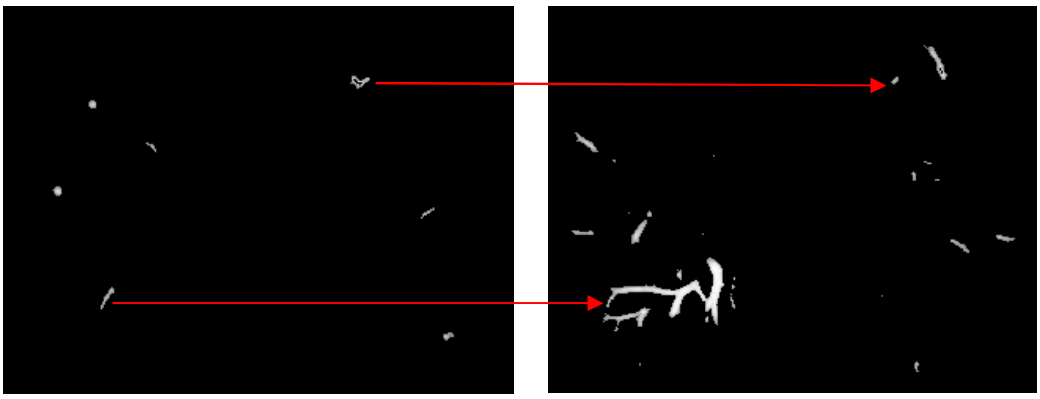

(a) (b)

Figure 5.17 Nodule candidates need to be removed (a) Result of the step 1 process (b) The next third combined α-image

Figure 5.18(b) shows the final result of the frequency based filtering, which is generated by removing the circled nodule candidates seen in Figure 5.18(a). The output image of Figure 5.18(a) is processed by centroid based filtering and intensity based filtering (see Figure 5.9(b)).

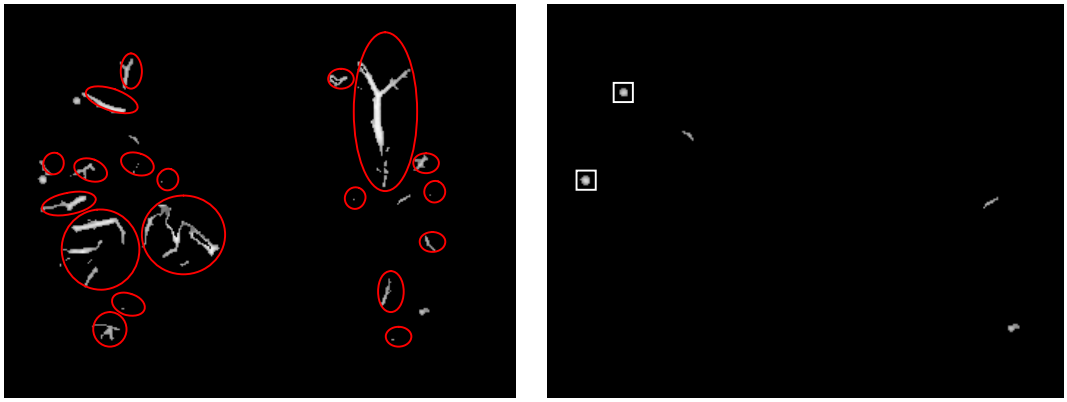

(a) (b)

Figure 5.18 Frequency based filtering (a) Nodule candidates need to be removed by the frequency based filtering are circled (b) Frequency based filtering result

According to the output image of Figure 5.18(b), the rule based filtering process successfully eliminated a large number of false positives, and nodules are kept after the process, as shown in Figure 5.18(b). Section 5.4 describes the development of the nodule detection technique.

5.4 Shape Feature Based Nodule Detection

The proposed nodule detection technique compares the shape features of filtered nodule candidates with nodule shape features. If the nodule candidates have similar shape features to nodules, then they are identified as nodules. The proposed nodule detection technique is capable of detecting spherical, star and quadrilateral shaped nodules. Figure 5.19 describes the structure of the nodule detection process.

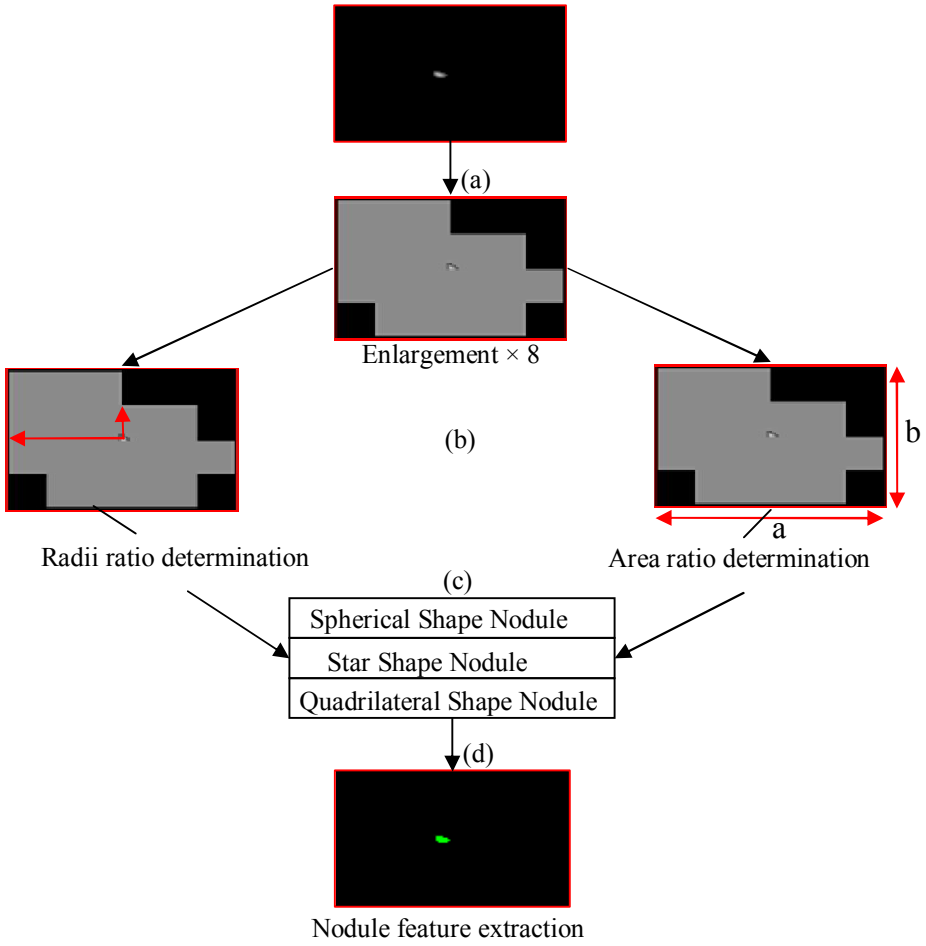

Figure 5.19 Shape feature based nodule detection

The whole process of the nodule detection technique can be presented by the following steps:

a) Each nodule candidate in Figure 5.18(b) is labelled and enlarged eight times for shape determination.

b) Nodule candidate shape features are determined using the nodule radii ratio metric and the nodule area ratio metric.

c) The shape feature of the three detecting nodules (nodules in spherical, star and quadrilateral shape) are extracted and analysed using the proposed metrics.

d) Nodules are identified by comparing whether nodule candidates have similar shape features to the three detecting nodules.

Section 5.4.1 presents a method of enlarging the nodule candidates for more accurate shape feature determination. The methodology of nodule shape determination is explained in Section 5.4.2. Nodule features are extracted in Section 5.4.3. Shape feature comparison is performed between the nodule candidates and the nodules in Section 5.4.4.

5.4.1 Nodule Candidates Enlargement

Small size lung nodules are normally hard to detect from lung images. Enlarging the filtered nodule candidates helps with determining shape features more accurately. Figure 5.20 illustrates the filtered nodule candidates from Figure 5.18(b). The labelled nodule candidates shown in Figure 5.20 are enlarged by adding pixels on the side of the original nodule candidates, as seen in Figure 5.21.

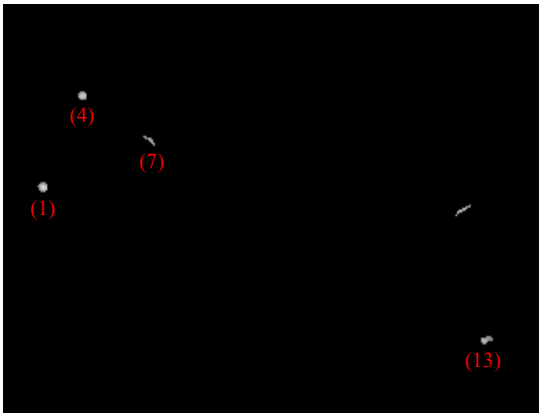

Figure 5.20 Filtered nodule candidates labelled by numbers

In Figure 5.21, the labelled nodule candidates from Figure 5.20 are enlarged from one to eight times. The more times the nodule candidate is enlarged, the more shape feature information is given.

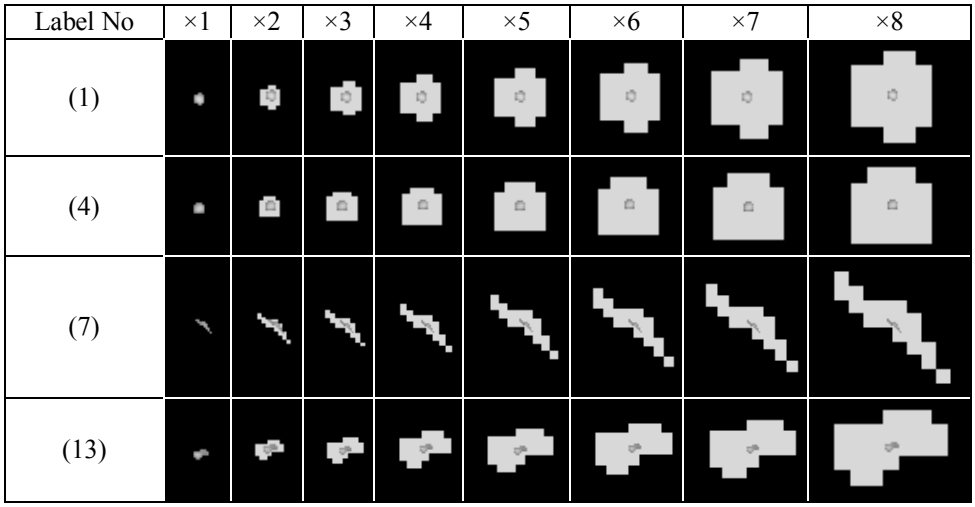

Figure 5.21 Labelled nodule candidates enlargement

Eight times enlargement is chosen, as enlarging more is too time consuming. The proposed nodule detection technique only enlarges the nodule candidates with a diameter lower than 20mm, which saves time for enlarging large size nodule candidates.

5.4.2 Nodule Shape Determination

Shape is an important feature that can be used to distinguish nodules from non-nodules. In this section, two metrics are proposed for nodule shape determination, and they are defined as nodule radii ratio and nodule area ratio.

Nodule radii ratio

The radii shape descriptor employs the centroid-radii model to represent shapes. This method is completely invariant to translation, rotation and scaling by normalising the radii lengths. Firstly, the shape's radii are computed from the centroid to the boundary of nodule candidates in various directions. And then, using the minimum and the maximum radii compose a vector $R = \{r_{min}, r_{max}\}$ to

represent the nodule shape. In order to explain the methodology of the proposed metrics more clearly, the nodules illustrated in Figure 5.22-5.24 are enlarged more than eight times. Figure 5.22 shows the minimum and the maximum radii of a spherical shape nodule.

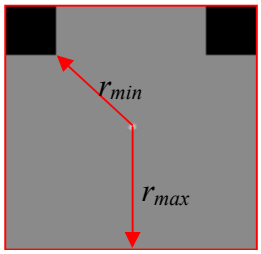

Figure 5.22 Minimum and maximum radii

The nodule radii ratio (R_r) is computed by dividing the minimum radius (r_{min}) by the maximum radius (r_{max}), as defined in Equation 5.1.

$$R_r = \frac{r_{min}}{r_{max}} \tag{5.1}$$

Nodules with different shapes have different nodule radii ratios. Figure 5.23(a)-(c) shows the nodules in spherical, star and quadrilateral shape which are enlarged in Figure 5.23(1)-(3). Each enlarged nodule has its minimum and maximum radii indicated.

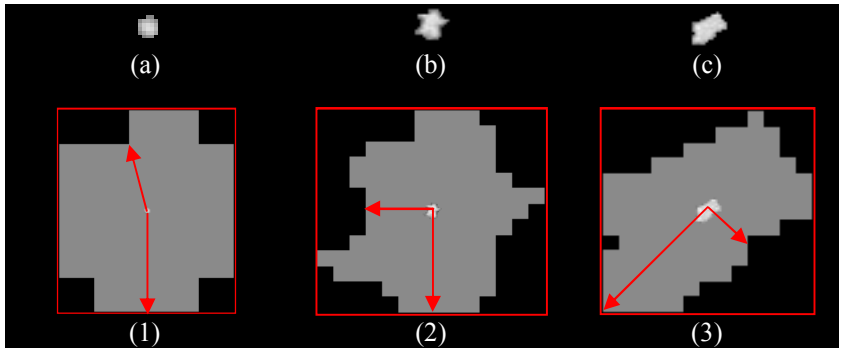

Figure 5.23 Nodule radii for the detecting nodules (a)-(c) Original size nodules (1)-(3) Nodules with minimum and maximum radii indicated

From Figure 5.23, the nodules of spherical and star shape have minimum and maximum radii of similar length. The quadrilateral shape nodule has a large difference between its minimum and maximum radii. The nodule radii ratio

difference can be used to roughly differentiate the nodule shapes presented in Figure 5.23. However, nodule shapes cannot be accurately determined by only implementing the nodule radii ratio metric. The nodule area ratio metric is also needed for more accurate shape determination.

Nodule area ratio

The nodule area ratio is defined as the ratio between the actual nodule area and the area of the axis-aligned bounding box. Figure 5.24 shows the enlarged nodules of spherical, star and quadrilateral shape. In Figure 5.24, the actual nodule area is represented by a grey area. The actual nodule area size A is determined by counting the number of pixels existing in the grey area. The nodule area in x direction is represented by a, and the nodule area in y direction is represented by b, as indicated in Figure 5.24. The nodule size B in x and y directions can be generated by multiplying a by b.

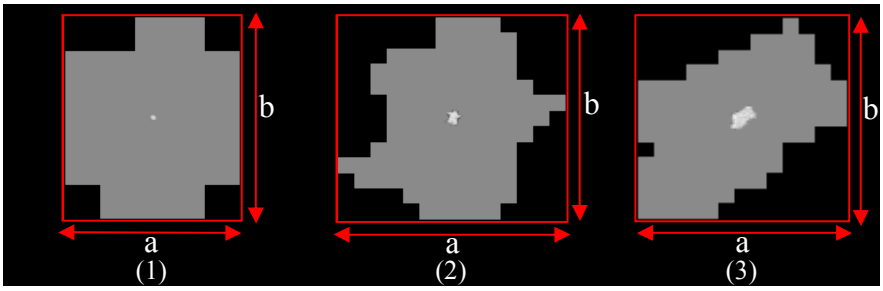

Figure 5.24 Nodule areas for detecting nodules (1)-(3) Nodules with size in x and y directions indicated

The nodule area ratio (R_a) between the actual nodule area (A) with the bounding box size in x and y directions (B) is defined in Equation 5.2.

$$R_a = \frac{A}{B} \tag{5.2}$$

The nodule area ratio shows how much of the nodule area in x and y directions is occupied by the actual nodule. As seen in Figure 5.24, the spherical shape nodule has the highest nodule area ratio because the actual nodule area size is similar to the nodule area size in x and y directions. Both the star and quadrilateral shape nodules have similar nodule area ratios.

The nodule radii ratio metric is able to distinguish the quadrilateral shape nodules, and the nodule area ratio metric is capable of differentiating the spherical nodules. So those nodule shapes can be accurately determined by implementing both of the metrics.

5.4.3 Nodule Shape Feature Extraction

Nodule shape feature extraction is a preparation step for nodule identification. In this research, nodule shape features are defined and represented by the radii ratio and the area ratio. Seventy-five nodules are collected and categorised into three shape groups for nodule radii ratio and nodule area ratio estimation. Those nodules are grouped into spherical, star and quadrilateral shape. The number of nodules for each group is 31, 19 and 25. All the nodules in those groups are enlarged eight times before their shape feature determination.

The ranges of the nodule radii ratio for different nodule shapes are given in Table 5.1.

Table 5.1 Nodule radii ratio ranges for different nodule shapes

Nodule Shapes	Min Radii Ratio [%]	Max Radii Ratio [%]
Spherical Shape	80.30	90.71
Star Shape	60.35	83.21
Quadrilateral Shape	33.51	50.25

In Table 5.1, the radii ratio range of the quadrilateral shape nodule is smaller than the radii ratio range of the spherical and the star shape nodule. Quadrilateral shape nodules can be easily distinguished by comparing their radii ratios with the radii ratios for the other two shapes. The ranges of nodule area ratios for different nodule shapes are concluded in Table 5.2.

Table 5.2 Nodule area ratio ranges for different nodule shapes

Nodule Shapes	Min Area Ratio [%]	Max Area Ratio [%]
Spherical Shape	75.12	98.18
Star Shape	58.16	71.38
Quadrilateral Shape	25.37	63.86

Table 5.2 shows spherical shape nodules have the highest area radii ratio compared with the other two nodule shapes. So the spherical shape nodules can be easily differentiated from the other two shapes.

5.4.4 Nodule Identification

Nodule identification is performed by comparing the nodule candidate shape features with the shape features of the three different nodules, as shown in Table 5.1-5.2. Figure 5.25 shows the difference of the radii ratios and the area ratios of the three detecting nodules.

In Figure 5.25, the nodules of different shapes have different levels of ratio. For example, the spherical shape nodules have a higher radii ratio and area ratio than the star and quadrilateral shape nodules. The star shape nodules have a higher radii ratio and area ratio than the quadrilateral shape nodules.

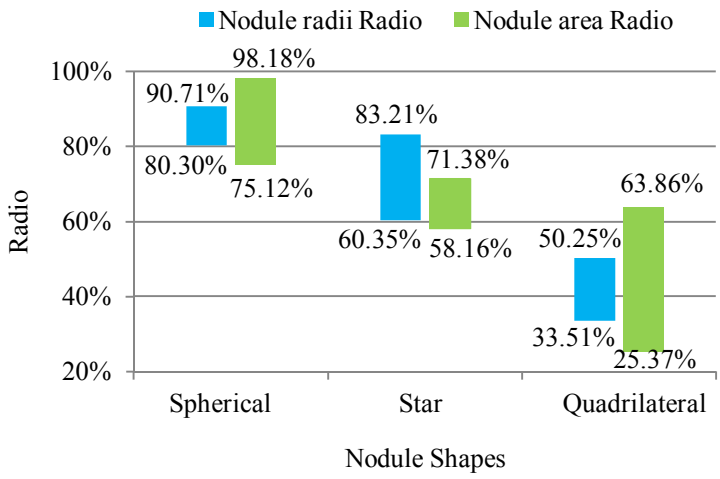

Figure 5.25 Ratio difference between the three nodule shapes

The ratio difference between those nodule shapes is quite clear and easy to identify. For example, if a nodule candidate is of spherical shape, then its radii ratio and area ratio must be in the range of 80.30% to 90.71% and 75.21% to 98.18%. So the nodule identification process is simply checking which ratio range the nodule candidate belongs to.

Figure 5.26(a) shows the nodule candidates labelled 1 and 4 are defined as spherical shape nodules in Figure 5.26(b). The pixels of the nodule candidates that identified as nodules are highlighted in green, as shown in Figure 5.26(b).

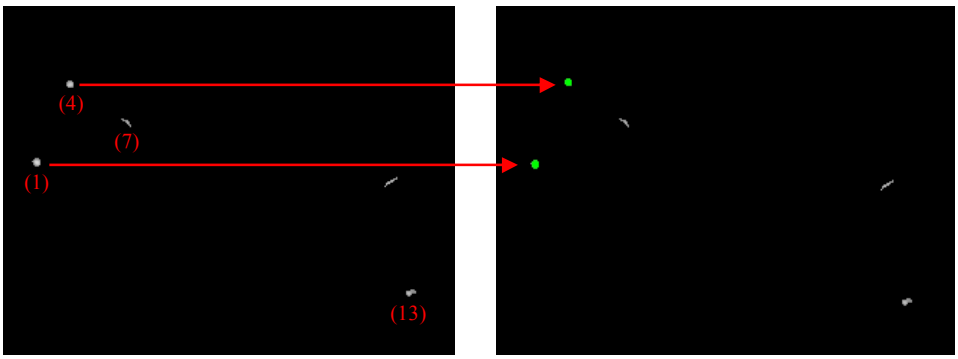

(a) (b)

Figure 5.26 Nodule detection (a) Filtered nodule candidates. (b) Detected nodules are highlighted

5.5 Summary

The proposed lung nodule detection technique extracts nodule candidates by combining the α-images containing nodule information, and rule based filtering is performed to reduce false positives. Nodule radii ratio and nodule area ratio are the two metrics that are used to determine the shape features of the filtered nodule candidates. Determined shape features of the nodule candidates are compared with the nodule shape features for nodule identification.

The advantages and the limitations of the lung nodule detection technique are listed as follows:

Advantages of the proposed technique

- The method is fully automatic, and is able to process different numbers of continuous images for nodule detection.
- The rule based filtering process can effectively remove the majority of the non-nodule noise information.
- The shape feature based nodule detection process can accurately identify the nodules in spherical, star and quadrilateral shape.

Limitations of the proposed technique

- The method is only capable of detecting nodules in spherical, star and quadrilateral shape.

Chapter 6

Results and Analysis: Lung Segmentation

This chapter presents and analyses the results of the lung segmentation technique. The lung segmentation results are automatically generated from the lung segmentation technique described in Chapter 4.

The implementation of the technique is tested with various types of lung images to determine its effectiveness. The accuracy of the lung segmentation is quantified by determining the performance metrics, such as sensitivity, specificity, accuracy, precision and F-measure. A detailed evaluation and comparative analysis are performed on the results.

Section 6.1 lists some typical lung segmentation results, and Section 6.2 gives an evaluation and comparative analysis of the results.

6.1 Experimental Results

This section lists the resulting images of the lung segmentation technique described in this work. Figure 6.1(i)-(xii) indicates the results after lung segmentation for a set containing distinctly different images and features. In all the cases, the lung regions have been successfully segmented. In order to show the robustness and accuracy of the proposed method, the lung regions in the test images (see Figure 6.1 (a)-(l)) have varying shape, size and location. As seen from the results, airway regions of different sizes and shapes have also been detected and removed by the proposed method. Figure 6.1(1)-(12) shows that precise lung boundaries are detected by using the proposed lung segmentation technique.

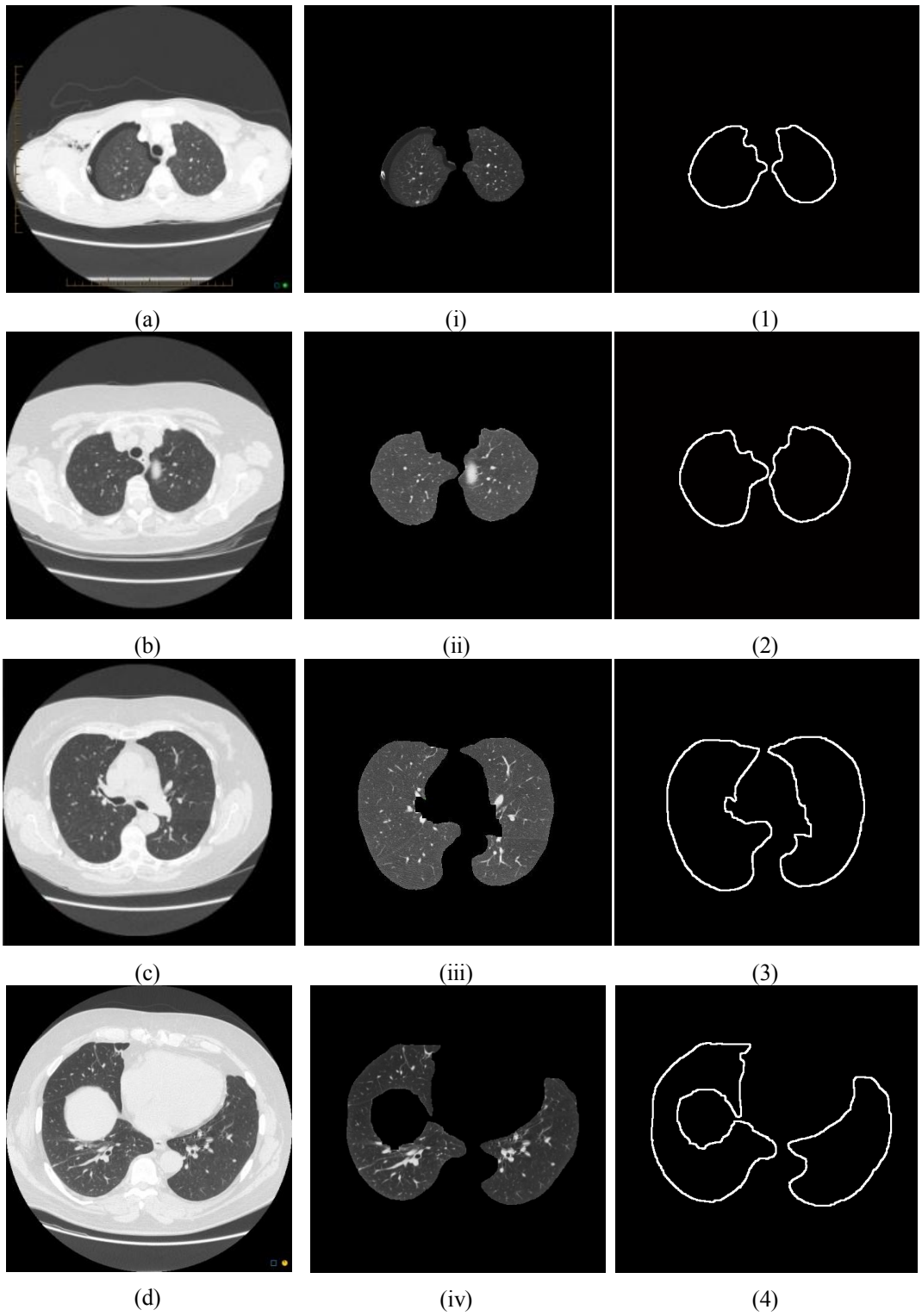

Figure 6.1 Lung segmentation results

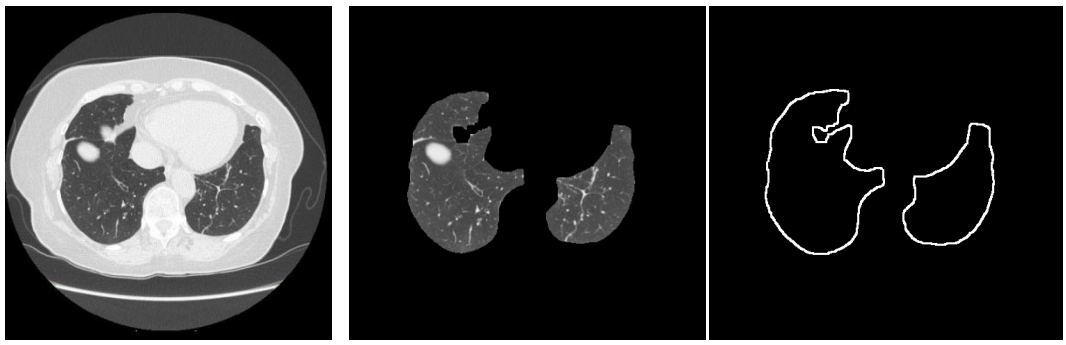

(e) (v) (5)

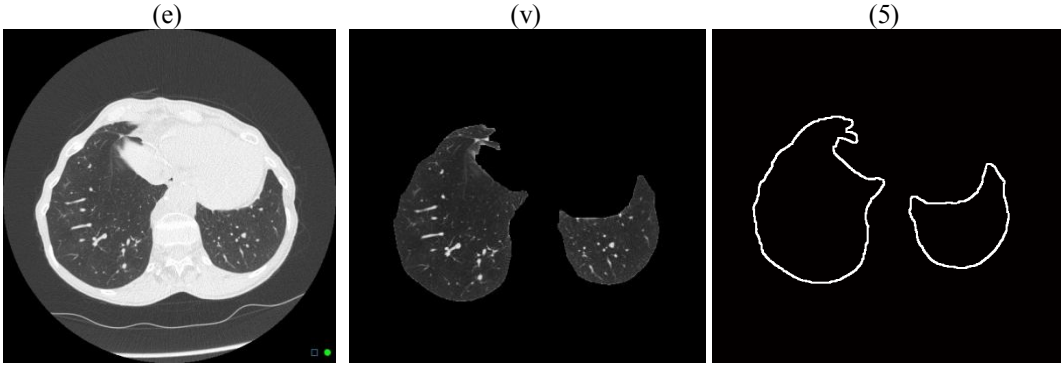

(f) (vi) (6)

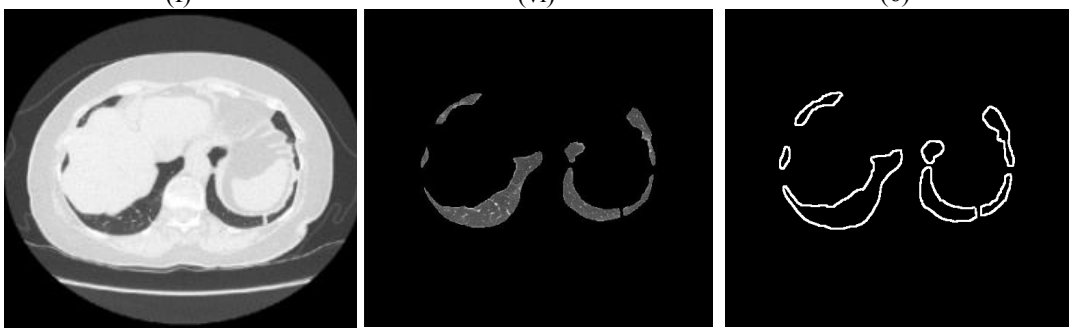

(g) (vii) (7)

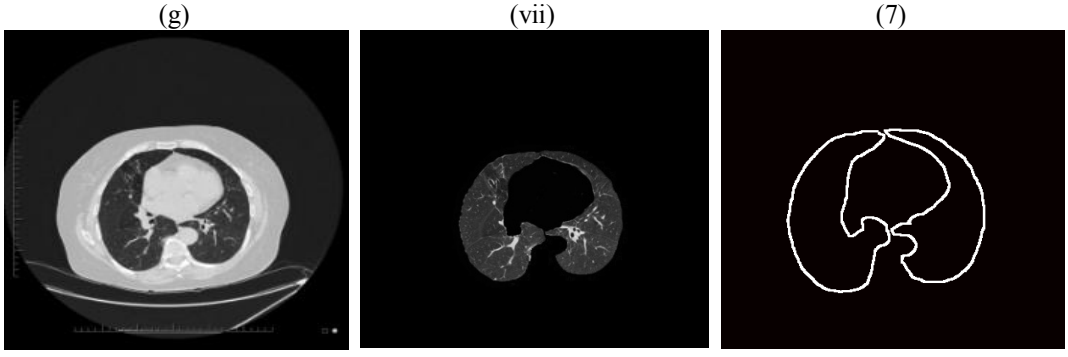

(h) (viii) (8)

Figure 6.1 (contd.)

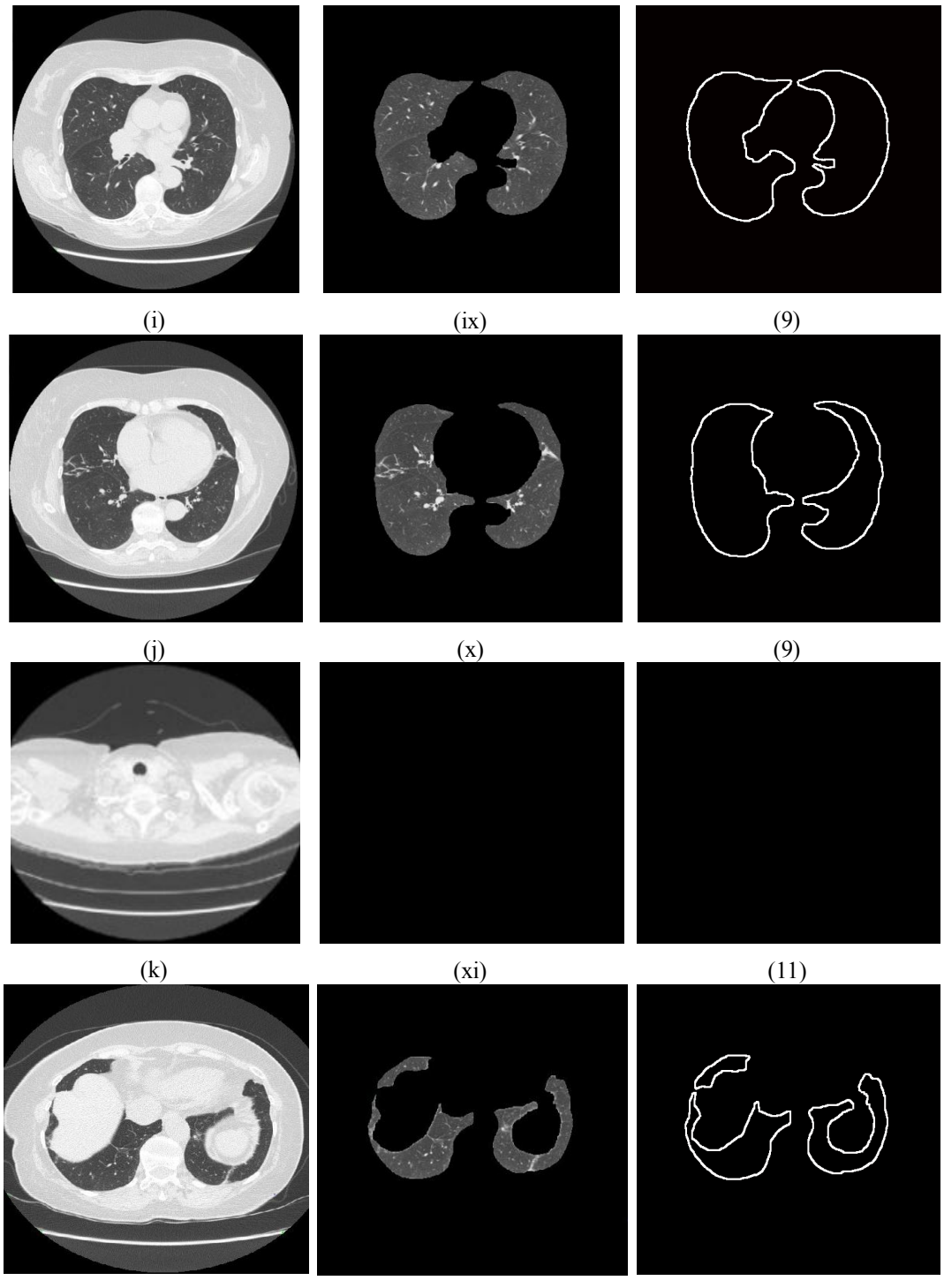

Figure 6.1 (contd.)

In Figure 6.1(a), (c), (e), (j) and (l), the intensity values of the pixels on the bronchi and the lung boundary are precisely restored by the method represented in

Section 4.5. The proposed lung segmentation method is able to segment lung regions of small size, as shown in Figure 6.1(g). All small size lung regions are retained after the lung segmentation. The trachea regions seen in Figure 6.1(j) and (k) are effectively eliminated by using the method presented in Section 4.4. The segmentation result shown in Figure 6.1(xi) is a black image due to the fact that lung regions do not exist on the lung image (see Figure 6.1(k)).

6.2 Evaluation and Comparative Analysis

To evaluate and show the effectiveness of the lung segmentation technique, result discussion and comparative analysis are given in this section. The factors influencing lung segmentation are discussed in Sections 6.2.1. Section 6.2.2 presents the comparison between our lung segmentation results and those presented in other people's work. The lung boundary detected by the proposed lung segmentation technique is compared with the lung boundary identified by edge detectors in Section 6.2.3.

6.2.1 Result Discussion

We considered the factors that affect the accuracy of lung segmentation. Those factors are listed as follows:

STR Small trachea region (see Figure 6.1(j)).

ITS Irregular trachea shape (see Figure 6.1(c)).

SLR Small Lung regions (see Figure 6.1(g)).

ILS Irregular lung shape (see Figure 6.1(d) and (e)).

CLJ Close lung junctions (see Figure 6.1(h)).

CLTD Close lung and trachea distance (see Figure 6.1(i)).

Let *a* be the number of HRCT images with one specific factor, and *b* be the number of HRCT images that are segmented accurately. Then *b/a* represents the

segmentation accuracy ratio. In our case, we set the value of *a* to 30 for each factor listed above. Figure 6.2 shows the comparison of segmentation accuracy ratios.

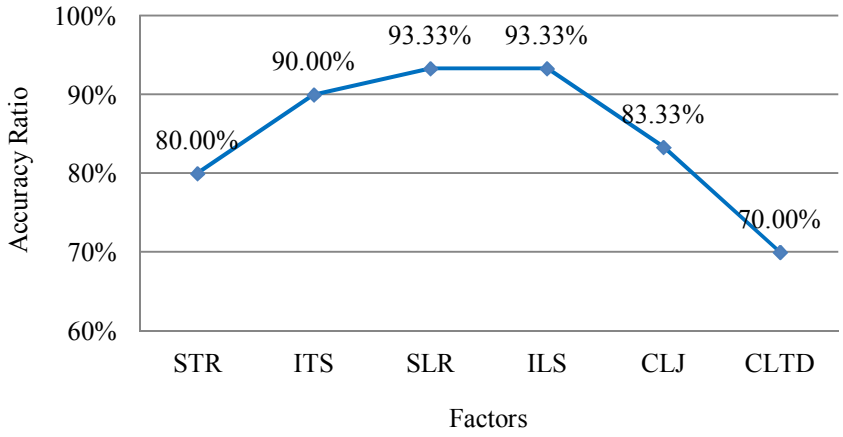

Figure 6.2 Comparison of segmentation accuracy ratios

From Figure 6.2, the images with irregular trachea shape (ITS), small lung regions (SLR), irregular lung shape (ILS) and close lung junctions (CLJ) are segmented well with an accuracy rate over 80%. For images with small trachea region (STR) and close lung and trachea distance (CLTD), the accuracy ratio is found to be lower than 80%.

From the results, it is concluded that the airway region and the lung regions can be effectively separated using pixel intensity mean and deviation values. The proposed method is still sensitive with the lung image with small trachea region and close lung and trachea distance. However, the variation of the lung shape and size will not reflect the segmentation result very much.

6.2.2 Comparison with Manual Analysis

Segmentation accuracy was assessed by comparing our lung segmentation results with manually traced segmentation results. As creating manual segmentation is labour intensive, evaluation was performed on three lung images. Each lung image has lung regions that vary in shape, size and location. Lung boundary is manually traced for every slice of the images.

For each of the performance metrics, we consider:

- True Positive (TP): The number of pixels that are correctly classified as lung.
- False Positive (FP): The number of pixels that are not correctly classified as lung.
- True Negative (TN): The number of pixels that are correctly classified as background.
- False Negativity (FN): The number of pixels that are not correctly classified as background.

Performance is measured in terms of sensitivity, specificity, accuracy, precision and F-measure, regarding the number of pixels in the evaluation slices that were correctly or incorrectly classified as being either lung or background. Values of those performance metrics vary from 0 to 1. Those metrics are defined as follows:

$$Sensitivity = \frac{TP}{TP + FN} \tag{6.1}$$

$$Specificity = \frac{TN}{TN + FP} \tag{6.2}$$

$$Accuracy = \frac{TP}{TP + TN} \tag{6.3}$$

$$Precision = \frac{TP}{TP + FP} \tag{6.4}$$

$$F(\beta) = \frac{(1 + \beta^2)PS}{\beta^2 P + S} \tag{6.5}$$

In Equation 6.5, β is used to control the weight that is assigned to the precision and sensitivity. P and S stand for the precision and sensitivity performance metrics. We assumed equal importance of sensitivity and precision by setting the β value as 1.

Figure 6.3-6.5 demonstrates the results of the proposed lung segmentation technique and manual lung segmentation. Each figure gives an image from

different lung portions in order to view the performance variation of the images with different shapes. The image (b) in each figure shows the result of the proposed lung segmentation technique. The image (c) indicates the outline of the lung mask of the reference scan, which is used to match the evaluation scan, as generated by manual lung segmentation. Table 6.1-6.3 below the figures give the performance metric measurement of each image shown in Figure 6.3-6.5.

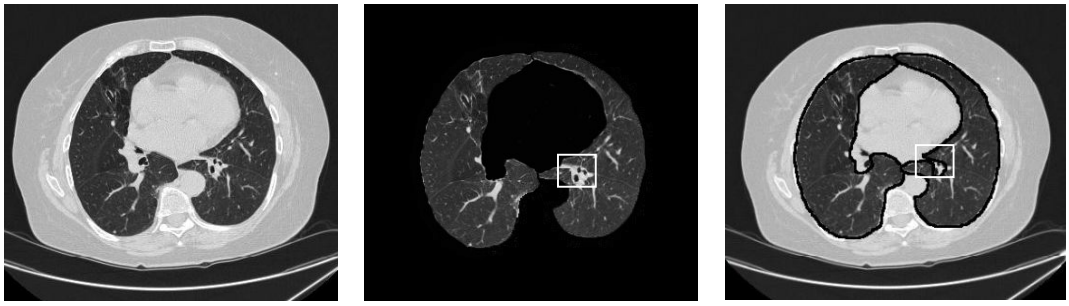

(a) (b) (c)

Figure 6.3 Image from upper lung portion (a) Original lung image (b) Lung segmentation result with restored bronchi region indicated (c) Manual lung segmentation result with restored bronchi region indicated

In Figure 6.3(b), the proposed method restores a large number of pixels (indicated by a square) of the lost right lung bronchi region shown in Figure 4.12. However, in the manual segmentation result (see Figure 6.3(c)), the square indicated bronchi region does not actually belong to the lung regions. In this case, the number of pixels that are not correctly classified as background is increased (*FN*). Both the sensitivity and the accuracy performance metrics of the lung segmentation are decreased. For the lung image, segmentation results were as follows:

Table 6.1 Performance metric measurement for upper lung portion images.

Performance Metrics	Sensitivity	Specificity	Accuracy	Precision	*F*(1)
Value	0.8995	0.9706	0.9461	0.9774	0.9368

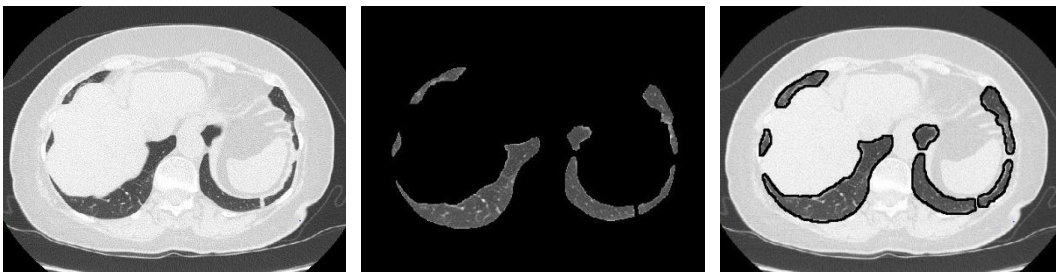

(a) (b) (c)

Figure 6.4 Image from lower lung portion (a) Original lung image (b) Lung segmentation result (c) Manual lung segmentation result

According to the segmentation result shown in Figure 6.4(b), the proposed method performs well on segmenting small size and separated lung regions. Each small lung region is accurately segmented without any background information included or lung region information lost. For the lung image, segmentation results were as follows:

Table 6.2 Performance metric measurement for lower lung portion images.

Performance Metrics	Sensitivity	Specificity	Accuracy	Precision	*F*(1)
Value	0.9769	0.9876	0.9977	0.9987	0.9877

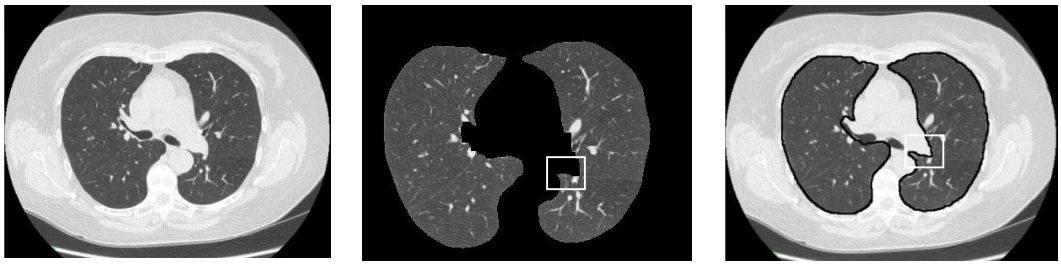

(a) (b) (c)

Figure 6.5 Image from middle lung portion (a) Original lung image (b) Lung segmentation result with lost lung regions indicated (c) Manual lung segmentation result with lost lung regions indicated

Compared to the manual segmentation result of Figure 6.5(c), the proposed method segmentation result in Figure 6.5(b) shows part of the lung regions is lost (indicated by a square). The lost lung region pixels cause the value of false positive to increase and the precision to decrease. The specificity and accuracy of the proposed lung segmentation method also decrease. For the lung image, segmentation results were as follows:

Table 6.3 Performance metric measurement for middle lung portion images.

Performance Metrics	Sensitivity	Specificity	Accuracy	Precision	$F(1)$
Value	0.9381	0.9285	0.9391	0.9004	0.9188

Some other people have also used these metrics for evaluation. Sluimer et al. [22] used sensitivity, specificity and accuracy as performance metrics. Comparison with Sluimer et al. is shown in Table 6.4.

Table 6.4 Comparison with Sluimer et al.'s method.

Performance Metric	Sluimer et al.	Proposed Method
Sensitivity	0.9200	(0.8995+0.9769+0.9381)/3 = 0.9382
Specificity	0.9600	(0.9706+0.9876+0.9285)/3 = 0.9622
Accuracy	0.9500	(0.9461+0.9977+0.9391)/3 = 0.9610

As Table 6.4 indicates, the proposed method outperformed Sluimer et al.'s method. The sensitivity, specificity and accuracy of the proposed method are higher than Sluimer et al.'s method. Vinhais et al. [23] used sensitivity, precision and F-measure as performance metrics. Comparison with Vinhais et al. is shown in Table 6.5.

Table 6.5 Comparison with Vinhais et al.'s method

Performance Metric	Vinhais et al.	Proposed Method
Sensitivity	0.9908	(0.8995+0.9769+0.9381)/3 = 0.9382
Precision	0.9862	(0.9774+0.9987+0.9004)/3 = 0.9588
F-measure	0.9885	(0.9368+0.9877+0.9188)/3 = 0.9478

According to Table 6.5, the proposed method is not as effective as Vinhais et al.'s method. Vinhais et al.'s method is able to accurately identify the bronchi region, background region and lung regions. So Vinhais et al.'s method has high sensitivity (0.99) and precision (0.99). The proposed method is not fully capable of identifying the bronchi region and lung regions, as shown in Figure 6.3. The background region and lung regions are also hard to distinguish by using the proposed method, as seen in Figure 6.5. So the proposed method has lower sensitivity and precision than Vinhais et al.'s method. The proposed method also has a lower F-measure (0.95) due to the sensitivity and the precision being low.

6.2.3 Comparison with Edge Detection

The lung boundary detected by the proposed method is compared with the lung boundary identified by edge detection methods. The Sobel operator [59] and the Canny edge detector [60] are used for lung edge detection. As mentioned in Section 3.3.1 the Holder exponent is able to detect the lung boundary.

Figure 6.6 shows an original lung image, which is used for lung boundary detection. The lung boundary detected by our proposed method is presented in Figure 6.7(a). Figure 6.7(b)-(c) indicates the lung boundaries detected by the Sobel operator and the Canny edge detector. Figure 6.7(d) gives the lung boundary detected by the Holder exponent.

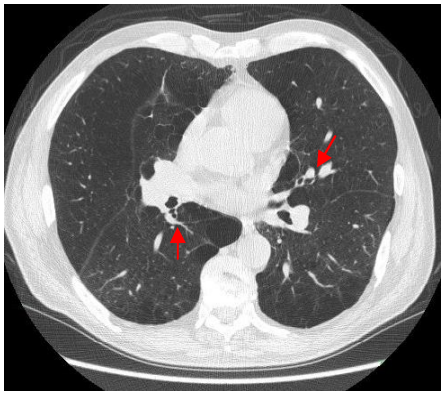

Figure 6.6 Original lung image with high intensity vein indicated

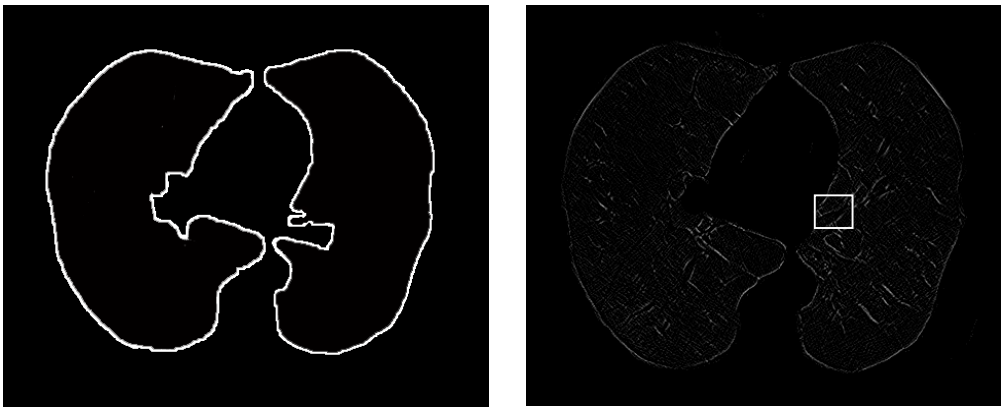

(a) (b)

Figure 6.7 Lung boundaries detected by: (a) Proposed method (b) Sobel operator with missed boundary indicated (c) Canny edge detector with missed boundary indicated (d) Holder exponent with missed boundary indicated

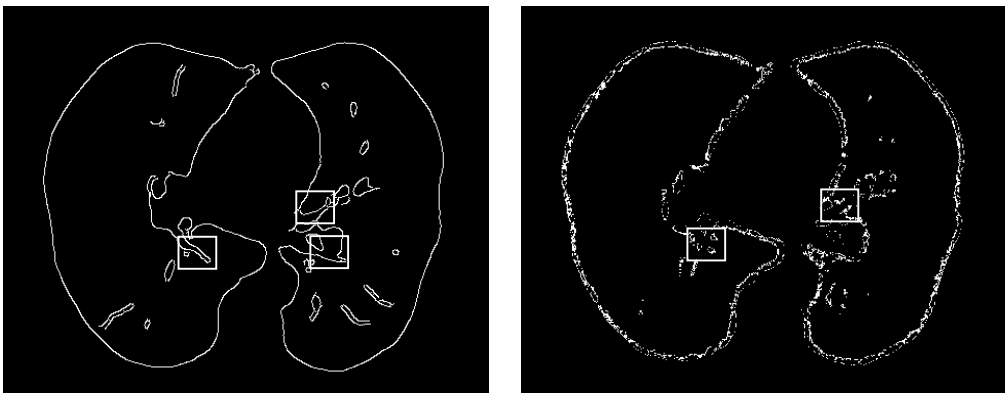

(c) (d)

Figure 6.7 (contd.)

The square indicated regions presented in Figure 6.7(b)-(d) show lung boundaries are not accurately segmented. The edge detection methods implemented in Figure 6.7(b)-(d) cannot effectively identify the high intensity veins (red arrows indicated in Figure 6.6) located on lung boundaries as a part of the lung regions.

The images processed by the edge detection methods cannot display detailed edge information in the image well. The Sobel operator and the Canny edge detector methods cannot detect intact edge information and the Holder exponent cannot gain a continuous edge. So simply implementing the edge detection methods is unable to obtain the lung boundary precisely. Edge optimisation techniques need to be used for lost edge information recovery, such as morphological operators [59] and rolling ball algorithm [61]. However, the proposed lung segmentation technique is capable of detecting a more exact lung boundary, as shown in Figure 6.7(a). The veins existing on lung boundaries are correctly classified as a part of lung regions, and they are located inside the lung boundaries. So the proposed lung segmentation method is capable of determining the most accurate lung boundary without losing any lung region information.

Chapter 7

Results and Analysis: Lung Nodule Detection

This chapter presents and analyses the results of the lung nodule detection technique. The nodule detection results are automatically generated from the lung nodule detection technique described in Chapter 5.

The implementations of the techniques are tested with a large number of consecutive lung image sets to determine the effectiveness of the technique described. The detection rate and false positive rate are computed to evaluate the technique's efficiency. The accuracy of the results is quantified by implementing the nodule detection technique on the nodules with different sizes, shapes and locations. The detection rate and false positive rate before and after the nodule candidate enlargement process and rule based filtering process are compared. Detailed evaluation and comparative analysis are performed on the results obtained from the techniques.

Section 7.1 presents some of the results obtained using the proposed lung nodule detection technique. Section 7.2 gives evaluation and comparative analysis of the results. The technique parameters used for the nodule detection technique are discussed in Section 7.3.

7.1 Experimental Results

In order to validate the efficiency of the proposed lung nodule detection technique, 10 sets of consecutive HRCT slices are used in our experiment. Both detected and undetected nodules are presented in this section so the advantages and limitations of the nodule detection technique can be summarised. The nodules that need to be detected on the images shown in Figure 7.1-7.4 are indicated by golden

arrows. Red arrows are used to indicate the detected nodules among the filtered nodule candidates. Section 7.1.1 gives the nodules that are detected by the proposed nodule detection technique. Undetected nodules are presented in Section 7.1.2.

7.1.1 Detected Nodules

The detected nodules presented in this section are spherical, star and quadrilateral shapes. They also vary in size and location.

Spherical shape nodules

Figure 7.1 shows the nodule detection results for spherical shape nodules. A continuous lung image set is shown in Figure 7.1(a)-(e) that contains a number of spherical shape nodules.

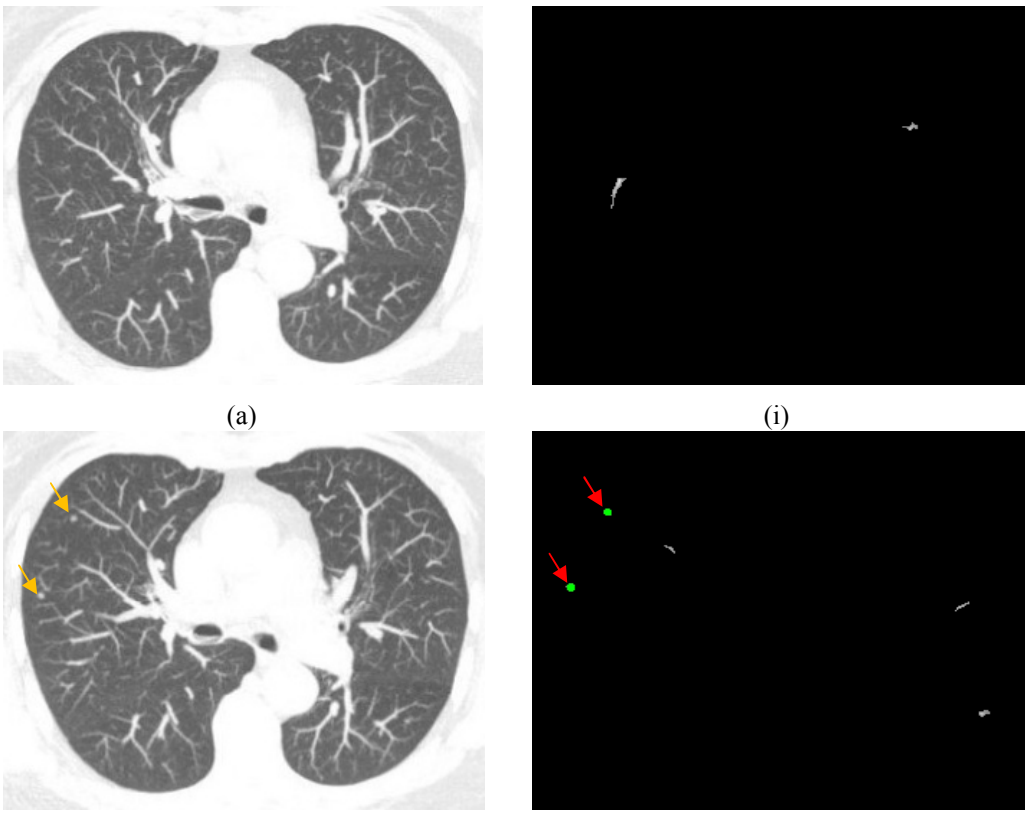

(a) (i)

(b) (ii)

Figure 7.1 Spherical shape nodule detection results

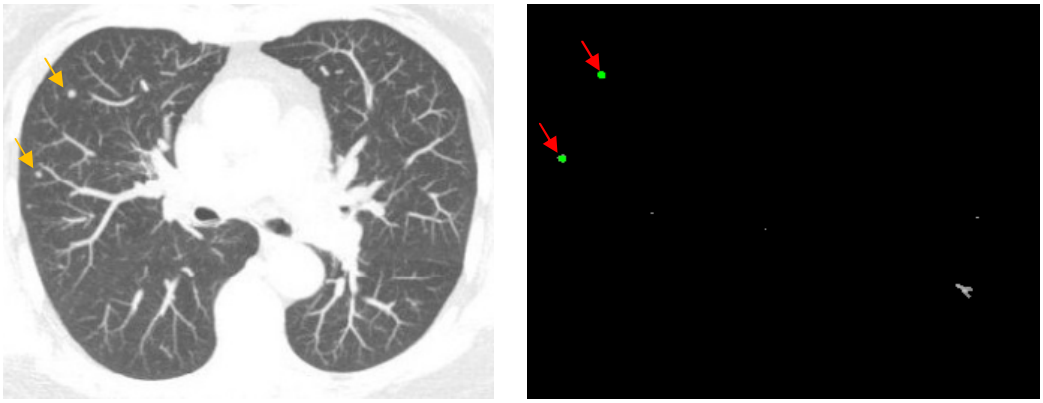

(c) (iii)

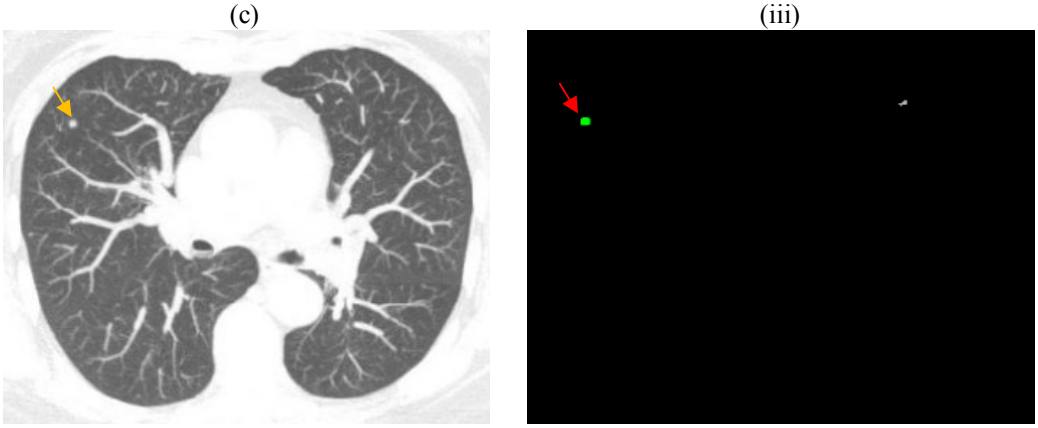

(d) (iv)

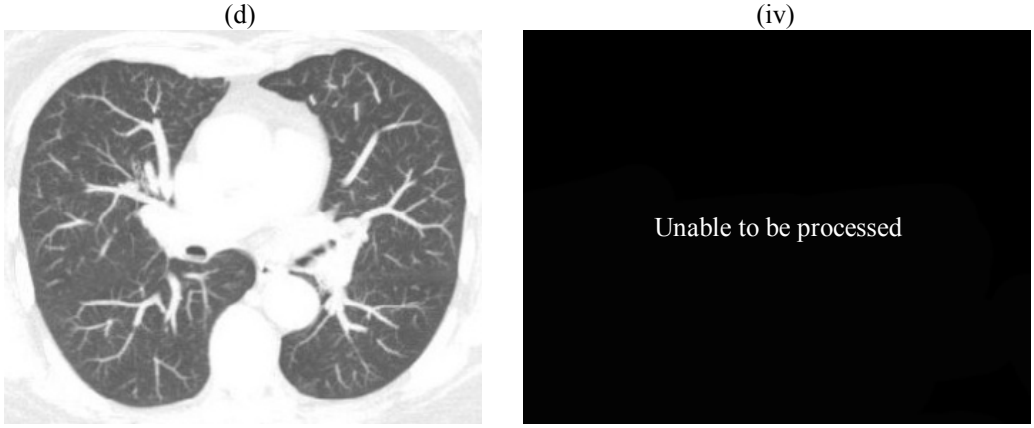

(e) (v)

Figure 7.1 (contd.)

The spherical shape lung nodules are detected and highlighted in green, as shown in Figure 7.1(ii)-(iv). In Figure 7.1(i)-(iv), the majority of the false positives are eliminated and a fewer number of nodule candidates processed by the rule based filtering process are left over, which helps to improve the nodule detection

accuracy. As mentioned in Figure 5.1, the result image of Figure 7.1(v) is unable to be processed.

Star shape and quadrilateral shape nodules

The lung images shown in Figure 7.2(a)-(d) are selected from four different continuous image sets. Figure 7.2(a) shows a star shape nodule which is detected in Figure 7.2(i). Quadrilateral shape nodules are presented in Figure 7.2(b)-(d), which are detected and shown in Figure 7.2(ii)-(iv).

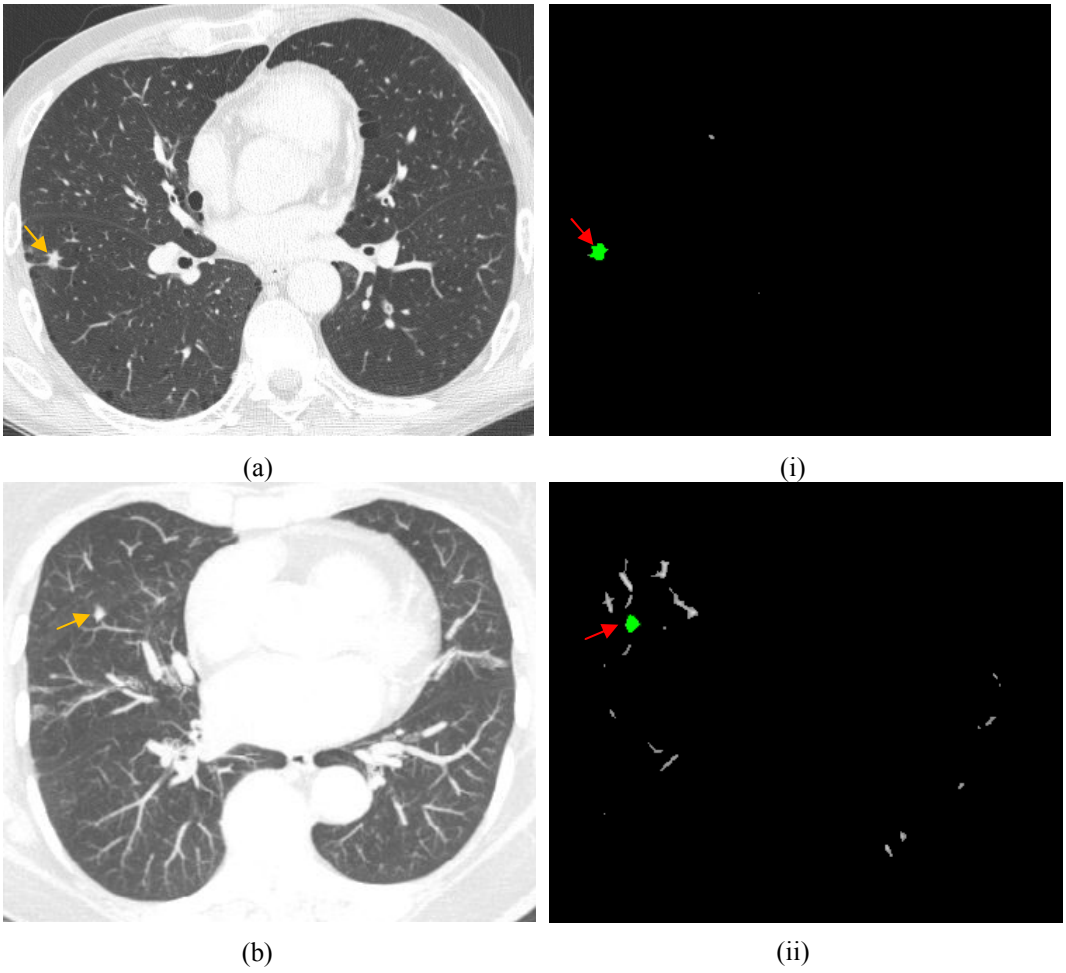

(a) (i)

(b) (ii)

Figure 7.2 Star shape and quadrilateral shape nodule detection results

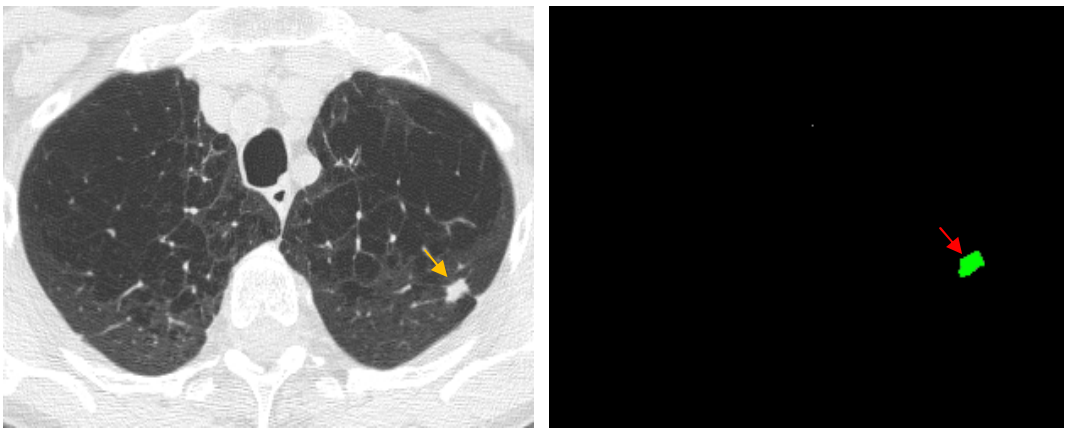

(c) (iii)

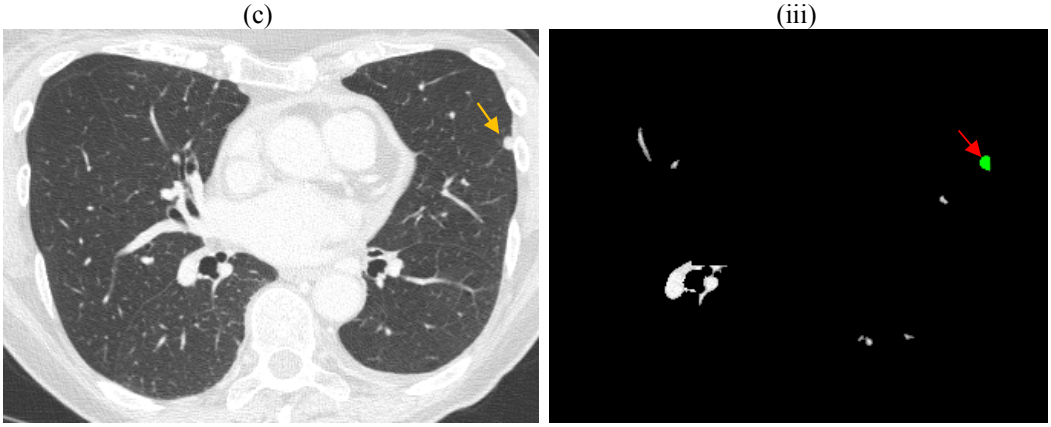

(d) (iv)

Figure 7.2 (contd.)

As seen in Figure 7.2, the star and quadrilateral shape nodules can be accurately detected. The nodule detection technique is able to detect them either located inside the lung regions (see Figure 7.2(a)-(c)) or on lung boundaries (see Figure 7.2(d)). However, the nodules in highly irregular shapes or attached to veins cannot be detected using the proposed nodule detection technique.

7.1.2 Undetected Nodules

This section presents the nodules that are unable to be detected by the nodule detection technique. These are either in irregular shapes or attached to veins.

Irregular shape nodules

Figure 7.3 lists the nodules that are unable to be detected because they are in irregular shapes. Irregular nodule shapes are hard to determine using the radii ratio metric and the area ratio metric. Those irregular shape nodules are either located on lung boundaries (see Figure 7.3(a)) or inside of the lung regions (see Figure 7.3(b)-(c)).

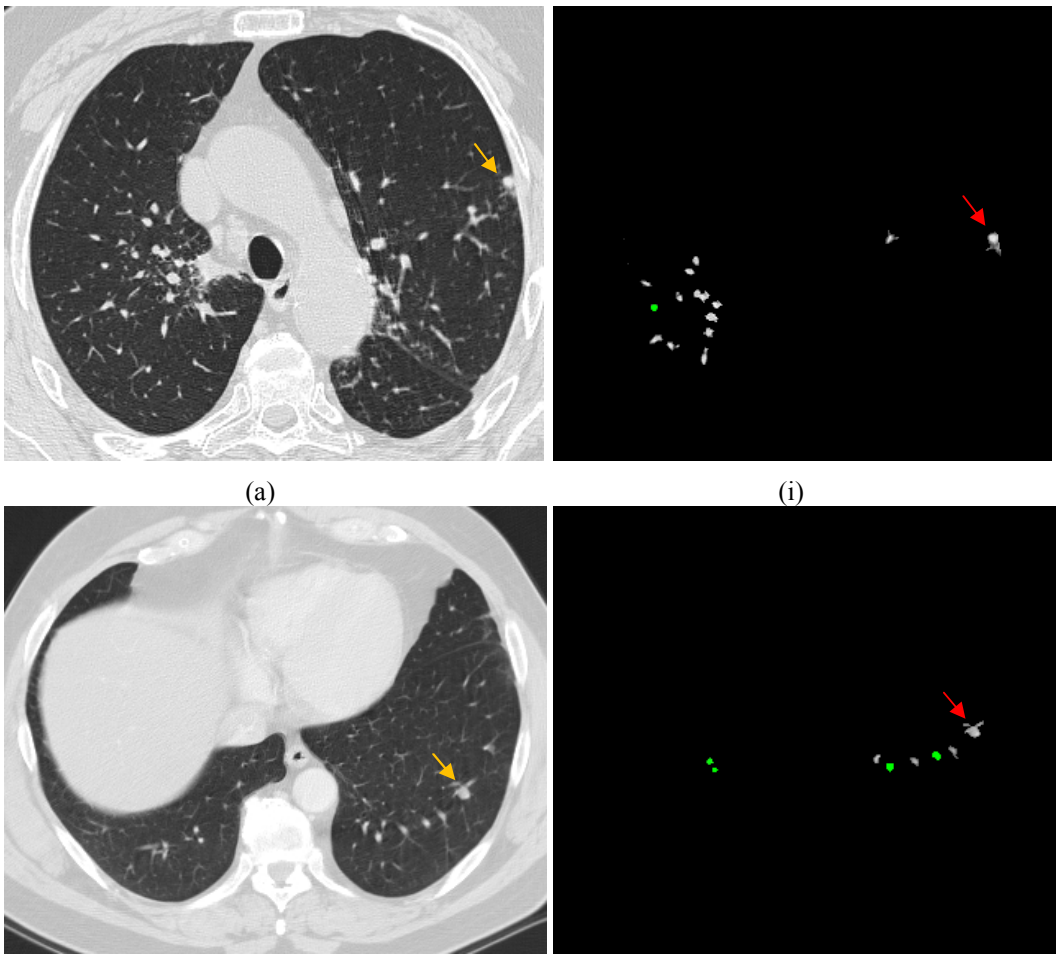

(a) (i)

(b) (ii)

Figure 7.3 Irregular shape nodule detection results

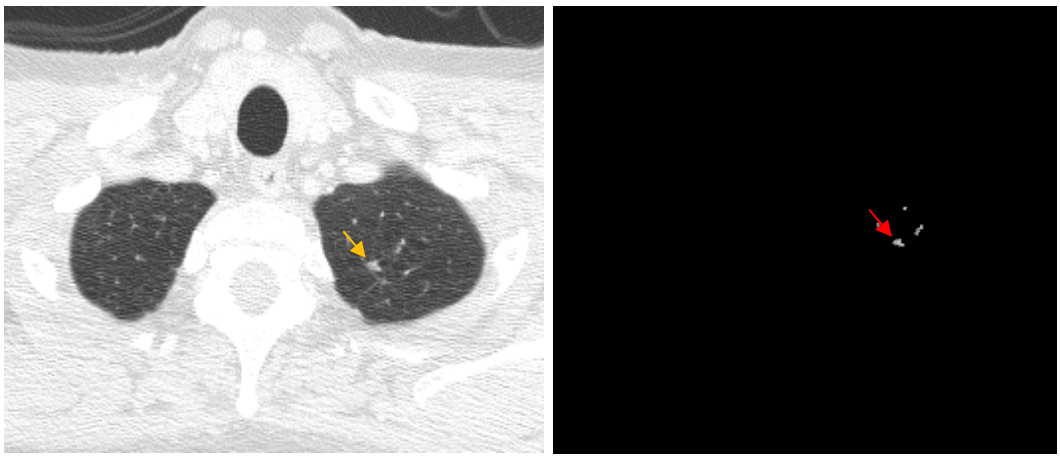

(c) (iii)

Figure 7.3 (contd.)

In Figure 7.3(i)-(ii), the green colour highlighted nodule candidates are incorrectly identified as nodules. Those highlighted nodule candidates are false positives since they are not indicated by the radiologist in Figure 7.3(a)-(b). The output image of Figure 7.3(iii) does not contain any nodule candidates that are identified as nodules by the proposed nodule detection technique.

Nodules attached to veins

As mentioned in Section 5.3.2, veins have similar intensity with lung nodules. So if nodules attach to veins, their shapes present differently on lung images. Figure 7.4 shows the nodule detection results of the nodules attached to veins.

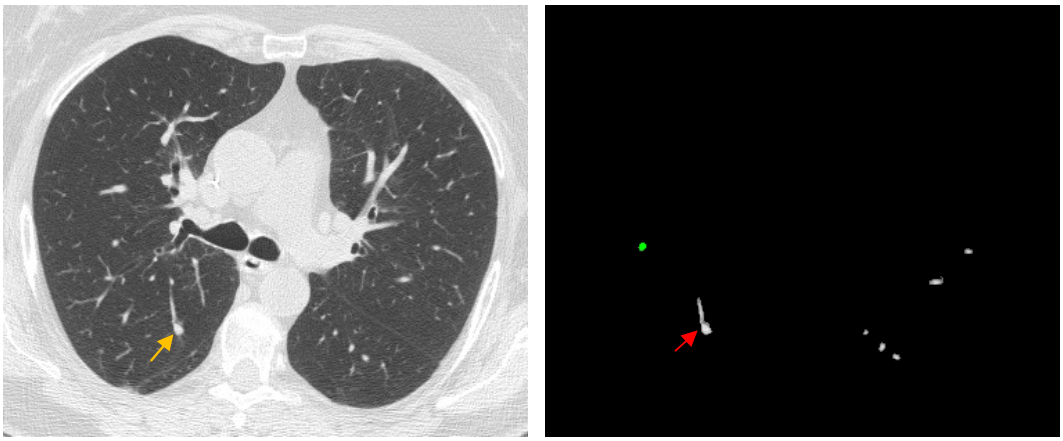

(a) (i)

Figure 7.4 Nodules attached to veins nodule detection results

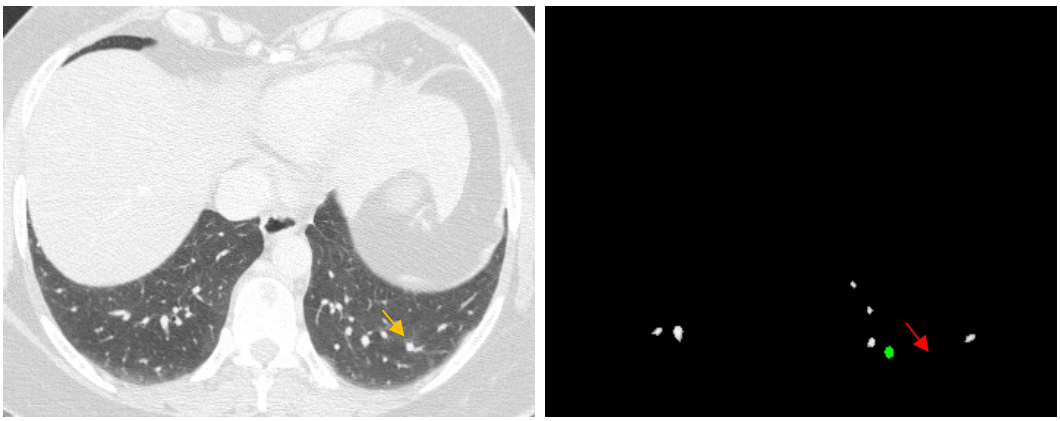

(b) (ii)

Figure 7.4 (contd.)

In Figure 7.4(i), the red arrow indicated nodule candidate is supposed to be a spherical shape nodule, as indicated in Figure 7.4(a). Shape variation makes nodules hard to detect using the proposed nodule detection technique. Nodules can be eliminated during the centroid based filtering process due to their inaccurate shapes. In most cases, nodules are not detected since they do not exist among the filtered nodule candidates, as shown in Figure 7.4(ii). The false positives in the images shown in Figure 7.4(i)-(ii) are highlighted in green.

7.2 Evaluation and Comparative Analysis

To evaluate and show the effectiveness of the lung nodule detection technique, result discussion and comparative analysis are given in this section. The total number of 75 lung nodules is collected from 100 slices as testing data. They range in size from 1mm to 20mm. The nodules are categorised into spherical, star, and quadrilateral shape. They are also located differently on lung regions. Some of the nodules are well-circumscribed and others are located on the lung boundary.

Section 7.2.1 discusses the detection rate and false positive rate with respect to the nodule size, shape and location. Detection rate is computed as the ratio of the number of detected nodules to the total number of nodules. The detection rate before and after the nodule candidate enlargement process and rule based filtering process is compared in Section 7.2.2. Section 7.2.3 presents the comparison

between our lung nodule detection results and the lung nodule detection results presented in other people's work.

For the nodule detection, we consider:

- True Positive (TP): The slices labelled by the radiologist to have the nodules and recognised so by the proposed nodule detection technique.
- False positive (FP): The slices recognised to have the nodule by the proposed nodule detection technique, but not labelled so by the radiologist.
- True Negative (TN): The slices labelled by the radiologist not to have the nodule and not recognised so by the proposed nodule detection technique.
- False Negativity (FN): The slices labelled by the radiologist not to have the nodule, but recognised so by the proposed nodule detection technique.

7.2.1 Result Discussion

The discussion of the nodule detection results is performed on the detection rate and false positive rate of the nodules which vary in size, shape and location. Table 7.1-7.3 presents the nodule detection rate and false positive rate. The experiment results in each table are generated by implementing the proposed technique on the independent testing data. Table 7.1 shows the experiment results based on different nodule size groups. The given images have 1mm spacing between two slices and the lung nodule is usually 25mm in size.

Table 7.1 Experiment results based on different nodule sizes

Nodule Size	Nodule Num	Nodule Missed	Detection Rate [%]	FP/slice
1-5mm	9	1	88.89	0.08
6-10mm	29	3	89.66	0.29
11-15mm	15	2	86.67	0.15
16-20mm	22	2	90.91	0.21

In Table 7.1, the small nodules ranging in size from 1mm to 5mm are detected with a detection rate 88.89%, which is similar to the detection rate of larger size nodules (6-20mm). So the proposed nodule detection accuracy is not affected by

nodule size variation. The proposed nodule detection technique has the best performance for the nodules sized between 16mm to 20mm, which has the detection rate of 90.91%. The nodules sized from 6mm to 10mm are most likely to be identified as nodules since they have a high false positive rate (about 0.29/slice). A large number of nodule candidates sized from 6mm to 10mm also causes a high false positive rate. The proposed technique is able to detect 67 nodules with different sizes and encountered 11 false positives in these cases.

Based on the detection rate shown in Table 7.1, the nodule size variation does not affect the accuracy of nodule detection. The overall detection rate for the nodules in different size groups is more than 86%, which shows the effectiveness of the proposed nodule detection technique. Table 7.2 shows the detection rate and false positive rate based on different nodule shape groups.

Table 7.2 Experiment results based on different nodule shapes

Nodule Shape	Nodule Num	Nodule Missed	Detection Rate [%]	FP/slice
Spherical	31	1	96.77	0.11
Star	19	2	89.47	0.29
Quadrilateral	25	2	92.00	0.16

As mentioned in Section 5.4.3, the nodules in spherical and quadrilateral shape have special area ratio and radii ratio. The spherical shape nodules have their area ratio higher than the area ratio of the star and quadrilateral shape nodules. The quadrilateral shape nodules have their radii ratio lower than the radii ratio of the spherical and star shape nodules. Based on those characters, the spherical and quadrilateral shape nodules can be accurately detected. Table 7.2 indicates that the detection rates for both spherical and quadrilateral shape nodules are higher than the detection rate of the star shape nodules. The nodules in spherical shape can be accurately detected due to their large area ratio, as shown in Figure 7.5(a). Quadrilateral shape nodules can have small radii ratio, as illustrated in Figure 7.5(b).

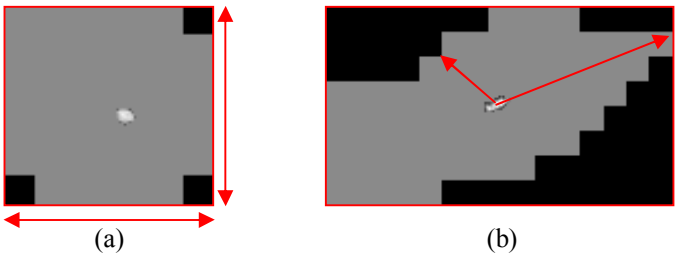

Figure 7.5 (a) Spherical shape nodule with large area ratio (b) Quadrilateral shape nodule with small radii ratio

In Table 7.2, the detection rate of star shape nodules is lower than the detection rate of spherical and quadrilateral shape nodules, but it is still acceptable. The star shape nodules have a higher false positive rate (about 0.29/slice) than the spherical and quadrilateral shape nodules. The high false positive rate of star shape nodules is caused by the large number of veins present after the nodule candidate extraction. However, the false positive rate for the spherical shape nodules is lower as they rarely exist among the filtered nodule candidates. The proposed technique is able to detect 70 nodules with different shapes and encountered 12 false positives in these cases. Table 7.3 shows the detection rate and false positive rate based on different nodule location groups.

Table 7.3 Experiment results based on different nodule locations

Location	Nodule Num	Nodule Missed	Detection Rate [%]	FP/slice
Well-circumscribed	44	4	87.91	0.20
Lung Boundary	15	1	83.33	0.07
Vascular	16	6	62.50	0.44

Nodule candidates are generated by combining the α-images that contain nodule information. So either the nodules are well-circumscribed or located on lung boundaries that can be extracted completely and accurately. Table 7.3 indicates the detection rate of well-circumscribed nodules (about 87.91%) and the nodules located on lung boundaries (about 83.33%) are similar. The nodules attached to veins are hard to detect as their shapes present differently after attaching to veins. In Table 7.3, the detection rate of the nodules attached to veins is low (about 62.50%), which means the detection rate is greatly affected by the nodule shape

variation. The proposed technique is able to detect 62 nodules with different sizes and encountered 17 false positives in these cases.

Based on the results shown in Table 7.1-7.3, we can conclude that nodules in different sizes are the least sensitive to nodule detection since it has less false positives. The experiment results revealed that irregular nodule shapes yield higher sensitivity, such as the nodules attached to veins. So we can conclude that the nodules in different locations are the most sensitive to nodule detection as they have the most number of false positives.

7.2.2 Comparison with Unprocessed Results

In Section 7.2.1, the experiment results are obtained after the nodule candidate enlargement process and the rule based filtering process. The experimental results obtained before the processes are presented in this section. In order to view the efficiency of the processes, the detection rate and false positive rate generated before and after the processes are compared.

Nodule candidate enlargement process

The nodule candidate enlargement process is based on enlarging nodule candidates smaller than 20mm. The detection rate and false positive rate of the nodules are different before and after the nodule candidate enlargement process. Figure 7.6 indicates the comparison of the detection rate and false positive rate before and after the nodule candidate enlargement process.

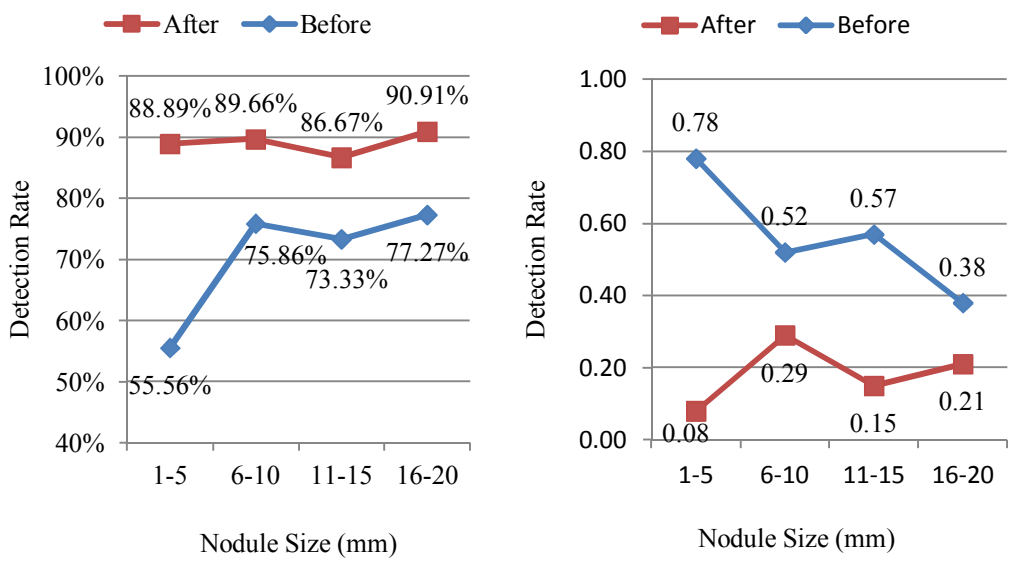

Figure 7.6 The effect of nodule enlargement process on nodule size (a) Detection rate comparison (b) False positive rate comparison

In Figure 7.6(a), the detection rates of the nodules in different size groups before the nodule candidate enlargement process is lower than the detection rate after the nodule candidate enlargement process. Small size nodules (1-5mm) are especially difficult to detect without size enlargement. Before the nodule candidate enlargement process, the detection rate of nodules sized from 1mm to 5mm is only 55.56%, which means only half of the nodules can be detected. The overall detection rate of the nodules sized from 6mm to 20mm is about 75%, which is lower than the overall detection rate after the nodule candidate enlargement process (about 89%). Figure 7.6(b) shows the false positive rate of the nodules sized between 1mm to 5mm before the nodule candidate enlargement process is 0.78, which means false positives nearly appear on each slice. The false positive rates of the nodules sized from 6mm to 20mm are higher than the false positive rates after the nodule candidate enlargement process. Figure 7.6(a)-(b) shows that the nodule candidate enlargement process improves the detection rate and the false positive rate of nodules sized 1mm to 5mm the most.

Effects of the nodule candidate enlargement process:

- Makes the nodule detection technique insensitive with small size nodules.
- Increase the nodule detection rate.
- Reduces the number of false positives and decreases the false positive rate for nodule detection.

Rule based filtering process

Rule based filtering process is implemented to reduce the number of nodule candidates (false positives). As mentioned in Section 5.3, the rule based filtering process removes nodule candidates based on nodule candidate centroid location, intensity and frequency criteria. Figure 7.7-7.9 gives the comparison of the detection rate and false positive rate of the nodules varying in size, shape and location before and after the rule based filtering process. Figure 7.7 shows the effect of the rule based filtering process on nodule size.

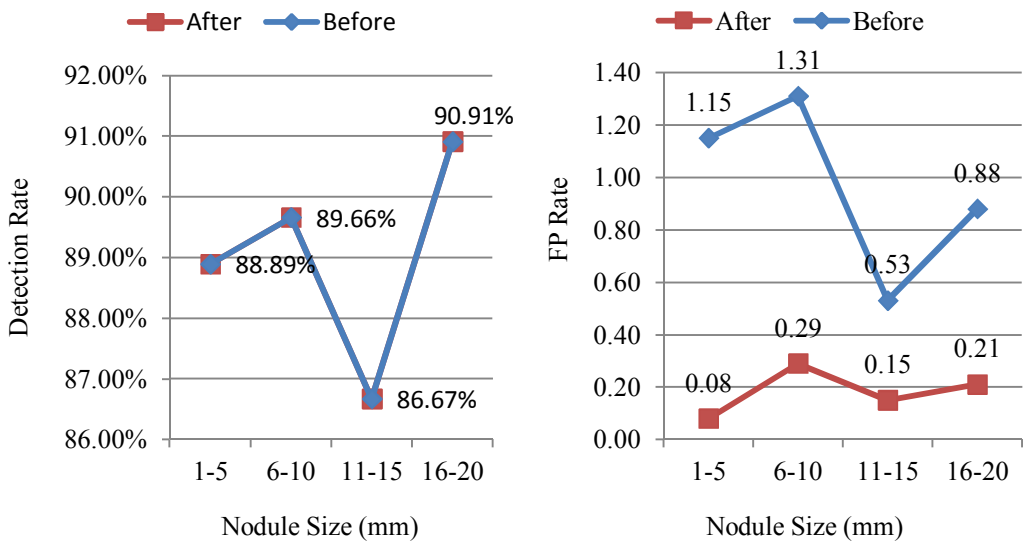

Figure 7.7 The effect of the rule based filtering process on nodule size (a) Detection rate comparison (b) False positive rate comparison

From Figure 7.7(a), the detection rate of the nodules in different sizes is not changed before and after the process due to the fact that the rule based filtering process criteria have no relation to nodule candidate size. However, the false positive rate of the nodules in different size groups is reduced after the rule based

filtering process, as shown in Figure 7.7(b). The false positive rate of the nodules smaller than 10mm is greatly reduced after the rule based filtering process. So the process removes a large number of small size nodule candidates, such as small lung tissue regions. Figure 7.8 indicates the effect of the rule based filtering process on nodule shape.

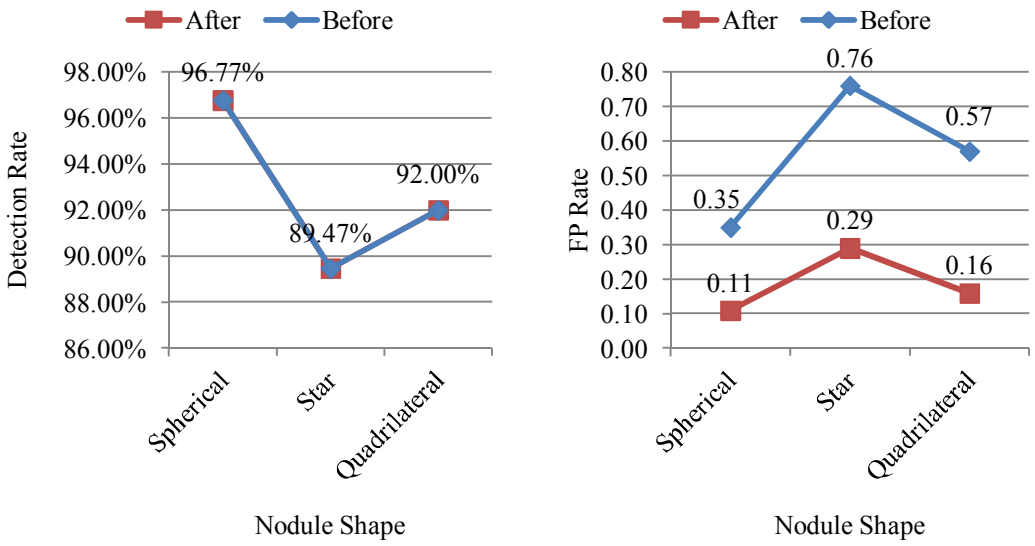

Figure 7.8 The effect of the rule based filtering process on nodule shape (a) Detection rate comparison (b) False positive rate comparison

In this research, the detected nodules are in spherica, star and quadrilateral shape, and all of those nodule shapes have centroids located inside. So the nodule candidates in those three shapes are not removed by the rule based filtering process, and their detection rate stays the same before and after the process, as shown in Figure 7.8(a). Figure 7.8(b) shows the false positive rate of the nodules in star shape (about 0.76/slice) and quadrilateral shape (about 0.57/slice) is high as a large number of star shape and quadrilateral shape nodule candidates were extracted from veins. The nodules in spherical shape rarely appear on the lung images, so its false positive rate is low (about 0.35/slice). Spherical nodule candidates can only be removed based on the nodule candidate intensity and frequency criteria. So the false positive rate variation of the spherical nodules before and after the rule based

processing is small. Figure 7.9 illustrates the effect of the rule based filtering process on nodule location.

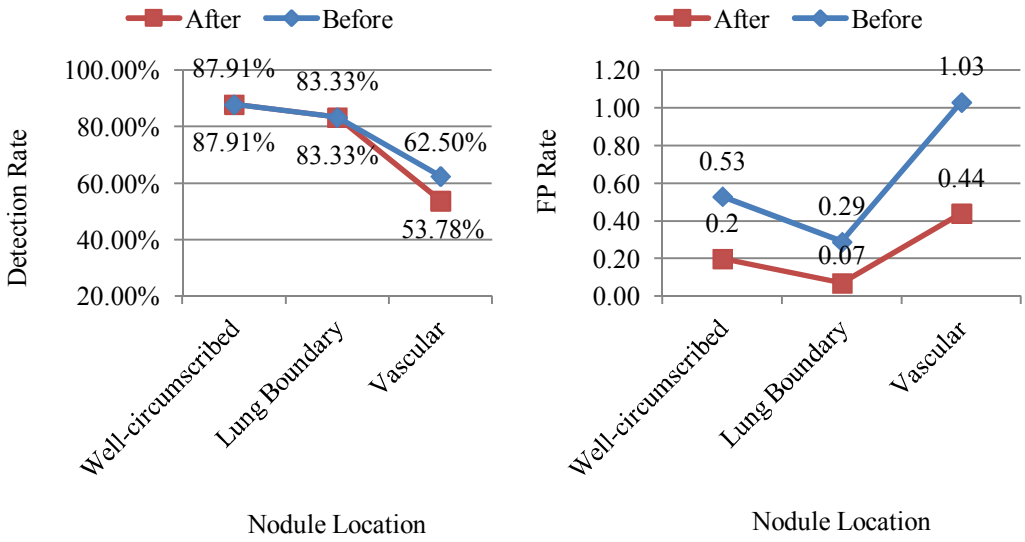

Figure 7.9 The effect of the rule based filtering process on nodule location (a) Detection rate comparison (b) False positive rate comparison

As seen in Figure 7.9(a), the detection rate of well-circumscribed nodules and the nodules located on lung boundaries is not changed before and after the rule based filtering process. The detection rate of nodules attached to veins reduces from 62.50% to 53.78% after the rule based filtering process. This is because nodule shapes are inaccurately extracted after the rule based filtering process. Some of the nodules are removed with their centroid located outside, which is caused by inaccurate shape presenting. The false positive rate of the nodules with different locations is decreased after the rule based filtering process, as shown in Figure 7.9(b).

Effects of the rule based filtering process:

- Reduces the number of false positives and decreases the false positive rate for nodule detection.
- Speeds up the nodule detection process by removing nodule candidates.

After comparing the experiment results generated before and after the processes, it can be concluded that they have had an outstanding impact by increasing the detection rate and decreasing the false positive rate. The nodule candidate enlargement process greatly improves the nodule detection accuracy since nodule candidate shapes are accurately determined. After the nodule candidate enlargement process, the nodule detection rate is increased and the false positive rate is decreased. However, the experiment results show the rule based filtering process only decreases the false positive rate for nodule detection, and it is not helpful with increasing the detection rate.

7.2.3 Comparison with Other Research

To evaluate and show the effectiveness of the nodule detection technique described in this work, a comparative analysis is performed. According to the detection rates and false positive rates shown in Table 7.1-7.3, the overall performance of the proposed technique is conclude in Table 7.4.

Table 7.4 Performance results of the proposed method

	Size	Shape	Location
Detection Rate [%]	89.33	93.33	82.67
False positive Rate	0.15	0.16	0.23
Overall Detection Rate [%]		88.44	
Overall false positive Rate		0.18	

The overall detection rate and false positive rates are generated by taking the average of the detection rates and false positive rates of the nodules varying in size, shape and location, as shown in Table 7.4.

The results of the groups working on this subject are presented in Table 7.5 for comparison. Table 7.5 shows the performance comparison of our method with that of Lin et al.'s [35] CCN (Convolution Neural Network) method, Lee et al.'s [37] GATM (Genetic Algorithm Template Matching), Kanazawa et al.'s [42] rule-based detection method and Dehmeshki et al.'s [38] GA (multi-model genetic algorithm) method, in which Kanazawa et al. applied on 450 subjects consisting of 15750

slices, Lin et al.'s CCN method is tested on 42 chest radiographs, Lee et al.'s GATM method was applied to 15 clinical cases consisting of 557 slice images.

Table 7.5 Performance comparison

Method	Detection Rate [%]	FP/slice
Proposed Method	88.44	0.18
Lin et al.	80.00	2.50
Lee et al.	70.00	1.10
Kanazawa et al.	90.00	0.25
Dehmeshki et al.	90.00	3.71

The overall performance of the proposed system is 88.44% correct detection and the false positive rate per slice is as low as 0.18. This result shows that we improve the detection rate with very low false positives. The statistical results in general can indicate that the proposed method is compatible to that of Kanazawa et al. but with less false positives. Compared with Lin et al.'s method and Lee et al.'s method, the proposed method performance is outperformed by either correct detection rate or false positive rate per slice. Although no significant improvement can be seen in the results of the proposed method with respect to the previous techniques and specifically Kanazawa et al.'s method and Dehmeshki et al.'s method, Kanazawa et al.'s method is unable to detect nodules smaller than 4mm. Adding these nodules to their dataset probably makes them less sensitive, therefore, the exploited dataset considerably affects the system's sensitivity.

7.3 Analysis of Parameter Variation

Some of the parameters used in the nodule detection technique are discussed and analysed in this section. Those parameters are evaluated by comparing the results generated by using different parameter values. In order to view the effect of assigning different parameter values for the nodule detection technique, the parameters are tested on the lung image that has a large star shape nodule indicated, as presented in Figure 7.10.

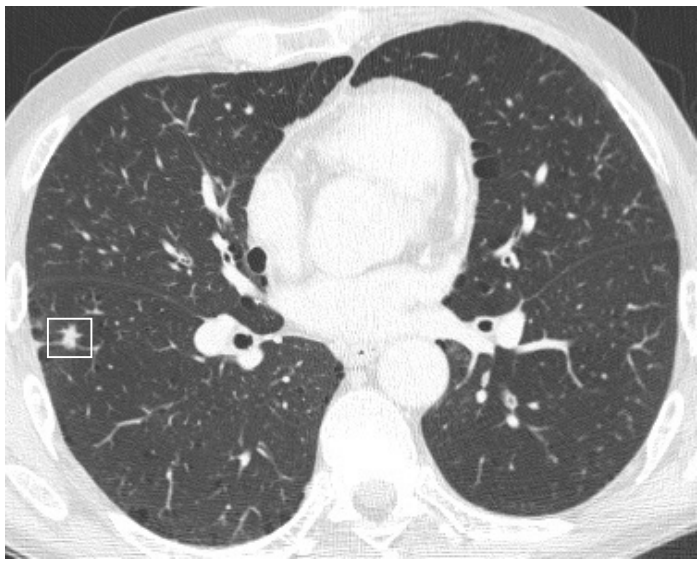

Figure 7.10 Lung image with a star shape nodule indicated

7.3.1 Intensity Measure Comparative Analysis

The following cases need to be considered when calculating the measures for α-value estimation.

- The lung image needs to be padded in order to consider neighbourhoods near the image border, which may cause boundary overlapping. α-values at the borders will be calculated incorrectly if we do not pad the image suitably. The lung image is padded with zero intensity pixels, which artificially lower the value of μ for the pixels near the image edges [48].
- To estimate α we must take the natural logarithm of $\mu_r(m, n)$. In Sum measure and Maximum measure, if the intensity measure $\mu_r(m, n)$ in a neighbourhood is 0 (black), the $\log(\mu_r(m, n))$ is undefined. As a solution, we consider any zero intensity 'background'. We assign an arbitrary α-value which lies outside of the range $0 < \alpha_{min} < \alpha_{max} < \infty$, that is any negative value. In Inverse minimum measure, if the intensity measure $\mu_r(m, n)$ is 1 (white), the $\log(\mu_r(m, n))$ will also be undefined. So we must consider white pixels as background because it is these that will be problematic. These pixels will be drawn as white in the α-

image. However, in Iso measure, we will not encounter the problematic 0 or 1 measure situation as $\mu_r(m, n)$ is always greater than, or equal to 1.

The way of determining the best measure is to generate α-images from the lung image shown in Figure 7.10, by using the four measures, and compare the α-images as shown in Figure 7.11. We choose the measure that generates the α-image with the most nodule information evident. Figure 7.11 shows the Sum measure has the best performance. The Inverse Minimum measure generates the α-image with the least nodule information evident.

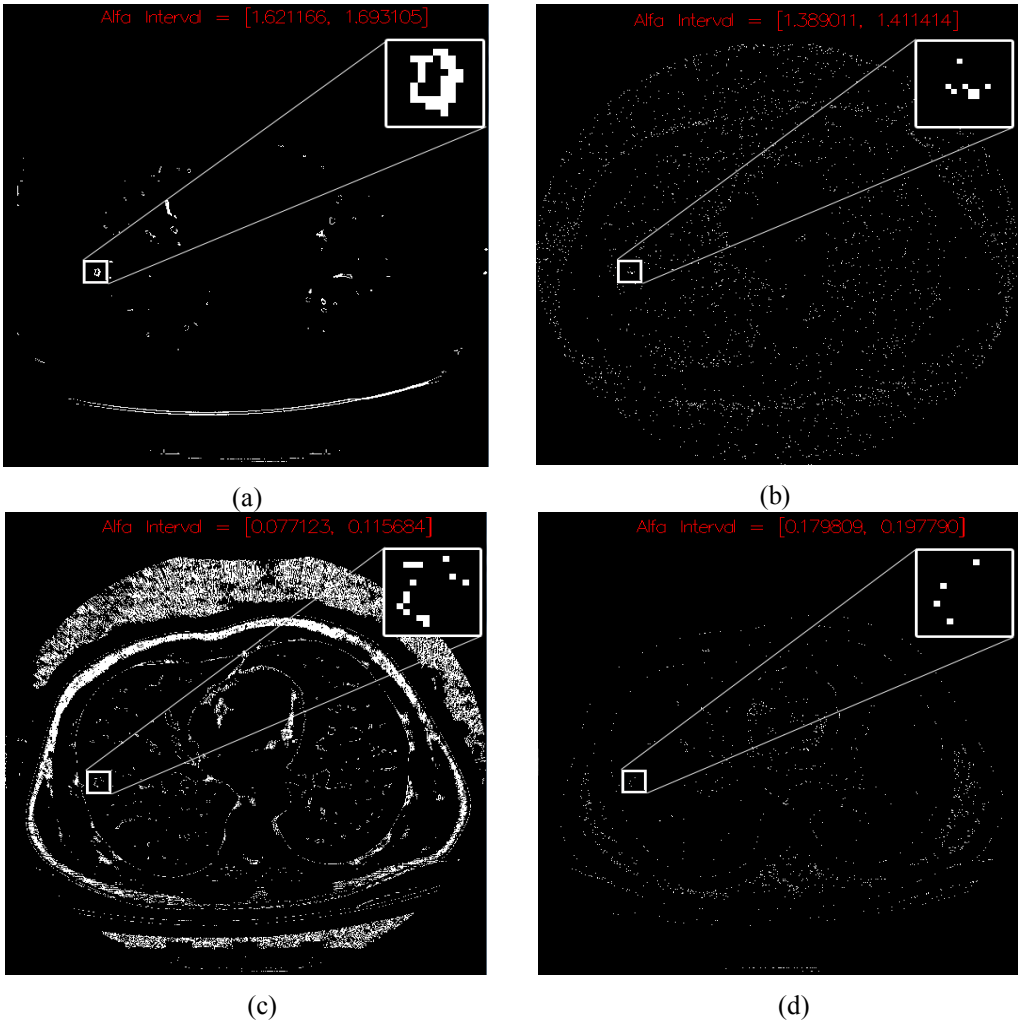

Figure 7.11 Type of intensity measures: (a) Sum Measure (b) Iso Measure (c) Maximum Measure (d) Inverse Minimum Measure

The error rate of each measure is calculated by dividing the number of missed nodule pixels by the total number of nodule pixels. The error rate of each measure type is compared in Figure 7.12. The Sum measure has the lowest error rate and it generates the α-image containing the most the nodule information so Sum measure is selected for α-value estimation.

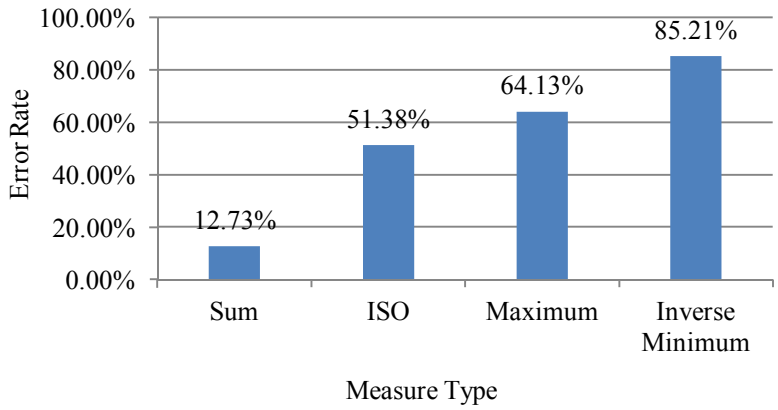

Figure 7.12 Error rate of the measures

7.3.2 Sum Measure Techniques Comparison

As introduced in Section 3.2.1, Sum measure techniques include Multiple concentric discs and Multiple concentric windows. Nilsson [52] described how the Multiple concentric windows intensity measure outperformed the Multiple concentric discs intensity measure. Both of the Sum measure techniques are implemented on the lung image given in Figure 7.10. The effectiveness of the techniques can be tested by comparing combined α-images and α-histograms.

Comparing combined α-images

The nodule shown in Figure 7.13(a) gives more accurate nodule information. The nodule in Figure 7.13(a) is clearly segmented and has the same size as the nodule shown in Figure 7.10. In Figure 7.13(b), the nodule is segmented with part of vein region included so the nodule size is slightly larger than the original nodule. Moreover, the combined α-image in Figure 7.13(a) shows up less noise information

than the combined α-image shown in Figure 7.13(b). Less noise information in the combined α-image helps to improve the accuracy of nodule detection.

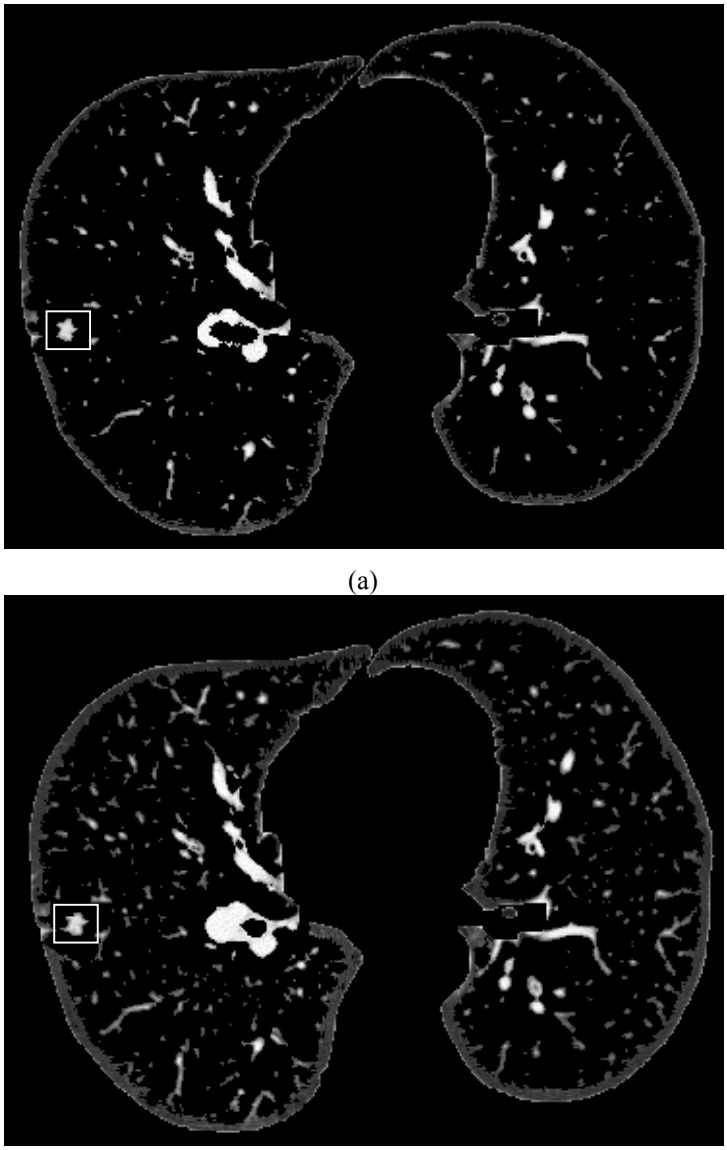

(a)

(b)

Figure 7.13 Nodule indicated combined α-image with sum measure based on: (a) Multiple concentric windows (b) Multiple concentric discs

Comparing α-histograms

Alfa histograms generated from both Sum measure techniques are shown in Figure 7.14. As described in Section 3.2.1, α gives the degree of intensity variation for each pixel, which is the local information of the point regularity. For instance,

pixels having α-value equal to 2 are pixels where the measure is regular, i.e., where the probability of the signal changes is small. Pixels with α-value not equal to 2 denote that non-regular zones exist. For instance, pixels with α-value < 2 or α-value > 2 denote the regions characterised by a high gradient or the regions of discontinuities of the signal or its derivative, respectively. In Figure 7.14(a), most pixels have the α-value around 2.04, which means those pixels have a small degree of intensity variation. In Figure 7.14(b), pixels with the α-value around 1.94 have a degree of intensity variation slightly larger than the pixels with α-value 2.04.

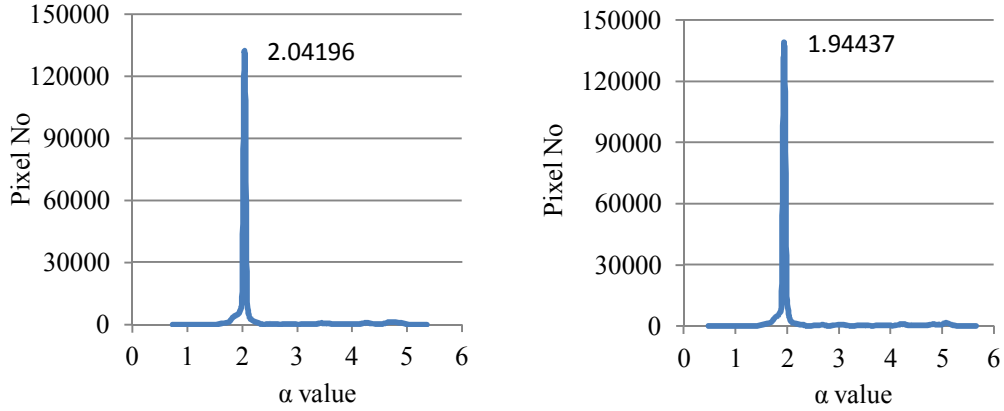

Figure 7.14 α-histograms: (a) Multiple concentric windows (b) Multiple concentric discs

The α-value estimated by Multiple concentric windows is higher than the α-value estimated by Multiple concentric discs. So the pixels shown on the α-image generated by the Multiple concentric windows have nearly the same degree of intensity variation.

7.3.3 Alfa Interval Number Variation

The variation of the α-interval number reflects the size of the α-range for each α-interval. Large α-interval number minimises the α-range and reduces the number of pixels that belong to each α-interval. So the α-interval number variation reflects the amount of information present on α-images. We used the α-interval number 100 for our experiment, which is the same as the interval number that Nilsson [52] used.

We designed a scheme for comparing the effects of applying different α-interval numbers. Combined α-images generated by using the interval numbers 50, 100 and 150 are compared in Figure 7.15.

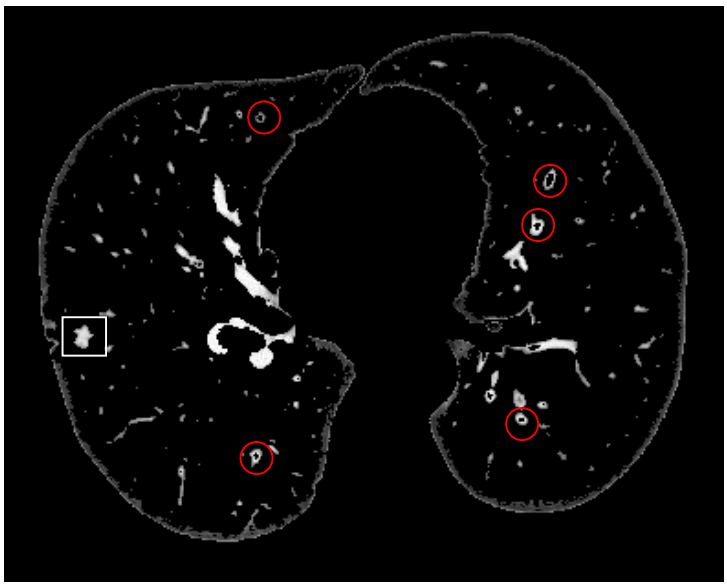

(a)

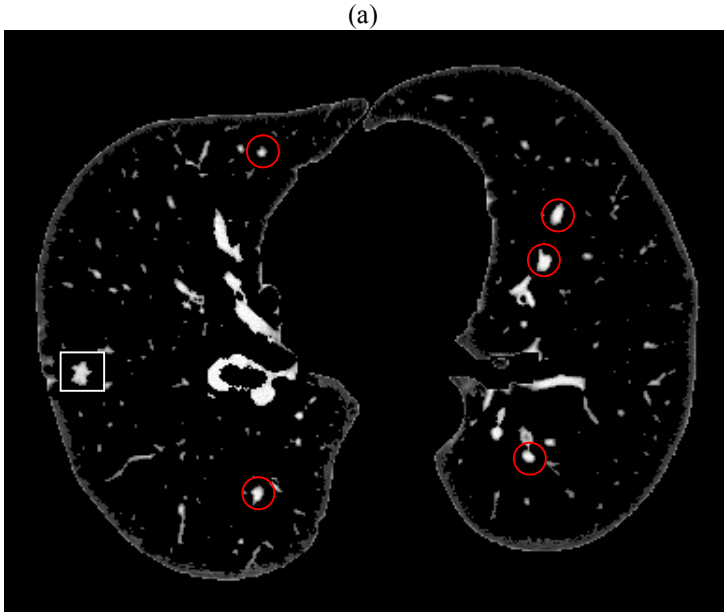

(b)

Figure 7.15 Effect of α-intervals to α-images (a) 50 intervals (b) 100 intervals (c) 150 intervals

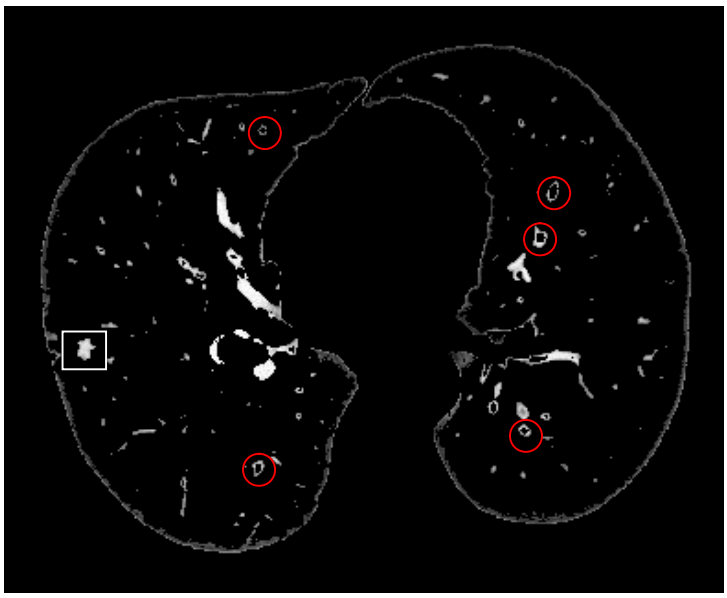

(c)

Figure 7.15 (contd.)

Combined α-images shown in Figure 7.15 are compared based on the following two rules:

- *Nodule information completeness*: Figure 7.15(c) shows the combined α-image contains less nodule information (square indicated) by comparing it to the nodule information shown on the original image in Figure 7.10.
- *Vein information completeness*: In Figure 7.15(a) and (c), some pixel information on veins (circle indicated) is lost. However, the intensity variation of the vein pixels is small, so they are supposed to be shown on one combined α-image as seen in Figure 7.15(b).

After the combined α-images comparison, only the combined α-image shown in Figure 7.15(b) does not have the nodule and vein information lost. So the combined α-image generated by using 100 intervals has the most accurate pixel information shown.

Chapter 8

Summary

8.1 Conclusion

The lung segmentation method has important value in clinical applications and it is also an important step in the study of lung nodule detection based on CT images. According to the current problems in recent lung segmentation and lung nodule detection literature, we proposed two new approaches for lung segmentation and nodule detection.

The proposed lung segmentation method is based on flood fill and morphological operations for effectively segmenting the lung regions of varying size, shape and location from HRCT images. Using the statistical characteristics of the intensity distribution, it is possible to easily distinguish the lung and the airway. The lung segmentation process assists the lung nodule detection process with minimising the nodule searching area. In addition, the proposed system has the advantage that it does not require any human expert intervention, nor any prior information about the input image.

The performance of the lung segmentation method was tested through a set of experiments. The measured segmentation accuracies of the lung segmentation method are compared with that of two other fully automatic algorithms that are presented by Sluimer [22] and Vinhais [23]. The comparison result shows the proposed method has lower sensitivity when bronchi regions are large and with a small gap on the side of the lung boundary. Thin lung regions located on the side of lung regions may get eliminated as background information. However, the lung

segmentation method gave excellent results for the rest of lung images. The proposed lung segmentation method is capable of detecting a more precise lung edge than the lung edge generated by edge detection methods.

The proposed lung nodule detection method is based on combining the α-images that contain nodule information to extract the nodule candidates. The extracted nodule candidates are filtered by the rule based filtering process to remove false positives. The shapes of filtered nodule candidates are determined by firstly enlarging the original nodule candidate, then, the radii ratio metric and area ratio metric are used for shape feature determination. Nodules are identified by comparing filtered nodule candidate shape feature with nodule shape feature.

The performance of the lung nodule detection method is well on its way as we have completed the proposed automated lung segmentation method. The method was tested on 100 HRCT lung images that include 75 nodules. The experiment results indicate the detection rate of 88.44%, with a false positive rates of approximately 0.18/slice. The detection rate and false positive rate are measured in terms of the size, shape and location of the nodules. Our finding shows that the nodule detection method is not sensitive to nodule size, but to nodule shape and location. Some challenging nodules such as irregular shaped nodules or nodules attached to veins with similar intensity cannot be identified, and have a low rate of detection. Most of the normal tissues such as blood veins and sternum type can be eliminated from nodule candidates. The performance comparison of the proposed method with that of CNN, GATM, rule based detection and GA methods shows the proposed method has acceptable detection rates and very low false positives. The technique parameters used for the lung nodule detection method are evaluated for improving nodule detection performance.

Experimental results obtained using a large collection of HRCT images with and without nodules show that the proposed approaches are highly effective. To prove the efficiency of the proposed approaches, the experimental results evaluation and comparative analysis were performed. The results of our study show that the

method can be effectively used to segment lung regions and detect the nodules with spherical, star and quadrilateral shape. This research provides a good basis for the development of an efficient and practical lung segmentation and lung nodule detection system.

The results and finding of this research can be used in applications like the Computer-Aided Diagnosis (CAD) system aimed at automating the analysis and processing of lung HRCT images and for supporting diagnosis. The CAD systems consist generally of two stages, the first of which is usually lung segmentation, while the second is the characterisation of disease patterns.

8.2 Future Work

There are many possibilities for further research arising from the work presented in this thesis.

For future improvement of the lung segmentation method we plan to optimise the system by improving the flood fill algorithm for identifying the thorax region, minimising the number of comparisons used in CT background segmentation, and eliminating the repeated operations of the morphological operations. The proposed method could be enhanced by making a stack of HRCT images with 3D morphological operators [62].

For future improvement of the lung nodule detection method we plan to optimise the system by further reducing the number of nodule candidates and improving the shape determination methodology. The number of nodule candidates can be reduced by using image subtraction to eliminate the same information appearing on two continuous images, leaving over the most suspect nodule candidates. The shape determination methodology can be modified in order to determine more nodule shapes.

A few more suggestions for possible future work are as follows:

- Segmented lung regions are used to build 3D volume data and enable accurate visualisation of imaged anatomy and much better visualisation of the disease patterns than conventional CT images.
- More datasets still needed to further improve the lung segmentation technique and the lung nodule detection technique.
- We will be looking at changing the rules applied in an attempt to further reduce false positives while trying not to eliminate nodules.

The number of the simultaneously detected false nodules can be considerably reduced by improving the accuracy of the nodule detection method. But it is still difficult to accurately detect the lung nodules that attach to veins.

Appendix A

Basic Processing Algorithms Used in Lung Segmentation

A.1 Flood fill algorithm

Flood fill algorithm is a recursive graphics algorithm used to fill in irregular-shaped regions with a solid colour. The purpose of flood fill algorithm is to colour an entire area of connected pixels in the same or similar colour [63]. There are two versions of flood fill algorithms: a version with recursive, and a version with a stack. The recursive version is divided into 4-way recursive and 8-way recursive. Stack version is divided into 4-way with stack and 8-way with stack.

A 4-way flood fill method starts from a given pixel, such as the centre pixel as position (x, y) in Figure A.1. The flood fill starts from the centre pixel and moves north, south, east and west.

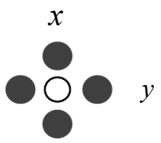

Figure A.1 Template for 4-way Connectivity

A 8-way flood fill method starts from a given pixel, such as the centre pixel as position (x, y) in Figure A.2. The flood fill starts from the centre pixel and moves north, south, east, west, north east (NE), north west (NW), south east (SE) and (south west) SW.

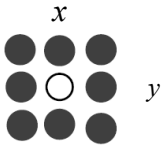

Figure A.2 Template for 8-way Connectivity

In this research, a 4-way recursive version flood fill method is implemented. The following pseudo code presents a stack-based flood fill implementation:

```
Flood-Fill (node, target-colour, replacement-colour):
1. If the colour of node is not equal to target-colour, return.
2. Set the colour of node to replacement-colour.
3. Perform Flood-fill (one step to the west of nodule, target-
   colour, replacement-colour).
   Perform Flood-fill (one step to the east of nodule, target-
   colour, replacement-colour).
   Perform Flood-fill (one step to the north of nodule, target-
   colour, replacement-colour).
   Perform Flood-fill (one step to the south of nodule, target-
   colour, replacement-colour).
4. Return.
```

Where *node* is the centre pixel, *target-colour* is the colour needed to be replaced and *replacement-colour* is the colour to replace it with. Figure A.3 shows the process of the flood fill algorithm. In Figure A.3(a), the *node* is located inside of the *y* shape region, *target-colour* is the white colour displayed in each cell, and the *replacement-colour* is black. The cells in the *y* shape region are processed by the flood fill algorithm and highlighted in black, as shown in Figure A.3(b).

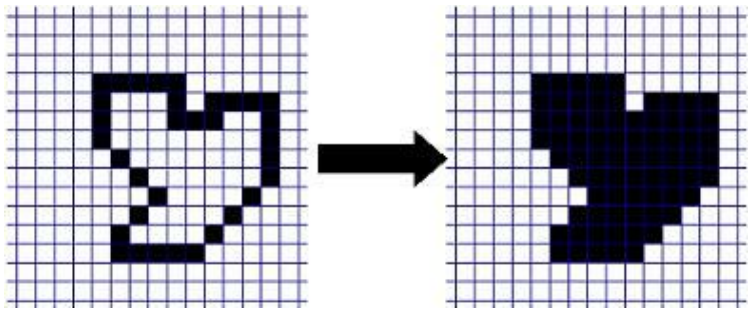

(a) (b)

Figure A.3 Flood fill algorithm (a) Before flood fill algorithm (b) After flood fill algorithm

A.2 Morphological Operators

Mathematical morphology is a set-theoretical approach to multi-dimensional digital signal or image analysis, based on shape [64]. Morphological operations are

used to understand the structure of form of an image. This usually means identifying objects or boundaries in an image. Morphological operations are used in applications such as machine vision and automatic object detection. Figure A. 4 shows an example of a binary image, which is used for morphological operation processing.

Figure A.4 Example of a binary image [65]

While morphological operations are usually performed on binary images, some processing techniques also apply to greyscale images. These operations are for the most part limited to erosion and dilation. Figure A.5 shows the result images that generated by the morphological operations.

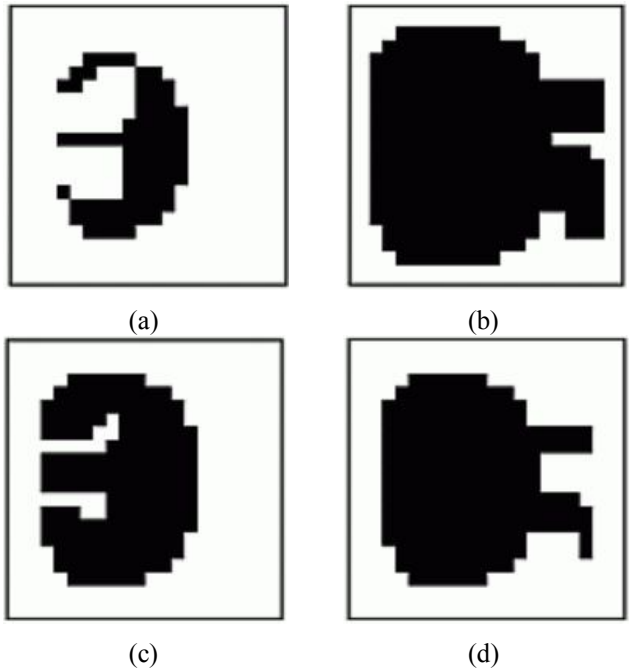

Figure A.5 Four basic morphological operations (a) Erosion (b) Dilation (c) Opening (d) Closing [65]

In Figure A.5(a)-(b), the binary image shown in Figure A.4 is processed by the two most common morphological operations, erosion and dilation. In erosion, every object pixel that is touching a background pixel is changed into a background pixel. In dilation, every background pixel that is touching an object pixel is changed into an object pixel. Erosion makes the objects smaller, and it can break a single object into multiple objects. Dilation makes the objects larger, and it can merge multiple objects into one. Those operations are the foundation for the opening and closing operations.

Opening and closing help separate and join objects. These two operations are the simple combination of erosion and dilation. Opening spaces objects that are too close together, detaches objects that are touching and should not be, and enlarges holes inside objects. In Figure A.5(c)-(d), opening is defined as an erosion followed by a dilation, and closing is defined as a dilation followed by an erosion.

Appendix B

Developed Application for Visualisation

A simple application with Graphical User Interface (GUI) is proposed in this research. This application is used to view the α-images that belong to different α-intervals, segmented lung regions, combined α-images and nodule detection results.

Figure B.1 shows the α-image generation for an original lung image. The α-images belonging to different α-intervals can be viewed in the application (see Figure B.1(a)). The application also highlights α-image pixels in red on original lung images, as shown in Figure B.1(b). Highlighting the pixels on the original lung image is used to determine nodule pixel α-ranges.

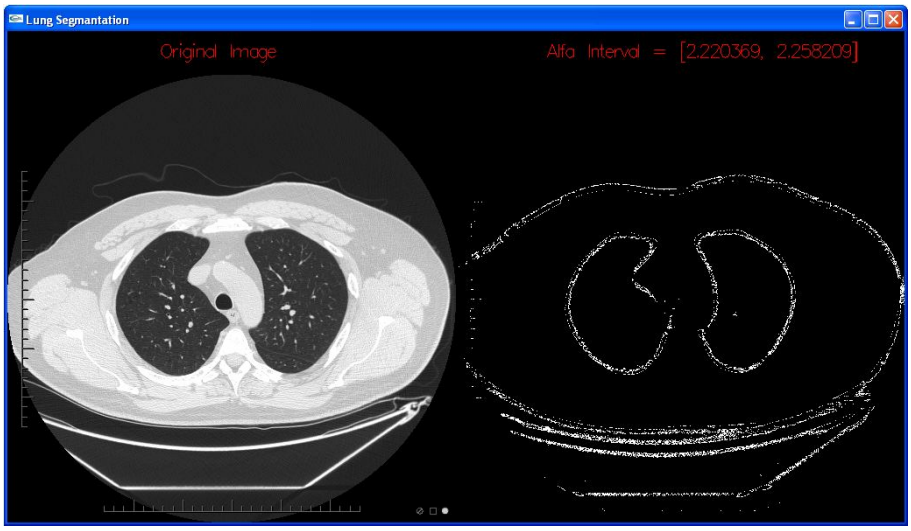

(a)

Figure B.1 α-image generation for original lung images (a) α-image shown on the right side of the application (b) α-image pixels are highlighted in red on the original lung images

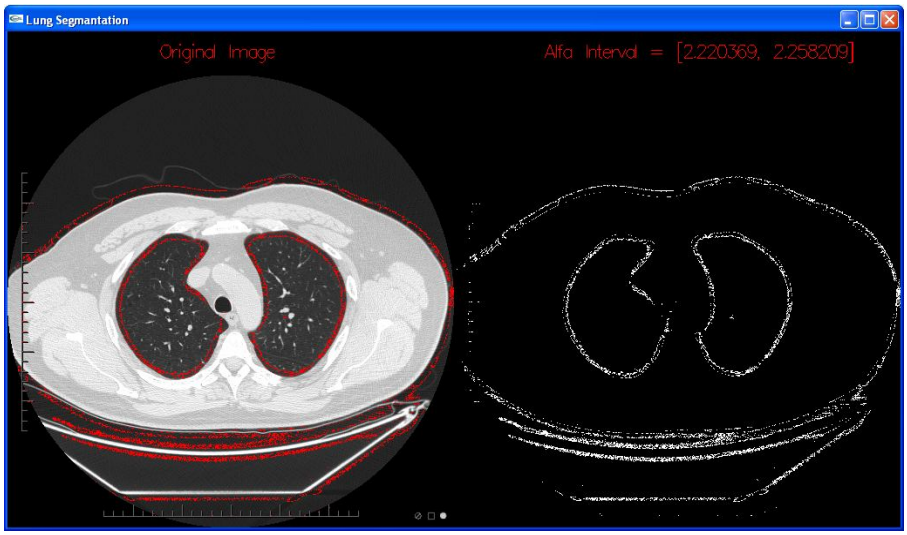

(b)

Figure B.1 (contd.)

The application displays the lung regions that are extracted from the original lung image. Segmented lung regions also require α-image generation, as shown in Figure B.2.

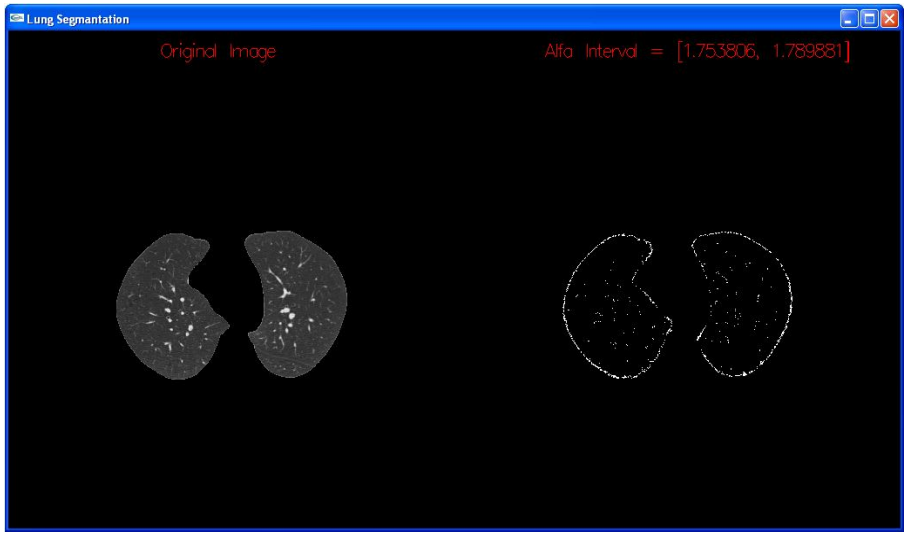

(a)

Figure B.2 α-image generation for segmented lung images (a) α-image shown on the right side of the application (b) α-image pixels are shown on the original lung image in red colour

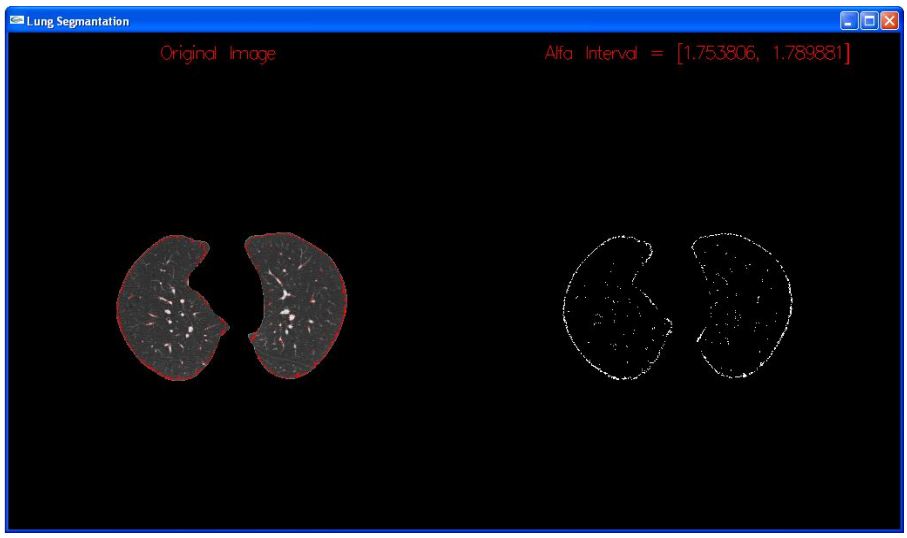

(b)

Figure B.2 (contd.)

The generated α-images need to be combined for complete nodule information extraction, as shown in Figure B.3.

Figure B.3 α-image combination based on segmented lung regions.

The combined α-image requires further rule based filtering processing to reduce false positives and obtain more precise nodule detection result. The filtered nodule candidates are shown in Figure B.4.

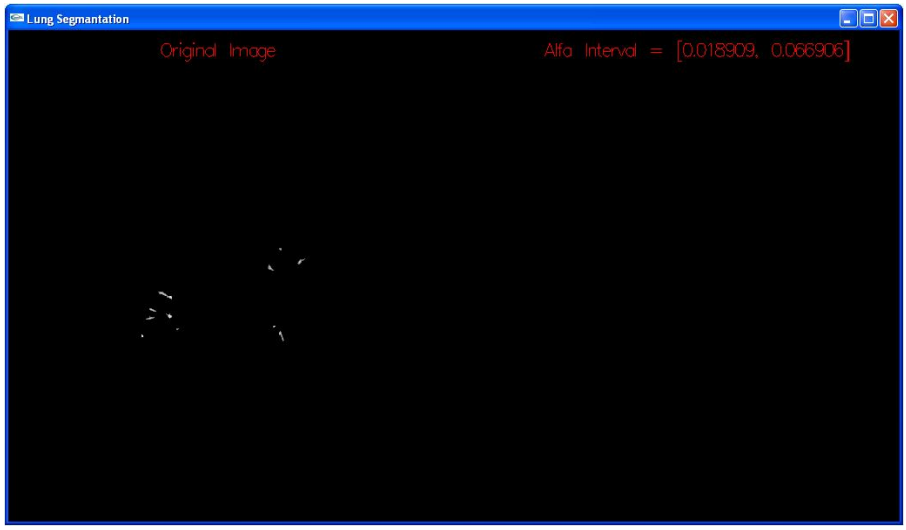

Figure B.4 Rule based filtering processed nodule candidates

Nodules are highlighted in green, which clearly indicates their position. The detected nodules can be clearly seen from the application.

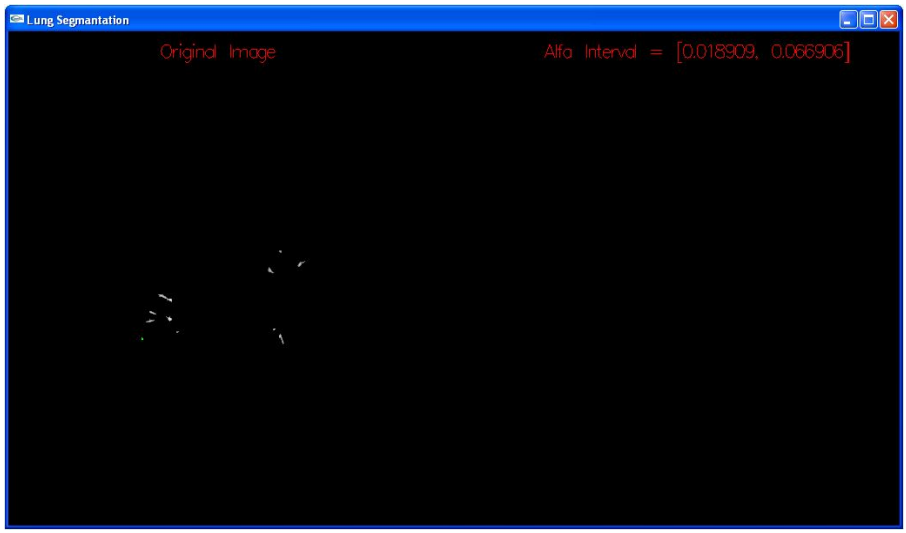

Figure B.5 Lung nodule detection result

Overall, the application visualises the whole process of lung image analysis and processing. All the experiment results are generated from this application, so their correctness can be visually identified.

References

[1] E. Neri, Caramella, Davide, Bartolozzi, and Carlo, *Image Processing in Radiology*. Germany: Springer Berlin Heidelberg New York, 2008.

[2] D. I. Fotiadis, A. N. Papadopoulos, and M. E. Plissiti, *Medical Image Analysis Methods*. Boca Raton London New York Singapore: Taylor & Francis Group, LLC, 2005.

[3] N. A. Memon, A. M. Mirza, and S. A. M. Gilani, "Segmentation of Lungs from CT Scan Images for Eatly Diagnosis of Lung Cancer," *Proceedings of World Academy of Science, Engineering and Technology,* vol. 14, 2006.

[4] H. M. Inc. (2008, 07/10). *Lung cancer cure*. Available: http://www.infobarrel.com/Lung_cancer_cure

[5] A. Misra, M. Rudrapatna, and A. Sowmya, "Automatic lung segmentation: a comparison of anatomical and machine learning approaches," in *Intelligent Sensors, Sensor Networks and Information Processing Conference, 2004. Proceedings of the 2004*, 2004, pp. 451-456.

[6] Z. Tatjana and S. Busayarat, "Computer-aided Analysis and Interpretation of HRCT Images of the Lung " in *Theory and Applications of CT Imaging and Analysis*, N. Homma, Ed., ed: Intech, 2011, p. 26.

[7] A. Farag, A. El-Baz, G. Gimel'farb, and R. Falk, "Detection and recognition of lung nodules in spiral CT images using deformable templates and Bayesian post-classification," in *Image Processing, 2004. ICIP '04. 2004 International Conference on*, 2004, pp. 2921-2924 Vol. 5.

[8] S. L. A. Lee, A. Z. Kouzani, and E. J. Hu, "Random forest based lung nodule classification aided by clustering," *Computerized medical imaging and graphics* vol. 34, pp. 535-542, 2010-10 2010.

[9] Y. Ming, S. Periaswamy, and W. Ying, "False positive Reduction in Lung GGO Nodule Detection with 3D Volume Shape Descriptor," in *Acoustics, Speech and Signal Processing, 2007. ICASSP 2007. IEEE International Conference on*, 2007, pp. I-437-I-440.

[10] H. A. B. Fukumoto, T. Nitta, and N. Tsudagawa, "Detection of Ground Glass Opacities in Lung CT Images Using Gabor Filters and Neural Networks," presented at the Instrumentation and Measurement Technology Conference, Ottawa, Ont, 2005.

[11] A. A. Farag, A. El-Baz, G. Gimel'farb, and R. Falk, "Detection and recognition of lung abnormalities using deformable templates," in *Pattern Recognition, 2004. ICPR 2004. Proceedings of the 17th International Conference on*, 2004, pp. 738-741 Vol.3.

[12] I. Amirav, S. S. Kramer, M. M. Grunstein, and E. A. Hoffman, "Assessment of methacholine-induced airway constriction by ultrafast high-resolution computed tomography," *J. Appl. Physiol,* vol. 75, 1993.

[13] R. H. Brown, C. J. Herold, C. A. Hirshman, E. A. Zerhouni, and W. Mitzner, "In Vivo Measurements of Airway Reactivity Using High-Resolution Computed Tomography," *American Review of Respiratory Disease,* vol. 144, 1991.

[14] E. A. Hoffman, S. J. Lai-Fook, J. Wei, and E. H. Wood, "Estimation of regional pleural surface expansile forces in intact dogs," *J Appl Physiol,* vol. 55, 1983.

[15] M. S. Brown, M. F. McNitt-Gray, J. G. Goldin, R. D. Suh, J. W. Sayre, and D. R. Aberle, "Patient-specific models for lung nodule detection and surveillance in CT images," *Medical Imaging, IEEE Transactions on,* vol. 20, pp. 1242-1250, 2001.

[16] Y. Xujiong, L. Xinyu, J. Dehmeshki, G. Slabaugh, and G. Beddoe, "Shape-Based Computer-Aided Detection of Lung Nodules in Thoracic CT Images," *Biomedical Engineering, IEEE Transactions on,* vol. 56, pp. 1810-1820, 2009.

[17] D. M. Denison, M. D. Morgan, and A. B. Millar, "Estimation of regional gas and tissue volumes of the lung in supine man using computed tomography," vol. 41, pp. 620-628, 1986.

[18] G. J. Kemerink, R. J. S. Lamers, B. J. Pellis, H. H. Kruize, and J. M. A. v. Engelshoven, "On segmentation of lung parenchyma in quantitative computed tomography of the lung," *Med. Phys,* vol. 25, pp. 2432-2439, 1998.

[19] L. W. Hedlund, R. F. Anderson, P. L. Goulding, J. W. Beck, E. L. Effmann, and C. E. Putman, "Two methods for isolating the lung area of a CT scan for density information," *Radiology,* vol. 144, pp. 353-357, 1982.

[20] W. A. Kalender, H. Fichte, W. Bautz, and M. Skalej, "Semiautomatic evaluation procedures for quantitative CT of the lung," *J. Comput. Assist. Tomogr,* vol. 15, pp. 248–255, 1991.

[21] R. Shojaii, J. Alirezaie, and P. Babyn, "Automatic lung segmentation in CT images using watershed transform," in *Image Processing, 2005. ICIP 2005. IEEE International Conference on*, 2005, pp. II-1270-3.

[22] I. C. Sluimer, M. Neineijer, and B. V. Ginnerken, "Lings field Segmentation from Thin-Slice CT Scans in Presence of Severe Pathology " *Medical Imaging, Proceding of SPIE,* vol. 5370, Ballingham, WA, 2004.

[23] C. Vinhais, A. e. Campilho, and M. Kamel, "Lung Parenchyma Segmentation from CT Images Based on Material Decomposition," *ICIAR,* vol. 4142, 2006.

[24] L. Tseng and H. Li-Chin, "An adaptive thresholding method for automatic lung segmentation in CT images," in *AFRICON, 2009. AFRICON '09.*, 2009, pp. 1-5.

[25] S. Hu, E. A. Hoffman, and J. M. Reinhardt, "Automatic lung segmentation for accurate quantitation of volumetric X-ray CT images," *Medical Imaging, IEEE Transactions on,* vol. 20, pp. 490-498, 2001.

[26] K. Doi, H. P. Chan, and C. J. Vyborny, "Improvement in Radiologists Detection of Clustered Microcalcification Mammograms: The Potential of Computer-Aided Diagnosis," *Inves. Radio,* vol. 25, pp. 1102-1110, 1990.

[27] M. L. Giger, N. Ahn, K. Doi, H. MacMahon, and C. E. Metz, "Computerized Detection of Pulmonary Nodules in Digital Chest Images: Use of Morphological Filters in Reducting False-Positive Detections," *Med. Phys,* vol. 17, pp. 861-865, 1990.

[28] K. Suzuki, L. Feng, S. Sone, and K. Doi, "Computer-aided diagnostic scheme for distinction between benign and malignant nodules in thoracic low-dose CT by use of massive training artificial neural network," *Medical Imaging, IEEE Transactions on,* vol. 24, pp. 1138-1150, 2005.

[29] K. Suzuki, "A supervised 'lesion-enhancement' filter by use of a massive-training artificial neural network (MTANN) in computer-aided diagnosis (CAD)," *Phys. Med. Biol,* vol. 54, pp. S31-S45, 2009.

[30] L. Boroczky, Z. Luyin, and K. P. Lee, "Feature Subset Selection for Improving the Performance of False positive Reduction in Lung Nodule CAD," *Information Technology in Biomedicine, IEEE Transactions on,* vol. 10, pp. 504-511, 2006.

[31] B. v. Ginneken, "Supervised probabilistic segmentation of pulmonary nodules in CT scans," in *In: 9th Medical Image Computing and Computer-assisted Intervention –MICCAI Conference*, Berlin, 2006.

[32] S. Matsumoto, K. HL, G. JC, G. WB, and H. H, "Pulmonary nodule detection in CT images with quantized convergence index filter," *Med Image Anal,* vol. 10, pp. 343-352, 2006.

[33] IC Sluimer, v. W. PF, V. MA, and v. G. B, "Computer-aided diagnosis in high resolution CT of the lungs," *Med Phys,* vol. 30, pp. 3081-3090, 2003.

[34] M. A. J. Klik, E. M. v Rikxoort, J. F. Peters, H. A. Gietema, M. Prokop, and B. v Ginneken, "Improved classification of pulmonary nodules by automated detection of benign subpleural lymph nodes," in *Biomedical Imaging: Nano to Macro, 2006. 3rd IEEE International Symposium on*, 2006, pp. 494-497.

[35] J. Lin, P. A. Ligomenides, S. C. B. Lo, M. T. Freedman, and S. K. Mun, "A hybrid neural-digital computer-aided diagnosis system for lung nodule detection on digitized chest radiographs," in *Computer-Based Medical Systems, 1994., Proceedings 1994 IEEE Seventh Symposium on*, 1994, pp. 207-212.

[36] D. Y. Kim, J. H. Kim, and S. M. Noh, "Pulmonary nodule detection using chest CT images.," *Acta. Radiol,* vol. 44, 2003.

[37] Y. Lee, T. Hara, H. Fujita, S. Itoh, and T. Ishigaki, "Automated detection of pulmonary nodules in helical CT images based on an improved template-matching technique," *Medical Imaging, IEEE Transactions on,* vol. 20, pp. 595-604, 2001.

[38] J. Dehmeshki, X. Ye, X. Y. Lin, M. Valdivieso, and H. Amin, "Automated detection of lung nodules in CT images using shape-based genetic algorithm," *Comput Med Imaging Graph,* vol. 31, pp. 408-417, 2007.

[39] K. Shigemoto, remove capitals: T. HOTAKA, Y. SHINJI, N. TOORU, M. TOORU, T. YUKIO, I. TAKESHI, and M. MITSUOMI, "Efficient Recognition Method for Lung Nodule Shadows in X-ray CT Images Using 3-D Object Models and Template Matching Techniques," *Med Imaging Technol,* vol. 21, pp. 147-156, 2003.

[40] Y. Zheng, C. Kambhamettu, T. Bauer, and K. Steiner, "Accurate estimation of pulmonary nodule's growth rate in CT images with nonrigid registration and precise nodule detection and segmentation," in *Computer Vision and Pattern Recognition Workshops, 2009. CVPR Workshops 2009. IEEE Computer Society Conference on*, 2009, pp. 101-108.

[41] M. Antonelli, G. Frosini, B. Lazzerini, and F. Marcelloni, "A CAD System for Lung Nodule Detection based on an Anatomical Model and a Fuzzy Neural Network," in *Fuzzy Information Processing Society, 2006. NAFIPS 2006. Annual meeting of the North American*, 2006, pp. 448-453.

[42] K. Kanazawa, Y. Kawata, N. Niki, H. Satoh, H. Ohmatsu, and R. Kakinuma, "Computer-aided diagnosis for pulmonary nodules based on helical CT images," in *Pattern Recognition, 1998. Proceedings. Fourteenth International Conference on*, 1998, pp. 1683-1685 vol.2.

[43] Y. Kawata, N. Niki, H. Ohmatsu, M. Kusumoto, R. Kakinuma, K. Mori, H. Nishiyama, K. Eguchi, M. Kaneko, and N. Moriyama, "Hybrid Classification Approach of Malignant and Benign Pulmonary Nodules Based on Topological and Histogram Features " *Medical Image Computing and Computer-Assisted Intervention,* vol. 1935, pp. 297-306, 2000.

[44] K.Falconer, *Fractal Geometry: Mathematical Foundations and Applications*. England: Wiley, 2003.

[45] L. Yuxin and L. Yanda, "New approaches of multifractal image analysis," in *Information, Communications and Signal Processing, 1997. ICICS., Proceedings of 1997 International Conference on*, 1997, pp. 970-974 vol.2.

[46] T. Stojic, I. Reljin, and B. Reljin, "Adaptation of multifractal analysis to segmentation of microcalcifications in digital mammograms," *Physica A: Statistical Mechanics and its Applications,* vol. 367, pp. 494-508, 2006.

[47] K. Falconer, *Fractal Geometry: Mathematical Foundations and Applications*, 2nd Edition ed. England: Wiley, 2003.

[48] Nilsson and Ethel, "Multifractal-based Image Analysis with Applications in Mwdical Imaging," Umea University, 2007.

[49] Needs surname R. I. S and R. B. D, "Fractal geometry and multifractals in analyzing and processing medical data and images," *Archive of oncology,* vol. 10, pp. 283-293, 2002.

[50] I. Reljin, B. Reljin, I. Pavlovic, and I. Rakocevic, "Multifractal analysis of gray-scale images," in *Electrotechnical Conference, 2000. MELECON 2000. 10th Mediterranean*, 2000, pp. 490-493 vol.2.

[51] J. L. Véhel and P. Mignot, "Multifractal Segmentation of Images," *Fractals,* vol. 2, pp. 371-378, 1994.
[52] E. Nilsson, "Multifractal-based Image Analysis with applications in Medical Imaging," Master's Degree, Computer Science and Mathematics, Umea University, Sweden, 2007.
[53] Q. Dawei and Y. Lei, "Multifractal spectrum theory used to medical image from CT testing," in *Advanced Intelligent Mechatronics, 2008. AIM 2008. IEEE/ASME International Conference on*, 2008, pp. 68-73.
[54] S. V. Burtsev and Y. P. Kuzmin, "An efficient flood-filling algorithm," *Computer & Graphics,* vol. 17, pp. 549-561, 1993.
[55] P. Andre, "Intelligent Flood Fill or: The use of Edge Detection in Image Object Extraction," University of Southampton2005.
[56] M. Rudrapatna, A. Sowmya, and P. Wilson, "Automatic detection of hilum and parenchymal bands on HRCT lung images," in *Cybernetics and Intelligent Systems, 2004 IEEE Conference on*, 2004, pp. 769-774.
[57] G. Qixin, W. ShengJun, Z. Dazhe, and L. Jiren, "Accurate Lung Segmentation For X-ray CT Images," in *Natural Computation, 2007. ICNC 2007. Third International Conference on*, 2007, pp. 275-279.
[58] J. Tschirren, "Segmentation, anatomical labeling, ranchpoint matching, and quantitative analysis of human airway trees in volumetric CT images," PhD thesis, The University of Iowa, 2003.
[59] D. Phillips. (2000). *Image Processing in C (2nd ed.)*.
[60] G. Bradski and A. Kaebler, *Learning OpenCV*. Sebastopol: O'Reilly Media, Inc, 2008.
[61] G. X. Ritter and J. N. Wilson, *Handbook of Computer Vision Algorithms in Image Algebra*: CRC Press LLC, 1996.
[62] J. Lerdsinmongkol, K. Chaisaowong, S. Roongruangsorakarn, T. Kraus, and T. Aach, "Application of 3D Morphological Operations in the Framework of a Computer-Assisted Diagnonsis System to Construct Thorax Mask and Remove Trachea," presented at the The 3rd International Symposium on Biomedical Engineering, 2009.
[63] L. Vandevenne. (2004, 16/01). *Lode's Computer Graphics Tutorial: Flood Fill*. Available: http://lodev.org/cgtutor/floodfill.html
[64] R. K. Bock. (1998). *Morphological Operations*. Available: http://rd11.web.cern.ch/RD11/rkb/AN16pp/node178.html
[65] S. W. Smith, *The Scientist & Engineer's Guide to Digital Signal Processing*: California Technical Pub, 1997.